



TECHNICAL REPORT 5-75-9

DEVELOPMENT OF A PROJECTILE PENETRATION THEORY

Report 1

PENETRATION THEORY FOR SHALLOW TO MODERATE DEPTHS

by

Robert S. Bernard, Sathya V. Hanagud

Soils and Pavements Laboratory

U. S. Army Engineer Waterways Experiment Station

P. O. Box 631, Vicksburg, Miss. 39180

June 1975

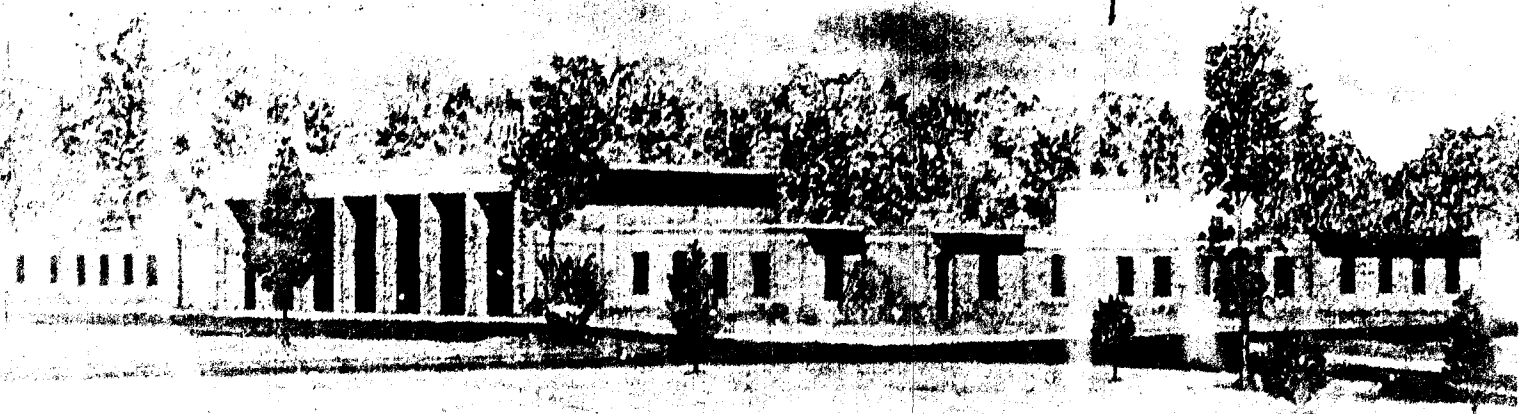
Report 1 of a Series

Approved For Public Release; Distribution Unlimited

12

OFFICE
OF THE
CHIEF OF ENGINEERS
U. S. ARMY
WASHINGTON, D. C.
1250

APA 013361



Prepared for Office, Chief of Engineers, U. S. Army
Washington, D. C. 20314

Under Project 4A161102B52E, Task 04,
Work Unit 013

Unclassified

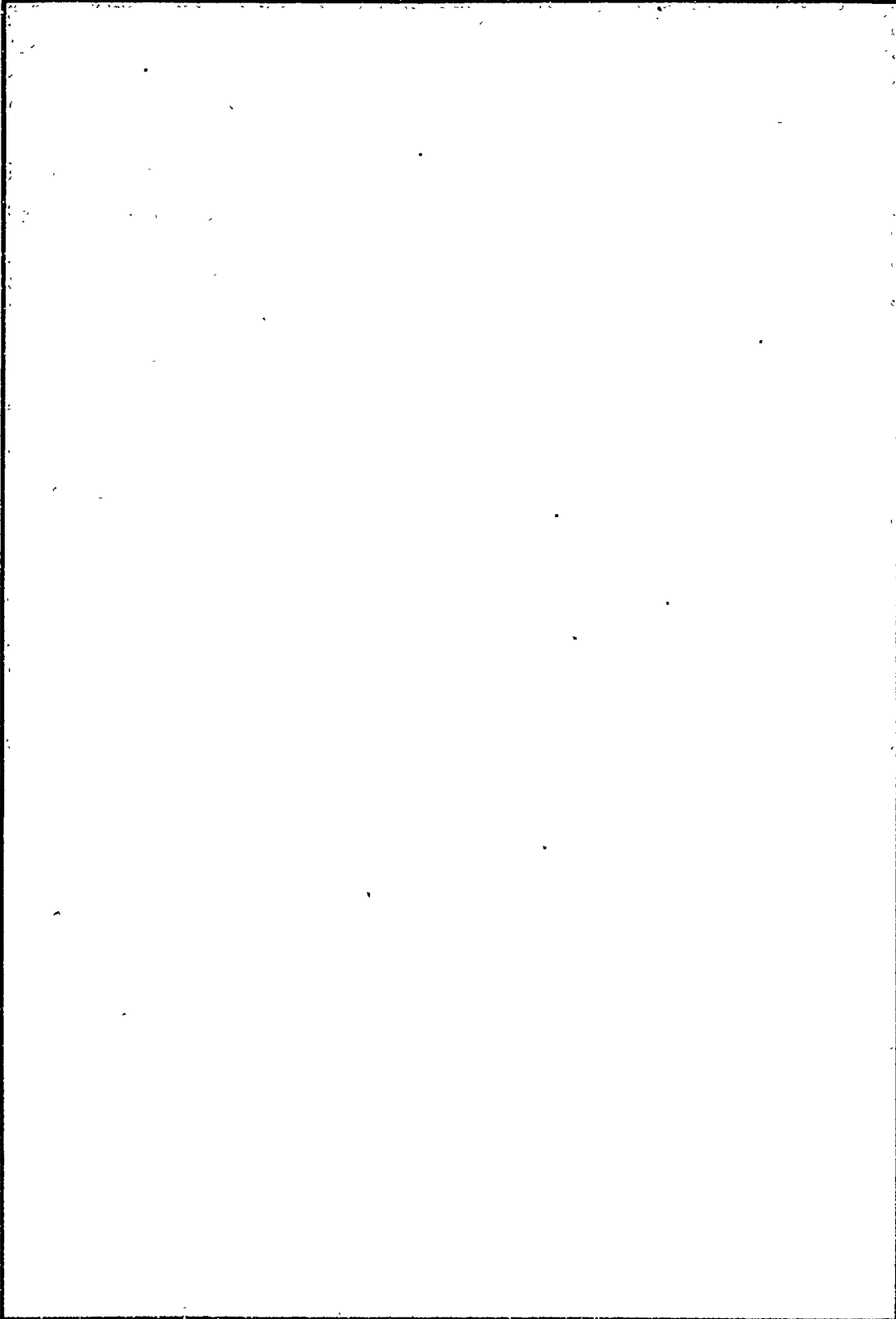
SECURITY CLASSIFICATION OF THIS PAGE (When Data Entered)

REPORT DOCUMENTATION PAGE		READ INSTRUCTIONS BEFORE COMPLETING FORM
1. REPORT NUMBER ⑨ Technical Report Jul 75 - Jun 75	2. GOVT ACCESSION NO.	3. RECIPIENT'S CATALOG NUMBER
⑥ DEVELOPMENT OF A PROJECTILE PENETRATION THEORY; Report 1. PENETRATION THEORY FOR SHALLOW TO MODERATE DEPTHS	5. TYPE OF REPORT & PERIOD COVERED Report 1 of a Series.	
	6. PERFORMING ORG. REPORT NUMBER	
7. AUTHOR(s) ⑩ Robert S. Bernard Sathya V. Hanagud	8. CONTRACT OR GRANT NUMBER(s) ⑫ 99 p.	
9. PERFORMING ORGANIZATION NAME AND ADDRESS U. S. Army Engineer Waterways Experiment Station Soils and Pavements Laboratory P. O. Box 631, Vicksburg, Miss. 39180	10. PROGRAM ELEMENT, PROJECT, TASK AREA & WORK UNIT NUMBERS Project 4A161102B52E, Task 04, Work Unit 013	
11. CONTROLLING OFFICE NAME AND ADDRESS Office, Chief of Engineers, U. S. Army Washington, D. C. 20314	⑪ Jun 75	12. REPORT DATE
13. MONITORING AGENCY NAME & ADDRESS (if different from Controlling Office) ⑭ AEWES-TR-S-75-9-1	13. NUMBER OF PAGES 96	
16. DISTRIBUTION STATEMENT (of this Report) Approved for public release; distribution unlimited. ⑮ DA-4-A-161102-B-52-E	15. SECURITY CLASS. (of this report) Unclassified	
15a. DECLASSIFICATION/DOWNGRADING SCHEDULE		
17. DISTRIBUTION STATEMENT (of the abstract entered in Block 20, if different from Report)		
18. SUPPLEMENTARY NOTES		
19. KEY WORDS (Continue on reverse side if necessary and identify by block number) Projectile penetration		
20. ABSTRACT (Continue on reverse side if necessary and identify by block number) Previous work in penetration theory, based on the theory for dynamic expansion of a spherical cavity in a compressible strain-hardening medium, is extended to include the effects of nose shape, layered targets, and oblique impact. Parametric implications of the theory are investigated, and governing parameters are defined. Theoretical results are compared with experimental and empirical results and with two-dimensional finite-difference solutions; good agreement is obtained when the penetration resistance of the target due to shear is comparable with that due to inertia.		

DN

Unclassified

SECURITY CLASSIFICATION OF THIS PAGE(When Data Entered)



Unclassified

SECURITY CLASSIFICATION OF THIS PAGE(When Data Entered)

PREFACE

The investigation reported herein was conducted by personnel of the Soils and Pavements Laboratory (S&PL), U. S. Army Engineer Waterways Experiment Station (WES), as a part of DA Project No. 4A161102B52E, "Fragment and Projectile Penetration Resistance of Soils," Task 04, Work Unit 013.

The research was accomplished by Mr. R. S. Bernard (WES) and Professor S. V. Hanagud, Georgia Institute of Technology, during the period July 1973 to June 1974 under the supervision of Dr. J. G. Jackson, Jr., Chief of the Soil Dynamics Division, S&PL. Messrs. J. P. Sale and R. G. Ahlvin were Chief and Assistant Chief, S&PL, respectively. SP4 D. C. Creighton executed the necessary computer calculations, and Dr. B. Rohani provided continuing support through his familiarity with previous work in this area. This report was prepared by Mr. Bernard and Professor Hanagud.

BG E. D. Peixotto, CE, and COL G. H. Hilt, CE, were Directors of WES during this investigation and the preparation of the report. Mr. F. R. Brown was Technical Director.

CONTENTS

	<u>Page</u>
PREFACE	1
CONVERSION FACTORS, U. S. CUSTOMARY TO METRIC (SI) UNITS OF MEASUREMENT	4
PART I: INTRODUCTION	5
Background	5
Purpose	6
Scope	6
PART II: PENETRATION THEORY	8
Historical Background	8
Cavity Expansion Theory	8
Penetration Theory for Spherical Projectiles	9
Penetration Theory for Axisymmetric Projectiles	12
Penetration Theory for Layered Targets	21
Oblique Impact Theory	28
PART III: SOME PARAMETRIC IMPLICATIONS OF PENETRATION THEORY	37
The Nondimensional Equation of Motion	37
The Shape of the Deceleration Curve	40
The Relative Effects of Nose Shape and Frontal Loading on Final Depth of Penetration	42
Parametric Differences Between Theoretical and Empirical Results for Homogeneous Targets	45
Penetration of Layered Targets	46
PART IV: APPLICATIONS OF PENETRATION THEORY	47
Introduction	47
Choice of Material Properties	47
Penetration of Rock	48
Penetration of Concrete	51
Penetration of Soft Earth	53
Perforation of a Metal Slab	54
Oblique Impact Against Hard Earth	60
PART V: CONCLUSIONS AND RECOMMENDATIONS	63
REFERENCES	65
APPENDIX A: SPHERICAL CAVITY EXPANSION IN A CONCENTRICALLY LAYERED MEDIUM	A1
Introduction	A1
Problem Formulation	A1
Inertial Terms	A4
Shear Terms	A8
Relations Among $a(t)$, $b(t)$, and $h(t)$	A12
Combined Effects	A14

CONTENTS

	<u>Page</u>
Summary of Results	A16
Special Cases	A18
APPENDIX B: COMPRESSIBILITY	B1
Introduction	B1
Average Dynamic Pressure in the Plastic Zone	B1
Compressibility in the Penetration Theory	B3
APPENDIX C: TARGET ACCELERATION	C1
Introduction	C1
The Effect of Added Mass on Penetration Predictions	C1
APPENDIX D: NOTATION	D1

CONVERSION FACTORS, U. S. CUSTOMARY TO METRIC (SI)
UNITS OF MEASUREMENT

U. S. customary units of measurement used in this report can be converted to metric (SI) units as follows:

Multiply	By	To Obtain
inches	2.54	centimetres
feet	0.3048	metres
pounds (mass)	0.4535924	kilograms
slug-square feet	1.353	kilogram-square metres
pounds (mass) per cubic foot	16.01846	kilograms per cubic metre
slugs per cubic foot	515.3788	kilograms per cubic metre
pounds (force) per square inch	6894.757	pascals
kips (force) per square inch	6894.757	kilopascals
feet per second	0.3048	metres per second
degrees (angle)	0.0174539	radians

Note: 1 kbar = 1,000 bars = 14,500 pounds per square inch
= 100 megapascals.
1 slug = 32.2 pounds (mass).

DEVELOPMENT OF A PROJECTILE PENETRATION THEORY

PENETRATION THEORY FOR SHALLOW TO MODERATE DEPTHS

PART I: INTRODUCTION

Background

1. The phenomenon of projectile penetration has been the object of numerous analytical and experimental investigations over the past two centuries.¹ Until recent years, successful analyses were of an empirical or semiempirical nature, utilizing various target resistance functions and pseudoconstants which were inevitably drawn directly from penetration experiments. As a result, the subject of penetration remained isolated from the rest of mechanics because the relation between target constitutive properties and penetration resistance was unknown. Nevertheless, a number of useful empirical equations were developed which afforded reasonable estimates of penetration depth for a variety of situations.¹⁻⁴ Unfortunately, the reliability of such equations is limited to the range of test conditions for which they were deduced, and the accuracy of prediction may dwindle significantly with extrapolation to situations which have not been characterized experimentally.

2. The last decade has given rise to a more basic approach to penetration through the use of digital computers. In various efforts, the details of target and projectile motion have been analyzed by means of two-dimensional finite-difference techniques employing realistic constitutive properties for both target and projectile.⁵⁻⁷ While a finite-difference solution may achieve good agreement with experimental observation, as shown in Reference 7, its execution is cumbersome and costly, thus diminishing its utility as a practical engineering tool. However, this approach represents a powerful device for examining the details of target and projectile behavior, indicating the relative consequences of different simplifying assumptions, and providing a means of determining what mechanisms are most important in the projectile-target interaction.

3. At the present time, there is a growing need for a simple theory which affords reliable analyses of the impact and penetration of rigid projectiles such as missiles, bombs, bullets, shell fragments, artillery and mortar rounds, and air-delivered mines and sensors into targets such as soil, rock, concrete, and metal. The results of these analyses could be used in design and optimization, both from the offensive and defensive points of view. In July 1973, a small research effort was initiated under the sponsorship of the Office, Chief of Engineers, to develop a tractable projectile penetration theory for natural and artificial earth targets. The general requirements were that the theory should account for the penetration of homogeneous and layered targets by rigid projectiles of various nose shapes and should deal at least approximately with oblique impact. Further, the theory should be derived from a consideration of target constitutive properties without recourse to penetration tests per se. The objective was to replace neither empirical nor finite-difference analyses, but rather to provide a practical tool for making reasonable predictions before the execution of a penetration test or finite-difference calculation. The developments presented in this report are the result of efforts conducted under this program during the period July 1973 to June 1974. Report 2 will document the extension of the present theory for application to very deep penetration in homogeneous and layered targets.

Purpose

4. The purpose of this investigation is to build upon existing penetration theory⁸⁻¹² to develop an approximate but more general theory meeting the requirements stated above. The starting point for the present work is the so-called "cavity expansion theory," originally applied to projectile penetration by Goodier.^{9,10}

Scope

5. Part II of this report outlines modifications of previous theoretical work⁸⁻¹² in which the effects of different nose shapes,

layered targets, and oblique impact are incorporated into a penetration theory for rigid projectiles. In Part III, the modified theory is non-dimensionalized, governing parameters are determined, and results of parameter studies are presented. Part IV contains comparisons of theoretical results with experimental observations and two-dimensional finite-difference solutions. Part V presents the conclusions and recommendations. The theory of dynamic expansion of a spherical cavity in a concentrically layered medium is developed in Appendix A. A discussion of material compressibility as it relates to the cavity expansion theory and the penetration theory is contained in Appendix B. The effect of target acceleration on final penetration depth predictions is investigated in Appendix C.

PART II: PENETRATION THEORY

Historical Background

6. The foundation for the present penetration theory was laid by Bishop, Hill, and Mott,⁸ who applied the theory of spherical cavity expansion in a strain-hardening medium to penetration by a rigid static punch. Goodier¹⁰ later extended this work and applied it to the penetration of a strain-hardening target by a high-velocity rigid spherical projectile. Hanagud and Ross¹² modified the cavity expansion theory to account for a compressible medium by means of a locking approximation and employed the results in Goodier's penetration theory.

Cavity Expansion Theory

7. The theory of dynamic expansion of a spherical cavity surrounded by concentric layers of compressible locking, strain-hardening material is developed in Appendix A. This cavity expansion theory forms the basis for the penetration theory discussed in the present report. The behavior of the material in shear (Figure A2) is characterized by the compressive yield strength Y , the modulus of elasticity E , and the strain-hardening modulus E_t .* The effect of material compressibility is approximated by means of an instantaneous locking assumption whereby material in the plastic state is presumed to be compressed to a uniform (i.e. locked) density ρ_ℓ . As discussed in Appendix B, the instantaneous locked density ρ_ℓ is a function of the instantaneous average dynamic pressure in the plastic zone.

8. According to Equation A76, the compressive normal stress p at the cavity surface is

$$p = p_s + \rho_\ell (B_1 a \ddot{a} + B_2 \dot{a}^2) \equiv p_s + p_I \quad (1)$$

* For convenience, symbols and unusual abbreviations are listed and defined in the Notation (Appendix D).

The two terms, p_s and p_I , which appear in Equation 1 are the separate contributions due to material deformation (shear) and inertia, respectively. Henceforth, the shear contribution p_s will be called the "shear resistance"; and the inertial contribution $p_I = \rho_\ell (B_1 a \ddot{a} + B_2 \dot{a}^2)$ will be called the "dynamic pressure" where a , \dot{a} , and \ddot{a} are the radial position, velocity, and acceleration of the cavity wall, and B_1 and B_2 are dimensionless inertial coefficients. For a homogeneous material (i.e. no layering), p_s , B_1 , and B_2 are identified by Equations A87, A88, and A89, respectively. Moreover, these quantities are functions of Y , E , E_t , and the instantaneous locking strain $\epsilon_\ell \equiv \ln \rho / \rho_\ell$, where ρ is the initial density.

Penetration Theory for Spherical Projectiles

9. While spherical cavity expansion and projectile penetration can hardly be regarded as the same process, the penetration of a solid target by a rigid spherical projectile (Figure 1) suggests at least a crude analogy with spherical cavity expansion. Goodier is the first investigator to apply such an analogy to projectile penetration. Considering only rigid spherical projectiles, he makes the following assumptions:

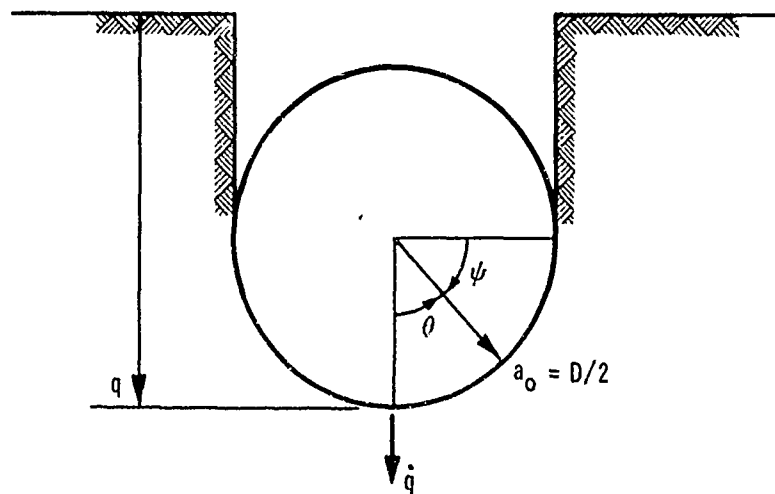


Figure 1. Fully embedded spherical projectile

- a. The embedded portion of the projectile frontal surface as seen in the above figure is in complete contact with the target.
- b. During the embedding process (penetration depth $q \leq$ projectile radius a_0), the projectile-target interaction is equivalent to a dynamic Brinell hardness test, and the total resisting force is given by Meyer's law.⁹⁻¹²
- c. After the projectile is fully embedded ($q > a_0$), only normal stresses exist on the projectile frontal surface (i.e., the effect of friction is negligible).

10. At this point, Goodier sets about to modify Equation 1 in order to approximate the normal stress distribution on the frontal surface of a fully embedded spherical projectile. To this end he makes two assumptions: (a) the normal stress due to shear (i.e. shear resistance) is constant over the frontal surface and is identical with p_s in Equation 1; and (b) p_I is maximum at the stagnation point $\theta = 0$ and zero at the shoulder $\theta = \pi/2$, where θ is measured as shown in Figure 1. Identifying a_0 with the cavity radius a , the projectile velocity \dot{q} with the cavity radial velocity \dot{a} , and the projectile acceleration \ddot{q} with the cavity radial acceleration \ddot{a} , Goodier then proposes

$$p_I = \rho_\ell (B_1 a_0 \ddot{q} + B_2 \dot{q}^2) \cos \theta \quad (2)$$

as a reasonable variation of dynamic pressure over the frontal surface $0 \leq \theta \leq \pi/2$. The compressive normal stress p on the projectile frontal surface is then

$$p = p_s + \rho_\ell (B_1 a_0 \ddot{q} + B_2 \dot{q}^2) \cos \theta \quad (3)$$

In Goodier's investigation the target is assumed incompressible such that^{9,10} $\rho_\ell = \rho$, $B_1 = 1$, and $B_2 = 3/2$. The rationale employed by Hanagud and Ross^{11,12} is identical with that of Goodier except that the target is considered compressible locking such that $\rho_\ell > \rho$, $B_1 < 1$, $B_2 < 3/2$, and the value of p_s is less than the incompressible value.

11. Integration of Equation 3 over the frontal surface leads to the following equation of motion for a projectile of mass M :

$$M\ddot{q} = -\pi a_o^2 \left[p_s + \frac{2}{3} \rho_l (B_1 a_o \ddot{q} + B_2 \dot{q}^2) \right] \quad (4)$$

Equation 4 is rearranged such that

$$\left(M + \frac{2}{3} \pi a_o^3 \rho_l B_1 \right) \ddot{q} = -\pi a_o^2 \left(p_s + \frac{2}{3} \rho_l B_2 \dot{q}^2 \right) \quad (5)$$

Equation A88 indicates that $B_1 \leq 1$; consequently, the effect of target acceleration is small in Equations 4 and 5 when the added mass¹³ for the sphere is small compared to the projectile mass, i.e., when

$$\frac{2}{3} \pi a_o^3 \rho_l \ll M \quad (6)$$

With the ratio R_a defined as

$$R_a \equiv \frac{\pi a_o^3 \rho_l}{M} \quad (7)$$

the effect of target acceleration on projectile loading is then small when $R_a \ll 1$. Moreover, the quantity $(2/3)\pi a_o^3 \rho_l B_1$ probably represents a high upper limit on the added mass term, and penetration predictions are improved in some cases by discarding the added mass term (i.e. the B_1 term) altogether, as shown in Appendix C. At any rate, Goodier's dynamic pressure distribution is adequately approximated by

$$p_I \approx \rho_l B_2 \dot{q}^2 \cos \theta , \quad R_a \ll 1 \quad (8)$$

12. Although the rationale employed by Goodier leads to fairly accurate predictions of final penetration depth (Appendix C), the $\cos \theta$ distribution of p_I is somewhat arbitrary. Other distributions of dynamic pressure produce projectile equations of motion identical to Equations 4 and 5. (For example, this occurs when $\cos \theta$ is replaced by $1 - \sin^4 \theta$ in Equations 2 and 3.) Furthermore, the

projectile equation of motion must be integrated with respect to time to obtain the final depth of penetration, so that a "correct" prediction of final depth alone indicates only that the average resisting force is correctly predicted. Thus, there is some flexibility in Goodier's rationale, insofar as the distribution of dynamic pressure is concerned. Moreover, it is this flexibility which allows extension of the cavity expansion analogy to projectiles with nose shapes other than hemispherical.

Penetration Theory for Axisymmetric Projectiles

13. Before generalizing the penetration theory to nose shapes other than hemispherical, it is necessary to reevaluate Goodier's three basic assumptions. First, the assumption of complete contact between the target and the embedded portion of the projectile nose (i.e. frontal surface) is retained. Although this assumption is physically questionable, it will provide an upper limit on the resisting force, at least within the framework of the theory. Second, the dynamic Brinell hardness analogy is discarded. Instead, an analogy with the cavity expansion theory will be used throughout the penetration process to approximate the normal stress distribution on the embedded portion of the projectile nose. (This will produce a higher target resistance during the embedding process, which will improve penetration depth predictions, especially for shallow penetration.) Third, friction effects are disregarded at all times on the projectile nose and aft body alike. This is a questionable assumption, although there is some evidence suggesting that friction on the aft body is relatively insignificant.^{7,14}

14. Subject to the above assumptions, Equation 1 is now modified in order to approximate the normal stress distribution on the nose of a projectile with an arbitrary axisymmetric nose shape. As in Goodier's rationale, the normal stress due to shear is assumed uniform over the nose and equal to p_s . This leaves only the distribution p_I to be determined as a function of nose shape. The problem, of course, is to arrive at a single rationale which generalizes the distribution of p_I

to any axisymmetric nose shape in a straightforward manner. Furthermore, the resulting effect of nose shape on final penetration depth should be consistent with experimental observation.

15. One approach is simply to guess the form of the p_I distribution in a manner similar to Goodier.^{9,10} Consider a projectile with a fully embedded conical nose, as shown in Figure 2. As in the case of a

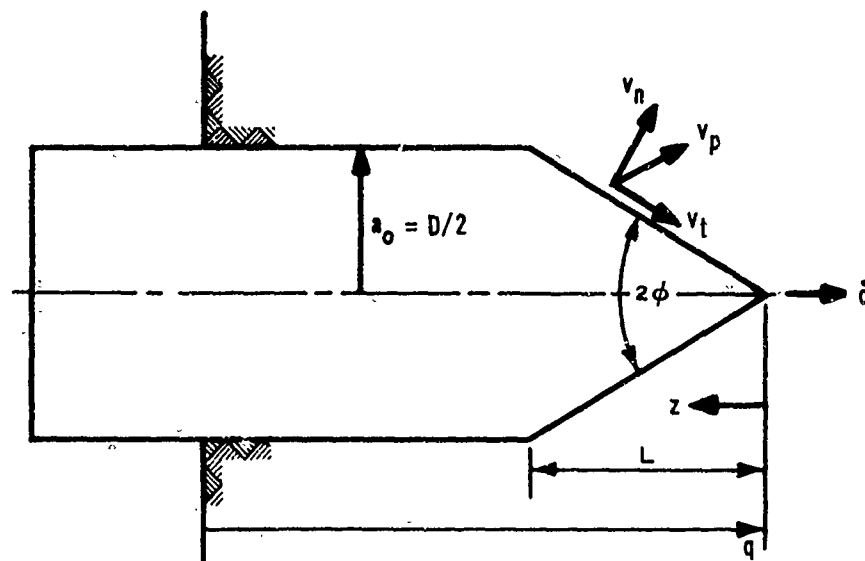


Figure 2. Projectile with a conical nose

hemispherical nose, one might assume that $p_I = \rho_\ell (B_1 a_0 \ddot{q} + B_2 \dot{q}^2)$ at the stagnation point (i.e., at the tip of the nose, $z = 0$). At the base of the nose, $z = L$, one might assume that the dynamic pressure reduces to $p_I = \rho_\ell (B_1 a_0 \ddot{q} + B_2 \dot{q}^2) \sin^n \phi$. This value corresponds to the value of p_I on a hemispherical nose at polar angle $\theta = \pi/2 - \phi$ when p_I is distributed according to $\cos^n \theta$ (as opposed to $\cos \theta$). The variation of p_I from $z = 0$ to $z = L$ could then be expressed according to

$$p_I = \rho_\ell (B_1 a_0 \ddot{q} + B_2 \dot{q}^2) \left[\sin^n \phi + (1 - \sin^n \phi) f(z) \right] \quad (9)$$

where $f(z)$ is a dimensionless function which decreases smoothly from unity at $z = 0$ to zero at $z = L$.

16. Since the problem at hand is to make an ad hoc modification of the dynamic pressure for different nose shapes, there is basically

nothing wrong with the approach outlined above. On the other hand, the arbitrariness in the development of Equation 9 prompts one to seek a more fundamental scheme based (albeit crudely) on the underlying physics. The fact that the dynamic pressure which appears in Equation 1 depends on both particle acceleration and velocity suggests that the p_I distribution for an axisymmetric projectile can be obtained by approximating the variation of particle acceleration and velocity along the surface of the nose. Moreover, since most cases of practical interest satisfy the condition $R_a \ll 1$, the particle acceleration has only a small effect on projectile loading, and it is then sufficient to approximate the variation of particle velocity alone.

17. In order to construct a reasonable distribution of particle velocity v_p on the nose surface, one must first consider certain physical constraints on particle motion:

- a. A particle at the very tip of the nose (i.e. the stagnation point) must move with the projectile velocity \dot{q} .
- b. The component of particle velocity v_n normal to the surface of the nose must be equal to the normal component of projectile velocity (i.e., material cannot cross the target/projectile interface).
- c. Over the nose surface v_p must be continuous.
- d. Finally, it is assumed that the tangential component of particle velocity v_t is zero at the base of the nose.

Relative to these constraints, only the variation of v_t along the length of the nose remains to be specified. Although it is quite possible that v_t is a complicated function of target properties, projectile velocity, nose shape, and relative position on the nose, the present investigation considers only the effects of nose shape and relative position.

18. Consider first the fully embedded conical nose shown in Figure 2. The normal component of velocity v_n is given by

$$v_n = \dot{q} \sin \phi \quad (10)$$

where ϕ is the cone half-angle. Now defining

$$x \equiv \frac{z}{L} \quad (11)$$

where z is longitudinal distance from the nose tip and L is nose length, the following equation is proposed for v_t :

$$v_t = (1 - x)^{1/2} \dot{q} \cos \phi, \quad 0 \leq x \leq 1 \quad (12)$$

The resulting expression for v_p is then

$$v_p = \left(v_n^2 + v_t^2 \right)^{1/2} = \dot{q} \left(1 - x \cos^2 \phi \right)^{1/2} \quad (13)$$

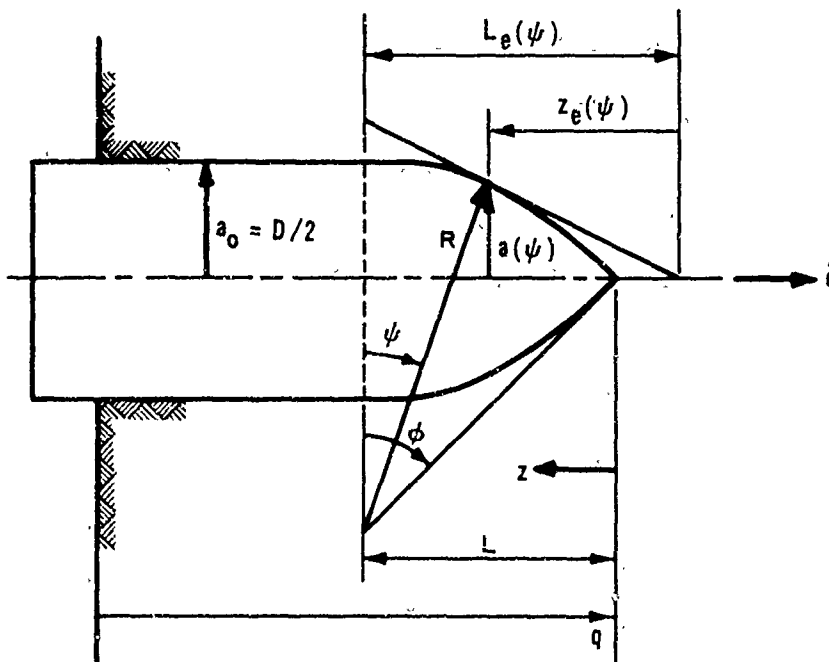


Figure 3. Projectile with an ogival nose

19. Consider next the fully embedded ogival nose shown in Figure 3. The normal component v_n is given by

$$v_n = \dot{q} \sin \psi \quad (14)$$

where ψ is the half-angle for the circumscribed cone which is tangent to the ogive at any longitudinal position z . To arrive at a functional form for v_t which is consistent with Equation 12, the effective cone length $L_e(\psi)$ and effective longitudinal position $z_e(\psi)$ (Figure 3) are defined by

$$L_e(\psi) \equiv \frac{R(1 - \cos \theta \cos \psi)}{\sin \psi} \quad (15)$$

and

$$z_e(\psi) \equiv a(\psi) \cot \psi \quad (16)$$

where

$$a(\psi) = R(\cos \psi - \cos \theta) \quad (17)$$

and

$$a_0 = R(1 - \cos \theta) \quad (18)$$

The effective dimensionless cone position $x_e(\psi)$ is then defined as

$$x_e(\psi) \equiv \frac{z_e(\psi)}{L_e(\psi)} = \frac{\cos \psi (\cos \psi - \cos \theta)}{1 - \cos \theta \cos \psi} \quad (19)$$

In order to be consistent with Equation 12, v_t is taken to be

$$v_t = \dot{q} [1 - x_e(\psi)]^{1/2} \cos \psi \quad (20)$$

Thus, the expression for v_p is

$$v_p = \left(v_n^2 + v_t^2 \right)^{1/2} = \dot{q} \left[1 - x_e(\psi) \cos^2 \psi \right]^{1/2} \quad (21)$$

20. By replacing a by a_0 , \dot{s} by v_p , and \ddot{a} by \ddot{q} in Equation 1, the general expression for p_I on an axisymmetric nose surface is

$$P_I = \rho_l B_1 a \ddot{q} + \rho_l B_2 v_p^2 \approx \rho_l B_2 v_p^2, \quad R_a \ll 1 \quad (22)$$

where v_p is given by Equations 13 and 21 for cones and ogives, respectively. Thus,

$$P_I \approx \rho_l B_2 (1 - x \cos^2 \theta) \dot{q}^2 \quad \text{for cones} \quad (23)$$

and

$$P_I \approx \rho_l B_2 [1 - x_e(\psi) \cos^2 \psi] \dot{q}^2 \quad \text{for ogives} \quad (24)$$

when $R_a \ll 1$. For a hemispherical nose, which is the limiting case for an ogive, Equation 24 reduces to

$$P_I \approx \rho_l B_2 \dot{q}^2 (1 - \cos^4 \psi) = \rho_l B_2 \dot{q}^2 (1 - \sin^4 \theta) \quad (25)$$

where $\theta = \pi/2 - \psi$ as indicated in Figure 1. A comparison of Equations 8 and 25 is presented in Figure 4 to show that for a hemispherical

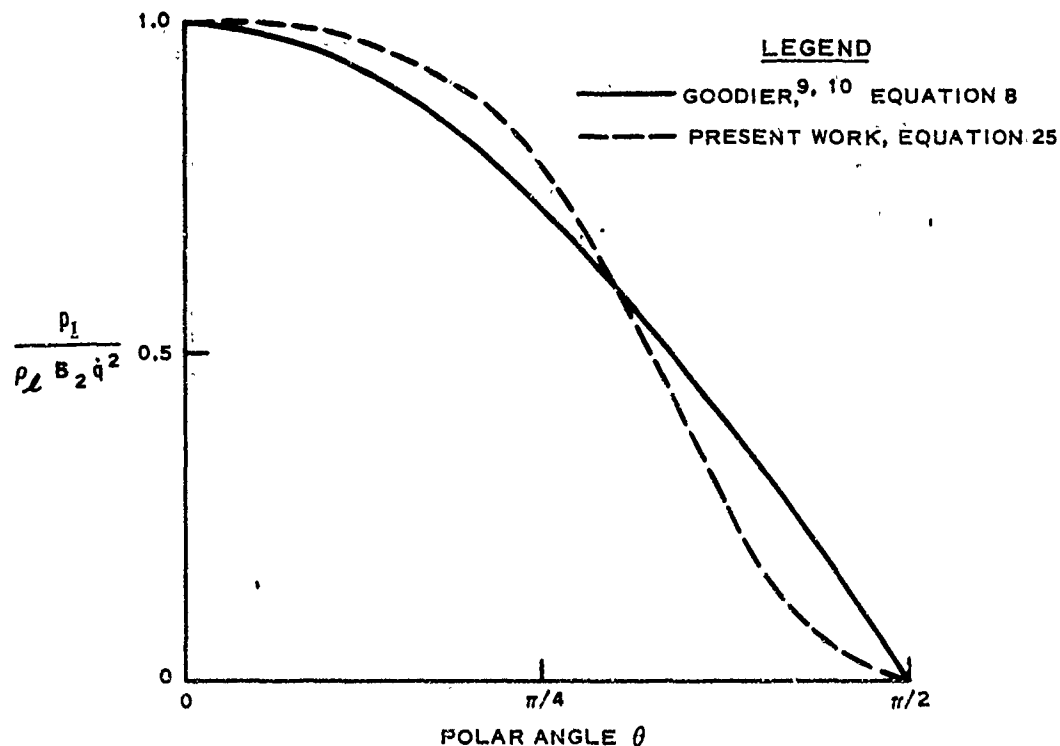


Figure 4. Graphic comparison of Equations 8 and 25 for distribution of dynamic pressure on a hemispherical nose

nose the p_I distribution obtained by assuming a functional form for v_t is not radically different from Goodier's assumed p_I distribution.

21. With the normal stress distribution having been approximated for conical and ogival noses (the rationale outlined in paragraphs 17-20 can be readily applied to other axisymmetric nose shapes), the next step is to obtain the resulting projectile equations of motion. This involves integrating the normal stress over the surface of the nose to obtain the total axial resisting force F_z acting on the projectile. Thus, for projectiles with conical noses, Equations 11, 13, and 22 are substituted into Equation 1 and integrated over the surface of the nose to obtain

$$M\ddot{q} = -F_z = - \int_{z=0}^{z=L} [p_s + p_I(z, \phi)] \sin \phi \, dA(z, \phi) \quad (26)$$

where

$$dA(z, \phi) = 2\pi \frac{\tan \phi}{\cos \phi} z \, dz \quad (27)$$

Likewise, for projectiles with ogival noses, Equations 19, 21, and 22 are substituted into Equation 1 and integrated over the surface of the nose to obtain

$$M\ddot{q} = -F_z = - \int_{\psi=\phi}^{\psi=0} [p_s + p_I(\psi)] \sin \psi \, dA(\psi) \quad (28)$$

where

$$dA(\psi) = 2\pi \frac{\tan \psi}{\cos \psi} z_e(\psi) \, dz_e(\psi) \quad (29)$$

The resulting projectile equations of motion have the form

$$\left(M + \pi a_o^3 \rho_\ell B_1 \right) \ddot{q} = -\pi a_o^2 \left(p_s + \rho_\ell B_2 f_n \dot{q}^2 \right) \quad (30)$$

The quantity f_n (nose shape factor) results from the variation of p_I over the nose and thus characterizes the relative effect of nose shape on the average inertial resistance of the target to penetration. For conical noses of length L and base diameter $D = 2a_0$ shown in Figure 2, f_n is expressed as

$$f_n = 1 - \frac{2}{3} \left(\frac{4\zeta^2}{4\zeta^2 + 1} \right) \quad (31)$$

where

$$\zeta \equiv \frac{L}{D} \quad (32)$$

For ogival noses of length L and base diameter D illustrated in Figure 3, f_n is written as

$$f_n = 1 - \frac{2}{\epsilon^2(1-\epsilon)^6} \left[B^2 \ln(2-\epsilon) - (3B^2 + 2B)(B-\epsilon) + \frac{1}{2} (3B^2 + 6B + 1)(B^2 - \epsilon^2) - \frac{1}{5} (B^5 - \epsilon^5) - \frac{1}{3} (B^2 + 6B + 3)(B^3 - \epsilon^3) + \frac{1}{4} (2B + 3)(B^4 - \epsilon^4) \right] \quad (33)$$

where

$$B \equiv 2\epsilon - \epsilon^2 \quad (34)$$

$$\epsilon \equiv \frac{2}{4\zeta^2 + 1} \quad (35)$$

and $\zeta = L/D$. For ogives, the relation between the caliber radius head (CRH) and ζ is

$$CRH = \zeta^2 + \frac{1}{4} \quad (36)$$

An ogive with $\zeta = 1/2$ is a hemisphere, for which case Equation 33 reduces to $f_n = 2/3$ and the right hand side of Equation 30 is identical

with Equation 5. Thus, for spherical projectiles and projectiles with hemispherical nose shapes, the distribution of particle velocity given by Equation 21 leads to essentially the same equation of motion as that obtained by Goodier^{9,10} and by Hanagud and Ross^{11,12} when $R_a \ll 1$.

22. Whether one chooses to develop projectile equations of motion based on assumed stress distributions or assumed particle velocity distributions is of little consequence in the final analysis. The important question is whether or not the equation of motion (30) leads to reliable predictions of final penetration depth for projectiles with different nose shapes. Moreover, the relative effect of nose shape on final penetration depth should lie within experimentally observed bounds. (For earth penetration, variation of nose shape from a blunt cylinder to a sharp cone seldom increases final penetration depth by more than a factor of three.²) Thus, the choice of a velocity or stress distribution leading to f_n is neither arbitrary nor unique, and it is no accident that variation of nose shape from a blunt cylinder to a sharp cone reduces target inertial resistance in Equation 30 by no more than a factor of three. The tangential velocity distribution given by Equation 12 is chosen so as to produce precisely this effect.

23. While f_n is presumed to characterize the relative effect of nose shape on inertial resistance to penetration for a fully embedded nose, the embedding process itself must also be considered in order to determine the overall effect of nose shape on penetration depth, especially for shallow penetration. Assuming that f_n approximately characterizes inertial resistance during the embedding of the nose, the equation of motion during the embedding process is

$$\left[M + \pi a_n^3(q) \rho_\ell B_1 \right] \ddot{q} = -\pi a_n^2(q) \left[p_s + \rho_\ell B_2 f_n \dot{q}^2 \right], \quad q \leq L \quad (37)$$

where $a_n(q)$ is the cylindrical radius of the nose at the surface of the target, and $\pi a_n^2(q)$ is the frontal area of the projectile which is in contact with the target for a given penetration depth $q \leq L$, as shown in Figure 5. When $q \geq L$, Equation 37 is replaced by Equation 30.

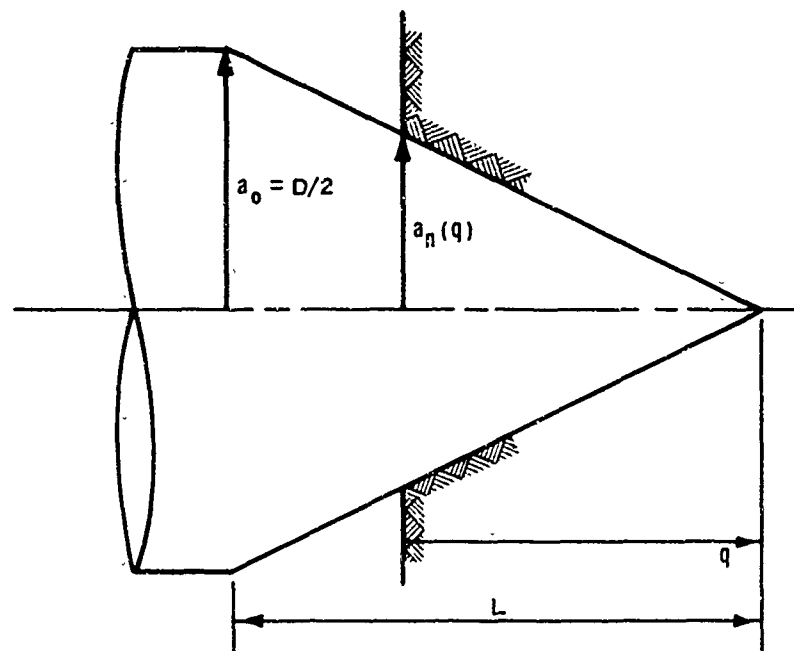


Figure 5. Projectile with partially embedded nose

A study of the relative effect of nose shape on final penetration depth is given in Part III.

Penetration Theory for Layered Targets

24. The penetration theory for layered targets is based upon the cavity expansion theory for a concentrically layered medium presented in Appendix A. The physical situation to be considered is illustrated in Figure 6. As is the case in Appendix A, the investigation is restricted to the two-layer situation. Physically, this means that a target may have any number of layers so long as the projectile equation of motion is significantly influenced by no more than two layers at a time.

25. The projectile equation of motion is assumed to have the same form as that for a homogeneous target, Equation 30. However, approximations for p_s , B_1 , and B_2 must be obtained through an appropriate analogy with the cavity expansion theory for a concentrically layered medium. The point which becomes the point of maximum deformation on the layer interface is denoted by $H(t)$ and coincides with the projectile axis of symmetry (Figure 6). The initial distance from the

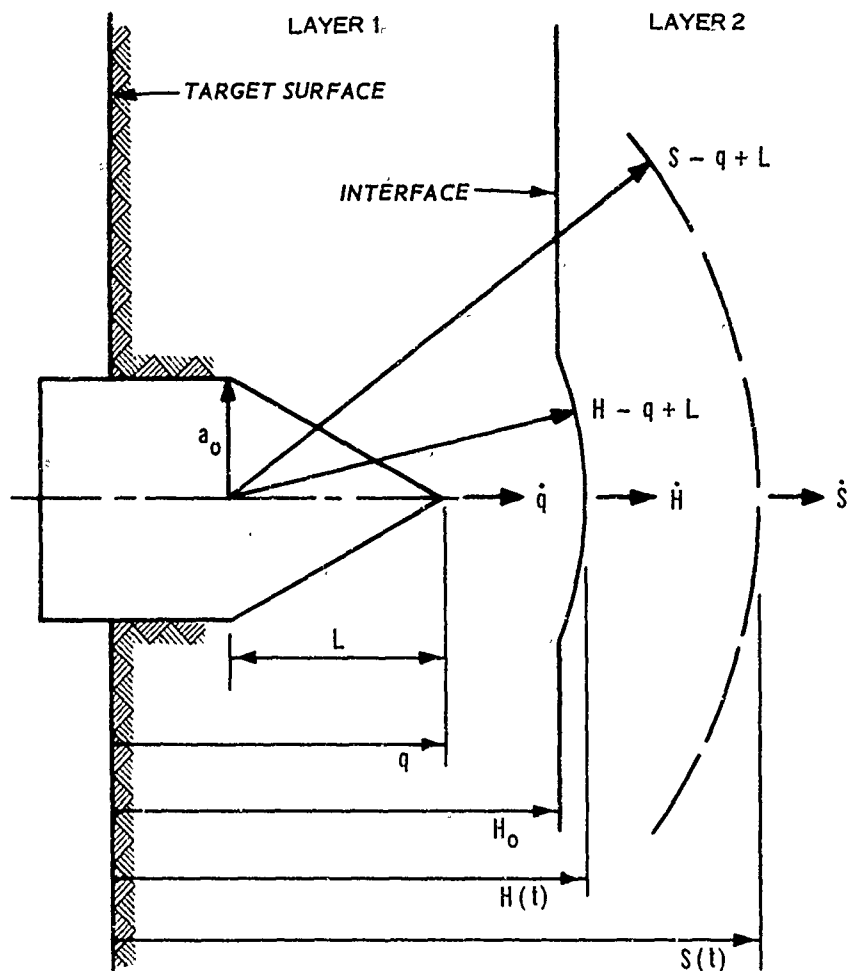


Figure 6. Penetration of a layered target

target surface to the layer interface is H_0 . A first approximation (probably representing an upper limit) to the effective deformation of the layer interface is then obtained by replacing the penetrating projectile with a spherical cavity of radius a_0 and radial velocity \dot{q} located at the base of the projectile nose (i.e., at depth $q - L$) and assuming that the motion of the point $H(t)$ is the same as that of a point lying on a spherical surface of instantaneous effective radius $H - q + L$ and effective radial velocity \dot{H} , concentric to the effective cavity ($a = a_0$). The motion of the plastic front $S(t)$ can be determined in the same way, where $S - q + L$ is the instantaneous effective radius of the front and \dot{S} is its effective radial velocity. First approximations to p_s , B_1 , and B_2 are then

obtained by substituting a_0 for $a(t)$, \dot{q} for \dot{a} , $H_0 - q + L$ for h_0 , $H - q + L$ for $h(t)$, \dot{H} for \dot{h} , $S - q + L$ for $b(t)$, and \dot{S} for \dot{b} in Equations A79-A84.

26. In direct analogy with Appendix A, $H \cong H_0$ for $S \leq H_0$, i.e., the deformation of the interface is assumed negligible prior to the arrival of the plastic front. From Equation A57, $S - q + L$ is related to a_0 by

$$S - q + L = \frac{a_0}{\delta_1^{1/3}}, \quad S < H_0 \quad (38)$$

where δ_1 is given by Equation A53. The condition $S \leq H_0$ is now replaced by $q \leq q_*$ where

$$q_* \equiv H_0 + L - \frac{a_0}{\delta_1^{1/3}} \quad (39)$$

which represents projectile penetration depth when the plastic front reaches the layer interface. Equation 39 is structured so that $S = H_0$ when $q = q_*$. When $q \leq q_*$, the projectile equation of motion is

$$\left[M + \pi a_0^3 \rho_{\ell_1} B_1^{(1)} \right] \ddot{q} = -\pi a_0^2 \left[p_s^{(1)} + \rho_{\ell_1} B_2^{(1)} f_n q^2 \right], \quad q < q_* \quad (40)$$

where, with the exception of $B_1^{(1)}$ and $B_2^{(1)}$, the subscripts 1 and 2 denote first and second layer properties, and

$$p_s^{(1)} = -\frac{2}{3} Y_1 \ln \delta_1 + \frac{4}{9} E_{t_1} \left[\frac{\pi^2}{6} - \sum_{m=1}^{\infty} \frac{\delta_1^m}{m^2} \right] + \frac{4}{3} \beta_1 E_1 \left[1 - \frac{a_0^3}{\delta_1 (H_0 - q + L)^3} \right] + \frac{\frac{4}{3} \beta_1 E_2 a_0^3}{\delta_1 (H_0 - q + L)^3} \quad (41)$$

$$B_1^{(1)} = 1 - \delta_1^{1/3} + \left(1 - \frac{\alpha_1}{\delta_1}\right) \left[\delta_1^{1/3} - \frac{a_o \left(1 - \frac{\rho_2}{\rho_1}\right)}{H_o - q + L} \right] \quad (42)$$

and

$$B_2^{(1)} = 2B_1^{(1)} + \frac{\alpha_1(1 - \delta_1)^2}{(1 - \alpha_1)\delta_1^{2/3}} - \frac{1}{2} \left(1 - \delta_1^{4/3}\right) - \frac{\left(1 - \frac{\alpha_1}{\delta_1}\right)^2}{2(1 - \alpha_1)} \left[\delta_1^{4/3} - \frac{a_o^4 \left(1 - \frac{\rho_2}{\rho_1}\right)}{(H_o - q + L)^4} \right] \quad (43)$$

where δ , β , and α are defined by Equations A90, A91, and A93, respectively. Equations 41-43 are analogous to Equations A79-A81.

27. After the plastic front has reached the interface, the projectile equation of motion is

$$\left[M + \pi a_o^3 \rho_{\ell_1} B_1^{(*)} \right] \ddot{q} = -\pi a_o^2 \left[p_s^{(*)} + \rho_{\ell_1} B_2^{(*)} f_n \dot{q}^2 \right], \quad q > q_* \quad (44)$$

where, with the exceptions of $B_1^{(*)}$ and $B_2^{(*)}$, the subscripts 1 and 2 denote first and second layer material properties, and

$$p_s^{(*)} = 2Y_1 \ln \left(\frac{H - q + L}{a_o} \right) + \frac{4}{9} E_{t_1} \left[\frac{\pi^2}{6} - \sum_{m=1}^{\infty} \frac{1}{m^2} \left(\frac{a_o}{H - q + L} \right)^{3m} \right] + 2Y_2 \ln \left(\frac{S - q + L}{H - q + L} \right) + \frac{4}{9} E_{t_2} \sum_{m=1}^{\infty} \frac{\delta_2^m}{m^2} \left[\left(\frac{S - q + L}{H - q + L} \right)^{3m} - 1 \right] + \frac{4}{3} \beta_2 E_2 \quad (45)$$

$$B_1^{(*)} = 1 - \frac{a_0}{H - q + L} + \frac{\rho_{\ell_1}}{\rho_{\ell_2}} \left[\frac{a_0}{H - q + L} - \frac{\alpha_2 a_0}{\delta_2 (S - q + L)} \right] \quad (46)$$

$$B_2^{(*)} = 2B_1^{(*)} + \frac{\rho_{\ell_2} \alpha_2 (1 - \delta_2)^2}{\rho_{\ell_1} \delta_2^2 (1 - \alpha_2)} \left(\frac{a_0}{S - q + L} \right)^4 - \frac{1}{2} \left\{ 1 - \left(\frac{a_0}{H - q + L} \right)^4 + \frac{\rho_{\ell_2}}{\rho_{\ell_1}} \left[\left(\frac{a_0}{H - q + L} \right)^4 - \left(\frac{a_0}{S - q + L} \right)^4 \right] \right\} - \frac{\rho_{\ell_2}}{2\rho_{\ell_1}} \frac{\left(1 - \frac{\alpha_2}{\delta_2} \right)^2}{(1 - \alpha_2)} \left(\frac{a_0}{S - q + L} \right)^4 \quad (47)$$

Equations 45-47 are analogous to Equations A82-A84. Examining Equation A64, and substituting $H - q + L$ for h , \dot{H} for \dot{h} , $S - q + L$ for b , and \dot{S} for \dot{b} , then

$$(H - q + L)^2 \dot{H} = \delta_2 (S - q + L)^2 \dot{S} \cong a_0^2 \dot{q}, \quad q > q_* \quad (48)$$

where δ_2 is given by Equation A61. Equation 48 leads to

$$H = a_0^2 \int_{q_*}^q \frac{dq'}{(H - q' + L)^2} + H_0, \quad q > q_* \quad (49)$$

and

$$S = \frac{a_0^2}{\alpha_2^2} \int_{q_*}^q \frac{dq'}{(S - q' + L)^2} + H_0, \quad q > q_* \quad (50)$$

Equations 49 and 50 give only crude (and probably upper limit) approximations to the effective positions of the layer interface H and the plastic front S as the projectile approaches the interface. Moreover, Equation 50 is reasonable only when $\delta_2 < \delta_1$, i.e., when the distance $S - q + L$ increases to the final value $a_o/\delta_2^{1/3}$ as the projectile enters the second layer. On the other hand, when $\delta_2 > \delta_1$, the distance $S - q + L$ decreases to the final value $a_o/\delta_2^{1/3}$, in which case S is simply located at H until $S - q + L = a_o/\delta_2^{1/3}$.

28. The approximations engendered by placing the effective cavity ($a = a_o$) at the base of the nose require some modification when $q > H$, i.e., when the nose extends beyond the effective interface depth H , as illustrated in Figure 7.

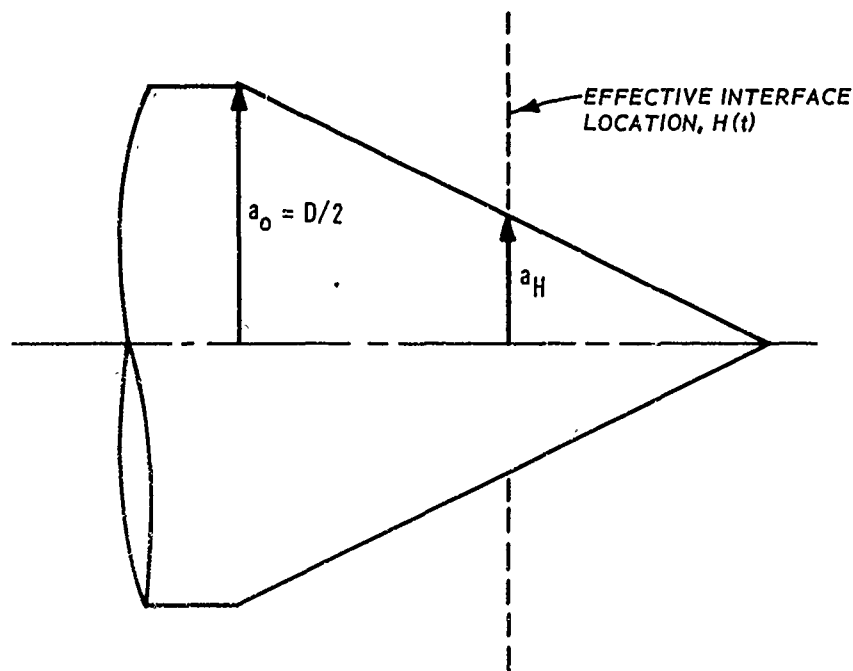


Figure 7. Situation when $q > H$

In such a situation, the frontal area in contact with layer 2 is πa_H^2 , and the frontal area in contact with layer 1 is $\pi(a_o^2 - a_H^2)$. The projectile equation of motion then becomes approximately

$$\left[M + \pi a_o^3 \rho_{l_1} B_1^{(**)} \right] \ddot{q} \cong -\pi a_o^2 \left[p_s^{(**)} + \rho_{l_1} B_2^{(**)} f_n q^2 \right] \quad (51)$$

for $q > H$, where

$$p_s^{(**)} = p_s^{(1)} \left(1 - \frac{a_H^2}{a_o^2} \right) + p_s^{(2)} \frac{a_H^2}{a_o^2}, \quad q < q_* \quad (52)$$

$$B_1^{(**)} = B_1^{(1)} \left(1 - \frac{a_H^3}{a_o^3} \right) + \frac{\rho_{l_2}}{\rho_{l_1}} B_1^{(2)} \frac{a_H^3}{a_o^3}, \quad q < q_* \quad (53)$$

$$B_2^{(**)} = B_2^{(1)} \left(1 - \frac{a_H^2}{a_o^2} \right) + \frac{\rho_{l_2}}{\rho_{l_1}} B_2^{(2)} \frac{a_H^2}{a_o^2}, \quad q < q_* \quad (54)$$

and

$$p_s^{(**)} = p_s^{(*)} \left(1 - \frac{a_H^2}{a_o^2} \right) + p_s^{(2)} \frac{a_H^2}{a_o^2}, \quad q > q_* \quad (55)$$

$$B_1^{(**)} = B_1^{(*)} \left(1 - \frac{a_H^3}{a_o^3} \right) + \frac{\rho_{l_2}}{\rho_{l_1}} B_1^{(2)} \frac{a_H^3}{a_o^3}, \quad q > q_* \quad (56)$$

$$B_2^{(**)} = B_2^{(*)} \left(1 - \frac{a_H^2}{a_o^2} \right) + \frac{\rho_{l_2}}{\rho_{l_1}} B_2^{(2)} \frac{a_H^2}{a_o^2}, \quad q > q_* \quad (57)$$

The quantities $p_s^{(2)}$, $B_1^{(2)}$, and $B_2^{(2)}$ are shear resistance and inertial coefficients for a semi-infinite second layer, given by

$$p_s^{(2)} = -\frac{2}{3} Y_2 \ln \delta_2 + \frac{4}{9} E_{t_2} \left(\frac{\pi^2}{6} - \sum_{n=1}^{\infty} \frac{\sigma_n^H}{H^2} \right) + \frac{4}{3} \beta_2 E_2 \quad (58)$$

$$B_1^{(2)} = 1 - \frac{\alpha_2}{\delta_2^{2/3}} \quad (59)$$

$$B_2^{(2)} = \frac{3}{2} - \frac{\alpha_2}{\delta_2^{2/3}} \left[2 - \frac{(1 - \delta_2)^2}{(1 - \alpha_2)} \right] + \frac{1}{2} \delta_2^{4/3} \left[1 - \frac{\left(1 - \frac{\alpha_2}{\delta_2}\right)^2}{(1 - \alpha_2)} \right] \quad (60)$$

29. When the projectile nose becomes essentially embedded in the second layer, i.e., when $H - q + L \cong a_0$, the equation of motion is approximately

$$\left[M + \pi a_0^3 \rho_{k_2} B_1^{(2)} \right] \ddot{q} \cong -\pi a_0^2 \left[p_s^{(2)} + \rho_{k_2} B_2^{(2)} f_n \dot{q}^2 \right] \quad (61)$$

at $a_0 \cong H - q + L$

which is the same as for a homogeneous semi-infinite target having the same properties as the second layer.

30. When $q < L$, i.e., when the nose is not fully embedded in the first layer of the target, Equations 38-61 still apply except that a_0 is replaced by a_n and L is replaced by q (Figure 5).

Oblique Impact Theory

31. The investigation thus far has disregarded projectile rotation which may occur due to oblique incidence with the target. Consequently, the next step involves a projectile with a conical nose of half-angle ϕ which strikes the target with an initial angle of obliquity ω_0 , as illustrated in Figure 8. The $\bar{X}, \bar{Y}, \bar{Z}$ right-hand, orthogonal coordinate system is fixed at the point of impact on the surface of the target. Figure 9 shows the x, y, z right-hand, orthogonal coordinate system fixed on the projectile nose tip. The z axis coincides with the

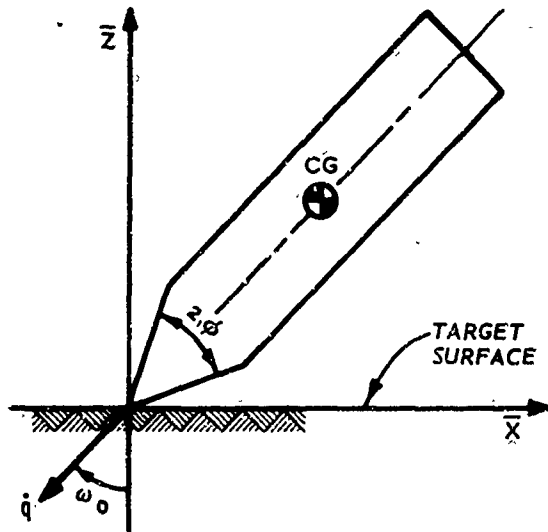


Figure 8. Oblique impact of a projectile with a conical nose

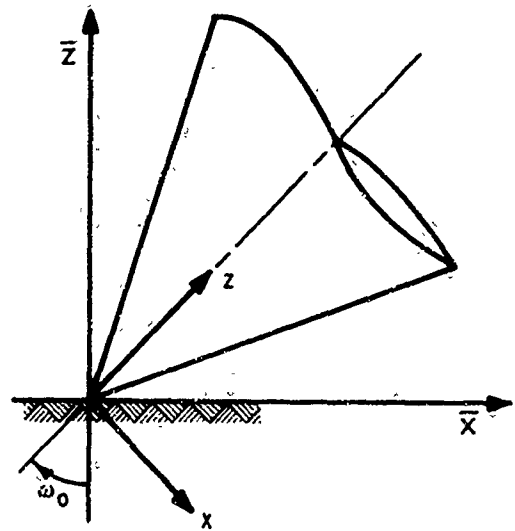


Figure 9. Coordinate systems

projectile axis of symmetry, and at impact the projectile y axis coincides with the fixed \bar{Y} axis. With ω as the instantaneous angle of obliquity, the projectile may undergo rotation during the embedding process due to asymmetric loading over the shaded portion of the nose (Figure 10). The rotation of the projectile about its center of gravity (CG) is now investigated, subject to the following restrictions:

- a. The investigation is limited to the embedding of the nose, and projectile-target interactions aft of the nose are not considered.
- b. The effect of angle of attack upon the stress distribution on the projectile is disregarded.
- c. The location z_G of the CG is aft of the nose, i.e. z_G is greater than L , as shown in Figure 10.
- d. The embedded surface of the nose is assumed to be everywhere in contact with the target.
- e. Finally, the compressive normal stress p_n on the embedded surface of the nose is assumed to be

$$p_n \approx p_s + \rho_l B_2 f_n \dot{q}^2 \quad (62)$$

where \dot{q} is the translational velocity of the CG.

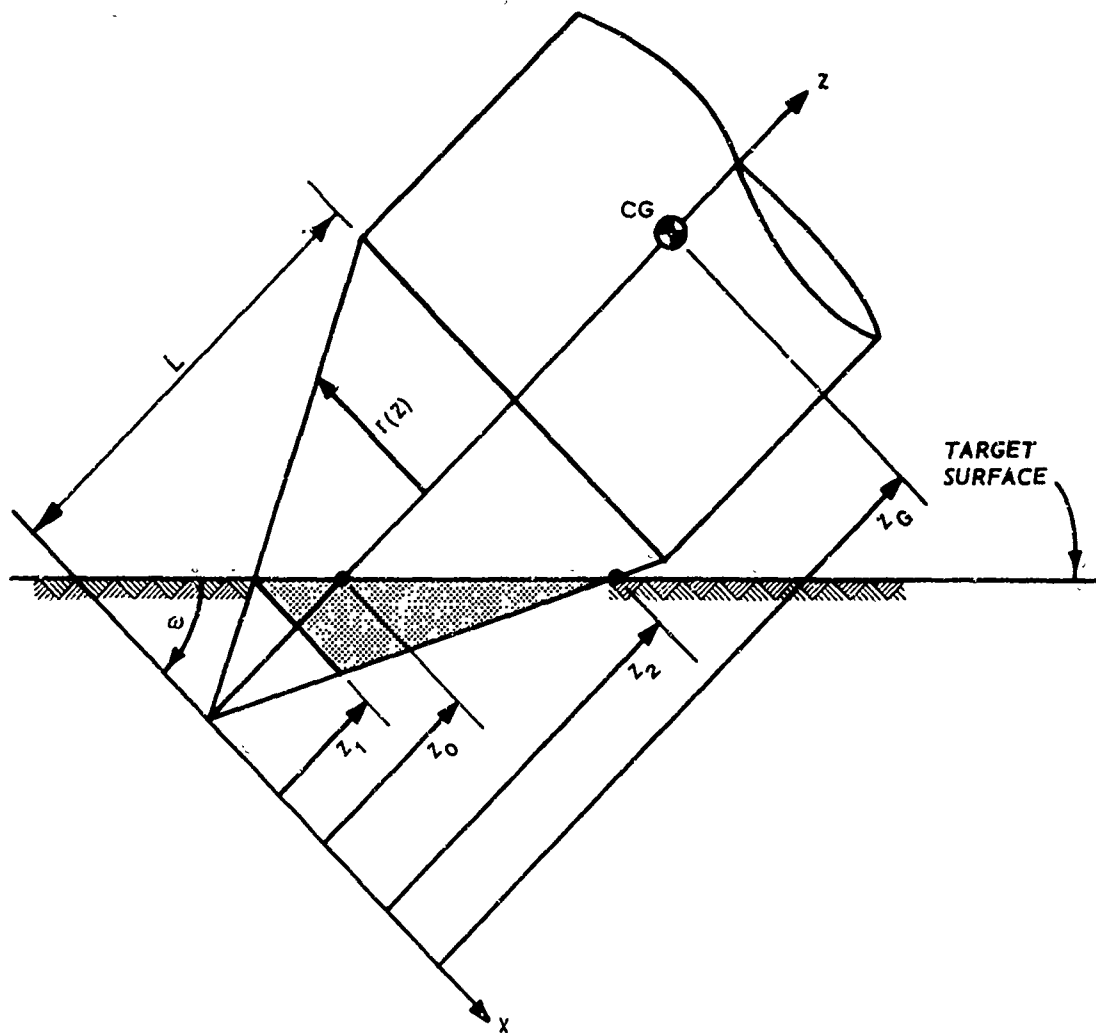


Figure 10. Projectile with conical nose partially embedded at angle of obliquity ω

Equation 62 corresponds approximately to the average compressive normal stress on a partially embedded nose when $R_a \ll 1$ (Equation 37).

32. For computation of forces and moments acting on the projectile, the cone is divided into circular bands of radius $r(z)$ and infinitesimal height dz . However, in the shaded region (Figure 10), only a portion of each band is subjected to p_n , and for each band $r(z)$ there is a limiting azimuthal angle $\psi_{max}(z)$ bounding the arc over which p_n acts. Looking along the projectile axis of symmetry in the direction of positive z and considering a particular band $r(z)$,

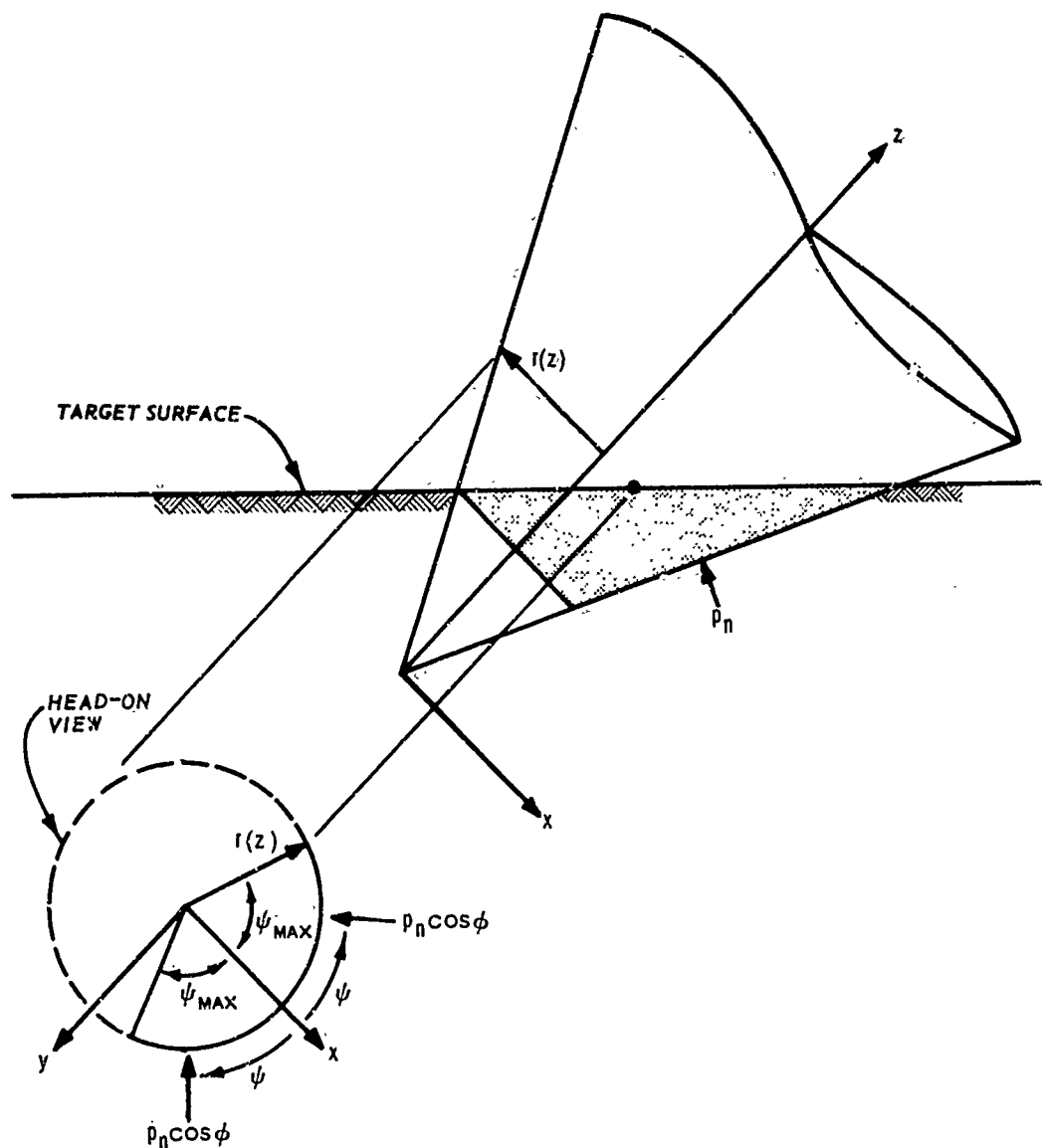


Figure 11. Partially embedded cone with head-on view of circular band $r(z)$

one sees the head-on view shown in Figure 11. The stress p_n acts on both sides of the band from $\psi = 0$ to $\psi = \psi_{\max}$, and the dashed arc represents the portion of the band which is not embedded. (Note that the xz plane is a plane of symmetry in Figures 9-11.) The relation between ψ_{\max} , z , ω , and ϕ is as follows:

$$\cos \psi_{\max} = \frac{z - z_0}{z \tan \phi \tan \omega}, \quad z_1 \leq z \leq z_2 \leq L \quad (63)$$

where

$$z_1 = \frac{z_0}{1 + \tan \phi \tan \omega} \quad (64)$$

$$z_2 = \frac{z_0}{1 - \tan \phi \tan \omega} \quad (65)$$

and z_0 is the point where the projectile axis of symmetry (z axis) intersects the target surface (Figure 10). The infinitesimal moment $d\vec{M}_{CG}$ about the CG due to a force $d\vec{F}$ acting on any infinitesimal portion dA of the cone surface is

$$d\vec{M}_{CG} = \vec{\gamma} \times d\vec{F} \quad (66)$$

where $\vec{\gamma}$ is the moment arm. (The moment arm $\vec{\gamma}$ is a position vector from the CG to the point where the force $d\vec{F}$ acts.) However, since the xz plane is a plane of symmetry, the total vector moment \vec{M}_{CG} about the CG must be perpendicular to the xz plane (i.e., parallel to the y axis). Thus, one need consider only components of $\vec{\gamma}$ and $d\vec{F}$ which lie in the xz plane. The x and z components of $\vec{\gamma}$ are

$$\gamma_x(z, \psi) = z \tan \phi \cos \psi \quad (67)$$

and

$$\gamma_z(z) = z - z_G \quad (68)$$

where

$$z \leq L \leq z_G \quad (69)$$

The x and z components of $d\vec{F}$ acting on an infinitesimal surface element $dA = z dz d\psi / \cos \phi$ are

$$dF_x = -p_n \tan \phi \cos \psi z dz d\psi \quad (70)$$

and

$$dF_z = p_n \tan^2 \phi z dz d\psi \quad (71)$$

Thus, $d\vec{M}_{CG}$ has only one component dM_{CG} , which is parallel to the y axis (a positive moment increases ω) and is given by

$$dM_{CG} = \gamma_z dF_x - \gamma_x dF_z = p_n \tan \phi (z_G - z \sec^2 \phi) z \cos \psi dz d\psi \quad (72)$$

Equations 70-72 are now integrated over the embedded surface of the nose to obtain the x and z components of the resisting force, F_x and F_z , and the total moment M_{CG} :

$$F_x = - \frac{2p_n z_o^2}{\tan \omega} \int_{\xi_1}^{\xi_2} f(\xi) d\xi \quad (73)$$

$$F_z = 2p_n z_o^2 \tan^2 \phi \left[\xi_1^2 + \frac{2}{\pi} \int_{\xi_1}^{\xi_2} \psi_{\max}(\xi) \xi d\xi \right] \quad (74)$$

$$M_{CG} = \frac{2p_n z_o^3}{\tan \omega} \left[\xi_G \int_{\xi_1}^{\xi_2} f(\xi) d\xi - \sec^2 \phi \int_{\xi_1}^{\xi_2} f(\xi) \xi d\xi \right] \quad (75)$$

Where the factor "2" arises in Equations 73-75 due to symmetry about the xz plane, and

$$\xi \equiv \frac{z}{z_o} \quad (76)$$

$$f(\xi) = (2\xi - 1 - \lambda^2 \xi^2)^{1/2} \quad (77)$$

$$\lambda = (1 - \tan^2 \omega \tan^2 \phi)^{1/2} \quad (78)$$

$$\xi_G = \frac{z_G}{z_0} \quad (79)$$

$$\xi_1 = \begin{cases} \frac{1}{(1 + \tan \phi \tan \omega)}, & z_1 \leq L \\ \frac{L}{z_0}, & z_1 > L \end{cases} \quad (80)$$

$$\xi_2 = \begin{cases} \frac{1}{(1 - \tan \phi \tan \omega)}, & z_2 \leq L \\ \frac{L}{z_0}, & z_2 > L \end{cases} \quad (81)$$

and ψ_{\max} , z_1 , and z_2 are given by Equations 63-65. The integral appearing in Equation 74 must be evaluated numerically. The integrals appearing in Equations 73 and 75 are evaluated as follows:

$$\int_{\xi_1}^{\xi_2} f(\xi) d\xi = \left[\frac{\lambda^2 \xi - 1}{2\lambda^2} f(\xi) \right]_{\xi_1}^{\xi_2} + \frac{1 - \lambda^2}{2\lambda^2} \int_{\xi_1}^{\xi_2} \frac{d\xi}{f(\xi)}, \quad \lambda^2 \neq 0 \quad (82)$$

$$\int_{\xi_1}^{\xi_2} \frac{d\xi}{f(\xi)} = \left[\frac{1}{\lambda} \arcsin \left(\frac{\lambda^2 \xi - 1}{\sqrt{1 - \lambda^2}} \right) \right]_{\xi_1}^{\xi_2}, \quad \lambda^2 > 0 \quad (83)$$

$$\int_{\xi_1}^{\xi_2} \frac{d\xi}{f(\xi)} = \left[\frac{1}{\sqrt{-\lambda^2}} \ln \left\{ f(\xi) + \xi \sqrt{-\lambda^2} + \frac{1}{\sqrt{-\lambda^2}} \right\} \right]_{\xi_1}^{\xi_2}, \quad \lambda^2 < 0 \quad (84)$$

$$\int_{\xi_1}^{\xi_2} f(\xi) \xi \, d\xi = \left[-\frac{f^3(\xi)}{3\lambda^2} \right]_{\xi_1}^{\xi_2} + \frac{1}{\lambda^2} \int_{\xi_1}^{\xi_2} f(\xi) \, d\xi, \quad \lambda^2 \neq 0 \quad (85)$$

When $\lambda^2 = 0$, Equations 82 and 85 reduce to:

$$\int_{\xi_1}^{\xi_2} f(\xi) \, d\xi = \left[\frac{1}{3} (2\xi - 1)^{3/2} \right]_{\xi_1}^{\xi_2}, \quad \lambda^2 = 0 \quad (86)$$

$$\int_{\xi_1}^{\xi_2} f(\xi) \xi \, d\xi = \left[\frac{1}{15} (3\xi + 1)(2\xi - 1)^{3/2} \right]_{\xi_1}^{\xi_2}, \quad \lambda^2 = 0 \quad (87)$$

33. During the embedding of the nose ($z_1 \leq L$, Equation 64 and Figure 10), the equations governing translation of the projectile CG are

$$\ddot{MX} = F_x \cos \omega + F_z \sin \omega, \quad 0 \leq z_1 \leq L \quad (88)$$

$$\ddot{MY} = 0, \quad 0 \leq z_1 \leq L \quad (89)$$

$$\ddot{MZ} = F_z \cos \omega - F_x \sin \omega, \quad 0 \leq z_1 \leq L \quad (90)$$

where $\bar{X}, \bar{Y}, \bar{Z}$ is the coordinate system shown in Figures 8 and 9, and F_x and F_z are given by Equations 73 and 74. Likewise, during the embedding of the nose, the rotation of the projectile about the CG is governed by

$$I\ddot{\omega} = M_{CG}, \quad 0 \leq z_1 \leq L \quad (91)$$

where

I = moment of inertia about CG

$\ddot{\omega}$ = angular acceleration

M_{CG} = moment about CG (Equation 75)

The rotational equation of motion (91) is limited to $z_1 \leq L$, and no equation for M_{CG} has been developed for $z_1 > L$. Thus, the present theory of oblique impact is limited to the prediction of obliquity ω and rotational velocity $\dot{\omega}$ for $0 \leq z_1 \leq L$, i.e., the theory considers only those rotations which occur during the embedding of the nose. A realistic theory of deep penetration at finite angles of obliquity should account for aft body effects which are beyond the scope of the present work.

PART III: SOME PARAMETRIC IMPLICATIONS OF PENETRATION THEORY

The Nondimensional Equation of Motion

34. According to the theory developed in Part II, the equation of motion for a projectile which impacts normal to the surface of a homogeneous target is

$$\left(M + \pi a_n^3 \rho_l B_1 \right) \ddot{q} = -\pi a_n^2 \left(p_s + \rho_l B_2 f_n \dot{q}^2 \right) \quad (92)$$

When the ratio R_a is small, Equation 92 reduces to

$$M\ddot{q} \cong -\pi a_n^2 \left(p_s + \rho_l B_2 f_n \dot{q}^2 \right), \quad R_a \ll 1 \quad (93)$$

When the effect of compressibility is small (Appendix B), Equations A89 and A93 are approximated by

$$B_2 \cong \frac{3}{2} \quad (94)$$

and

$$\rho_l \cong \rho \quad (95)$$

Thus, Equation 93 gives way to

$$M\ddot{q} \cong -\pi a_n^2 \left(p_s + \frac{3}{2} \rho f_n \dot{q}^2 \right) \quad (96)$$

Equation 96 is now rewritten as

$$\frac{M\ddot{q}}{\pi a_o^2 p_s} \cong - \frac{a_n^2}{a_o^2} \left(1 + \frac{3\rho f_n \dot{q}^2}{2p_s} \right) \quad (97)$$

By defining the dimensionless quantities

$$u = \frac{\dot{q}^2}{v_o^2} \quad (98)$$

and

$$y = \frac{a}{a_o} \quad (99)$$

where v_o is the impact velocity, Equation 97 then becomes

$$\frac{M\ddot{q}}{2\pi a_o^3 p_s} = \frac{Mv_o^2}{2\pi a_o^3 p_s} \frac{du}{dy} \cong - \frac{a}{a_o} \frac{n}{2} (1 + f_n G_o u) \quad (100)$$

where

$$G_o \equiv \frac{\rho_l B_o v_o^2}{p_s} \cong \frac{3\rho v_o^2}{2p_s} \quad (101)$$

The quantity G_o characterizes the ratio of maximum inertial resistance to shear resistance within the context of the cavity expansion and penetration theories presented in the present work. Since p_s is primarily a function of the target yield strength Y for the elastic-plastic case (Equation A96), Equation 101 suggests another ratio,

$$R_s \equiv \frac{\rho \dot{q}^2}{Y} \quad (102)$$

The ratio R_s is analogous to the so-called Reynolds number used in fluid mechanics, in that it represents an order of magnitude index of the ratio of inertial forces to shear forces in the target. Thus, the ratio R_s will henceforth be referred to as the "solid Reynolds number."

35. For many metals and earth materials, the practical range of p_s is $2Y \lesssim p_s \lesssim 5Y$, so that at impact ($\dot{q} = v_o$) the range of R_s is $G_o \lesssim R_s \lesssim 3G_o$. Using the symbol \sim to relate quantities which are of the same order of magnitude, it is appropriate to write

$$R_s \sim G_o \quad (103)$$

The quantity $M\ddot{q}/\pi a_{op_s}^2$ in Equation 100 represents a nondimensional acceleration (or force). Integrating Equation 100 from $y = 0$ to the final nondimensional penetration depth $y_p = q_p/a_o$, the following equation results:

$$y_p = \frac{1}{3f_n R_a} \ln(1 + f_n G_o u_1) + 2\zeta, \quad y_p \geq 2\zeta \quad (104)$$

where

$$u_1 = \left(1 + \frac{1}{f_n G_o}\right) e^{-6R_a f_n f_v \zeta} - \frac{1}{f_n G_o} \quad (105)$$

$$f_v = \frac{1}{3} \text{ for cones, and} \quad (106)$$

$$f_v = \frac{(2 - 2\epsilon + \epsilon^2) \sqrt{2\epsilon - \epsilon^2} - \frac{1}{3} (2\epsilon - \epsilon^2)^{3/2} - (1 - \epsilon) \arctan\left(\frac{\sqrt{2\epsilon - \epsilon^2}}{1 - \epsilon}\right) - (1 - \epsilon)^2 \sqrt{2\epsilon - \epsilon^2}}{\epsilon^2 \sqrt{2\epsilon - \epsilon^2}} \quad (107)$$

for ogives. The quantity ϵ is defined in Part II, Equation 35, and $\zeta = L/D$. After Equation 100 is solved explicitly for $u(y)$, the following equations are obtained for the acceleration of a projectile with a conical nose:

$$\frac{M\ddot{q}}{\pi a_{op_s}^2} = -(1 + f_n G_o u_1) e^{-3R_a f_n (y-2\zeta)}, \quad y \geq 2\zeta \quad (108)$$

$$\frac{M\ddot{q}}{\pi a_{op_s}^2} = -(1 + f_n G_o) \frac{y^2}{4\zeta^2} e^{-R_a f_n y^3/4\zeta^2}, \quad y \leq 2\zeta \quad (109)$$

Similar but more lengthy expressions can be obtained for ogives. For Equations 104 and 108 to be applicable, it is obvious that the projectile must penetrate at least one nose length L . After having integrated the approximate equation of motion (100) in nondimensional form, it is now possible to examine explicitly the roles of the parameters G_o , R_s , R_a , and $\zeta = L/D$. Furthermore, while the added mass term

$\pi a_0^3 \rho_t B_1$ has been neglected in Equations 93-109, the ratio R_a still appears as a parameter in the nondimensional final depth of penetration $y_p = q_p/a_0$, Equation 104.

The Shape of the Deceleration Curve

36. Probably the most stringent test of the present penetration theory lies in the comparison of predicted deceleration versus depth or time with experimental observations and with the results of detailed two-dimensional finite-difference calculations, where available. For the moment, however, attention is focused on the shape of the deceleration curve in order to make a qualitative comparison with experimental results. Projectiles with conical noses are amenable to such an examination because of the simplicity of Equations 108 and 109, but it is emphasized that similar results can be obtained for ogives.

37. The deceleration curve has the same general shape whether depth or time is chosen as the abscissa. The overall shape of the curve is strongly dependent on $G_0 \sim R_s$ and on $\zeta = L/D$. This is illustrated in Figures 12 and 13. The increasing portion of the curve corresponds to the embedding of the nose, and the decreasing portion corresponds to a fully embedded nose. Examination of experimental results^{14,15,16} reveals that many observed deceleration curves tend to be somewhat flat after the nose becomes embedded in the target, thus having the general shape of the curves in Figure 12 (at least for earth penetration), but the rapid decay shown in Figure 13 is rarely seen. The present penetration theory leads to reasonably accurate predictions of final penetration depth for $0 < R_s \lesssim 100$, but only the average value of the deceleration is correctly predicted when R_s is significantly greater than one. Moreover, the theory apparently overpredicts the instantaneous target inertial resistance during the early part of the penetration process, and the magnitude of this overprediction increases as R_s increases from one. The net result is that the theory tends to underpredict final penetration depths when R_s is very large at impact.

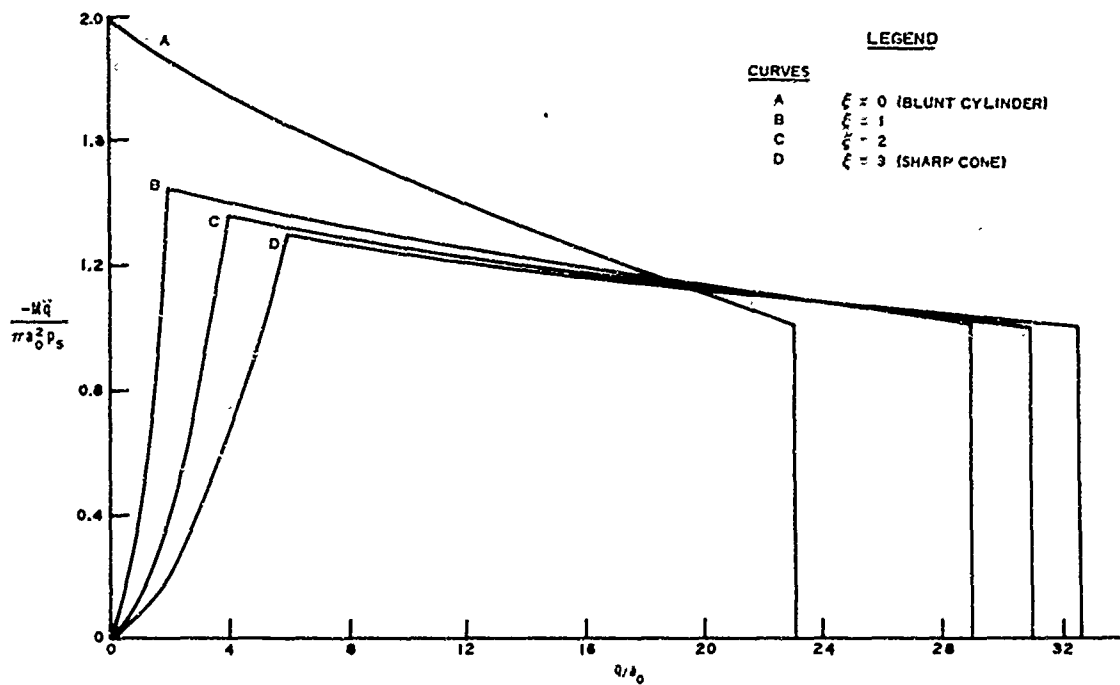


Figure 12. Nondimensional deceleration versus depth,
 $R_s \sim G_0 = 1$, $R_a = 0.01$

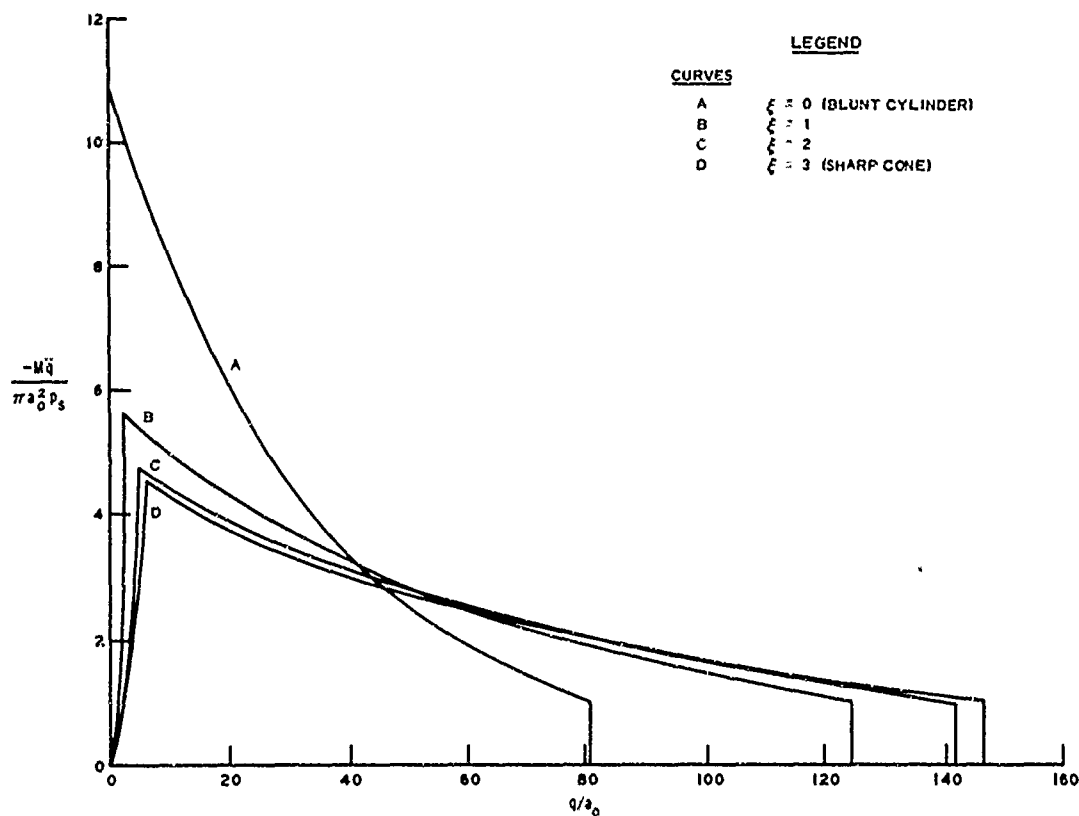


Figure 13. Nondimensional deceleration versus depth,
 $R_s \sim G_0 = 10$, $R_a = 0.01$

The Relative Effects of Nose Shape and Frontal Loading
on Final Depth of Penetration

38. In the context of the present penetration theory, the effect of nose shape is coupled with the effects of R_a and $G_o \sim R_s$, so that the final depth of penetration will not be proportional to some function of nose shape alone. The nose performance ratio R_n is now defined as

$$R_n \equiv \frac{q_p}{q_{pb}} \quad (110)$$

where q_p is the final depth of penetration for a projectile with a given nose shape, and q_{pb} is the corresponding quantity for an otherwise identical blunt cylinder ($\zeta = 0$). Combining Equations 104 and 110 leads to

$$R_n = \frac{\ln(1 + f_n G_o u_1) + 6\zeta f_n R_a}{f_n \ln(1 + G_o)}, \quad q_p > L \quad (111)$$

where u_1 is given by Equation 105. In Figures 14-17, R_n is plotted versus ζ for cones and ogives with R_a and G_o as parameters. Figures 14 and 16 correspond to shallow penetration depths on the order of a few nose lengths, and Figures 15 and 17 correspond to depths several times deeper than Figures 14 and 16. The values $R_a = 0.1$ and $R_a = 0.001$ were chosen to conform approximately to the upper and lower limits of R_a in penetration tests conducted by Sandia Laboratories,^{15,16} and the value $R_a = 0.01$ represents an intermediate value. For comparison Young's empirical correlation² is included in Figures 14-17. Young's linear relation between ζ and final depth of penetration was deduced from earth penetration data for a variety of projectiles and impact conditions and represents something of an overall average nose shape effect.²

39. The present theory results in a nose shape effect which becomes more pronounced as R_a increases. This simply means that, for a given projectile diameter, a sharp nose is less effective for a heavy projectile than for a light projectile as far as depth of penetration is

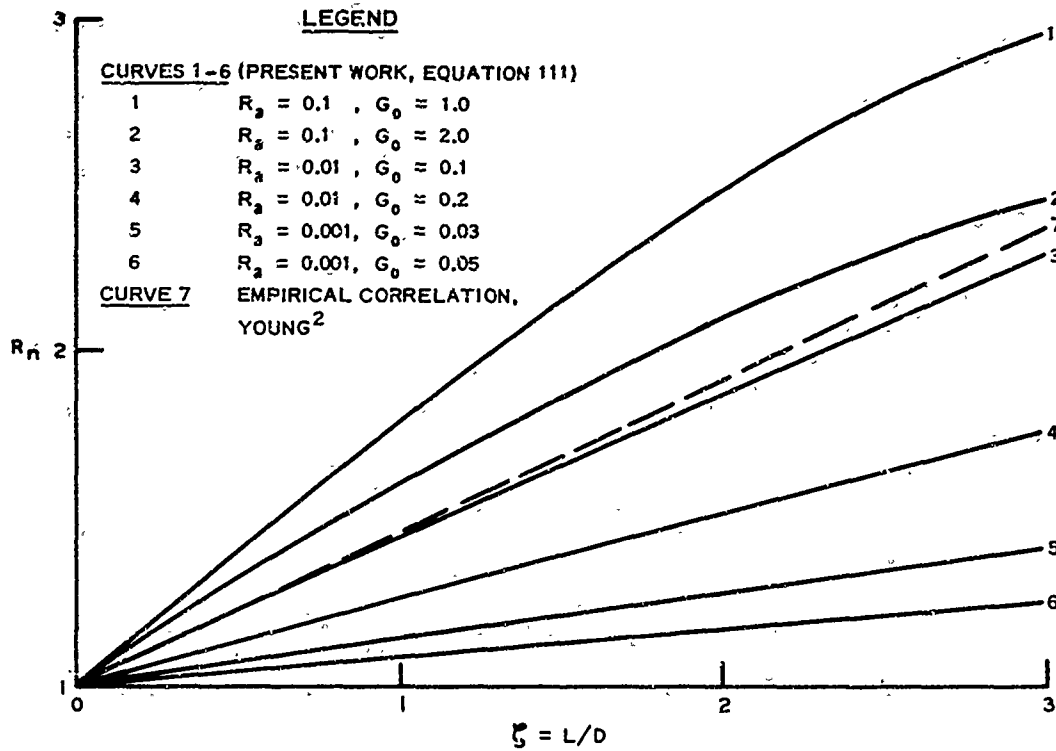


Figure 14. Nose performance ratio for cones, "shallow" penetration

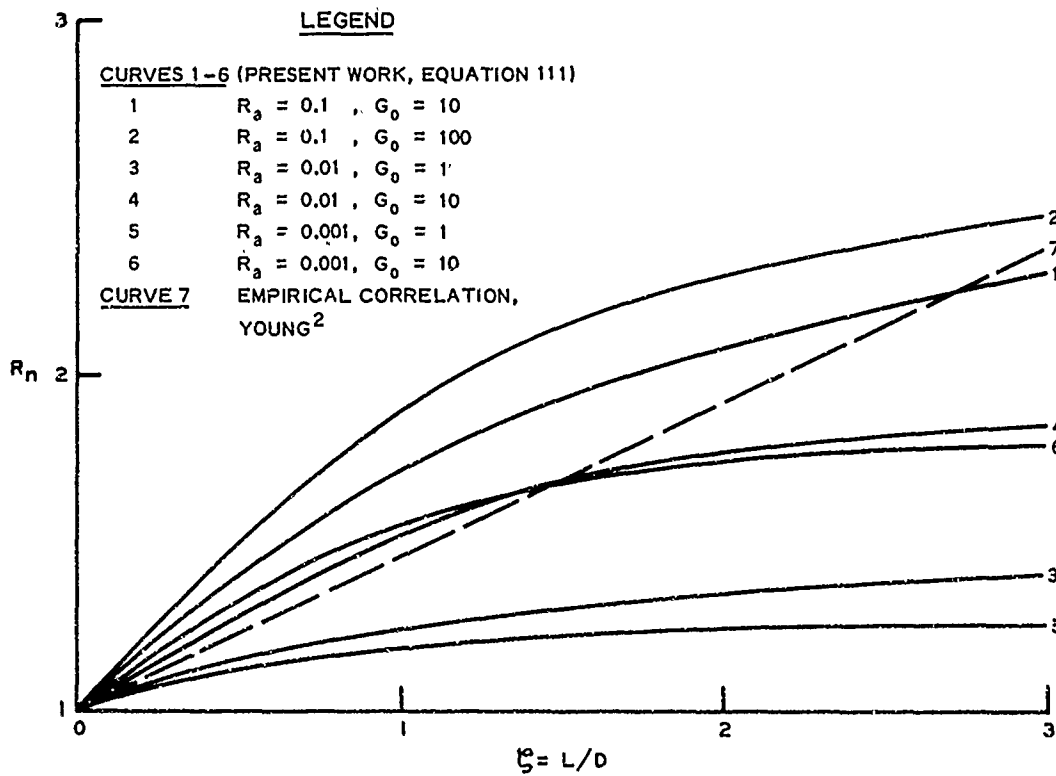


Figure 15. Nose performance ratio for cones, "deep" penetration

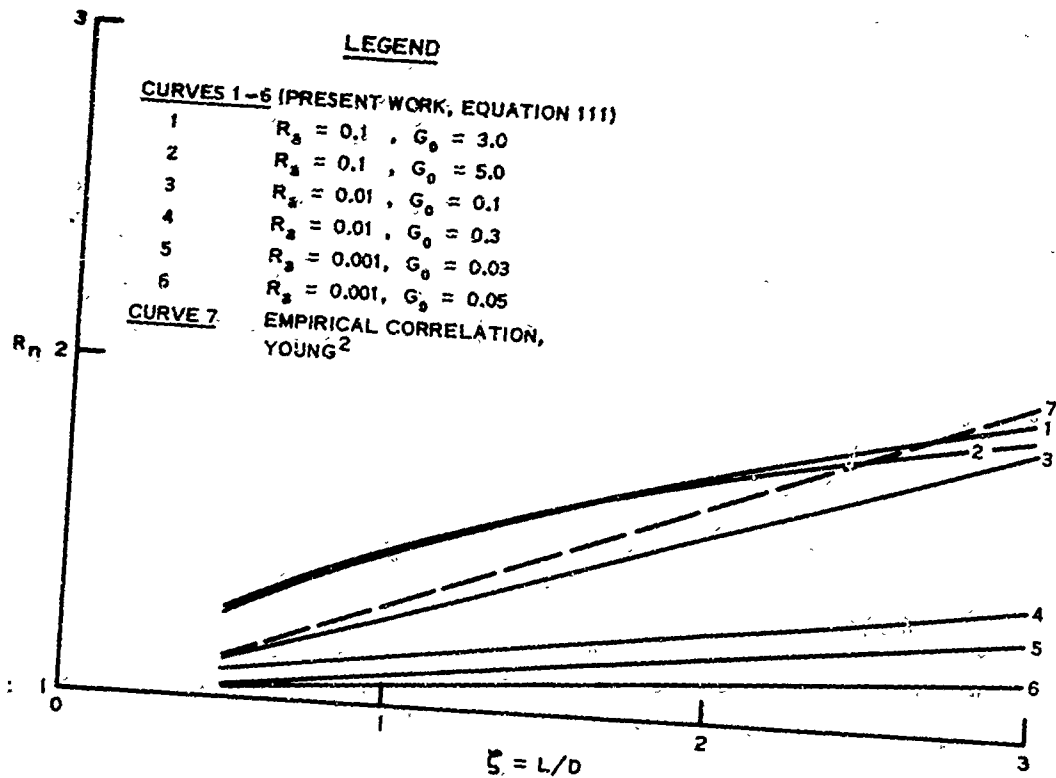


Figure 16. Nose performance ratio for ogives, "shallow" penetration

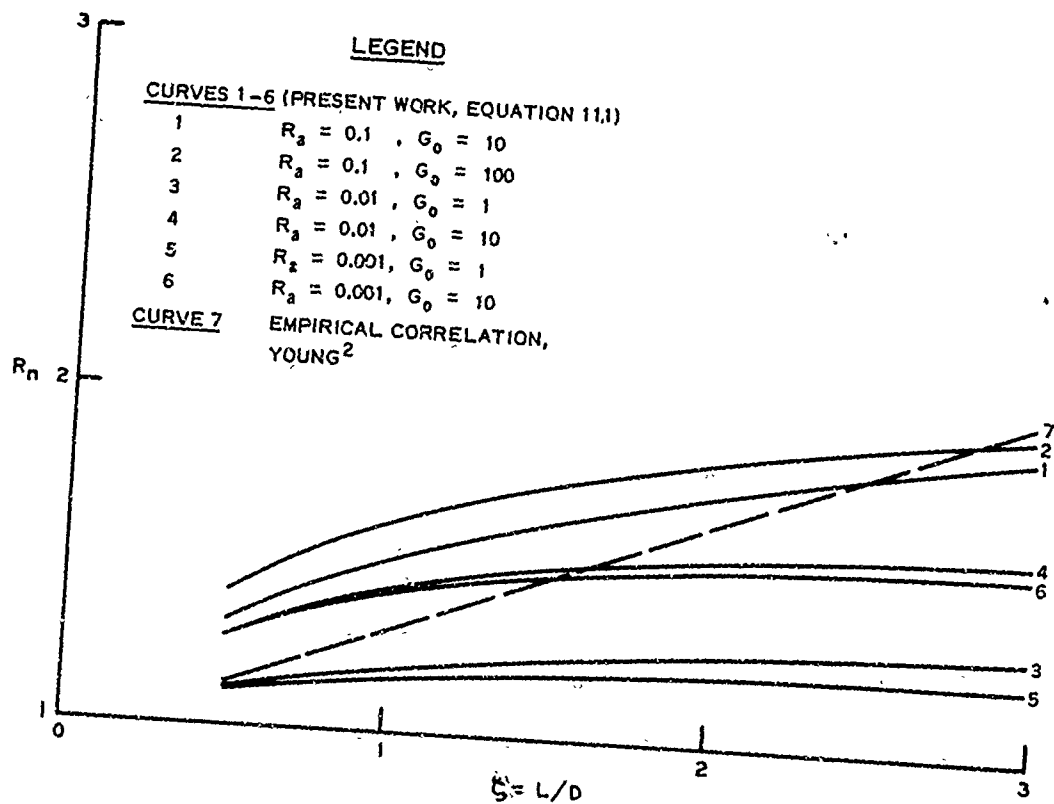


Figure 17. Nose performance ratio for ogives, "deep" penetration

concerned. The present theory also infers that nose shape is more effective in shallow penetration where the embedding of the nose constitutes a significant portion of the penetration process.

40. There have been various attempts to ascertain the relation between final penetration depth and frontal loading $W/\pi a_0^2 \equiv W/A$, where W is the projectile weight and A is the projected frontal area. Young's empirical correlation, for example, infers that final penetration depth is proportional to the square root of W/A . The present theory, on the other hand, yields an approximate linear relation between final (dimensional) penetration depth and W/A for depths greater than one nose length (Equation 104).

Parametric Differences Between Theoretical and Empirical Results for Homogeneous Targets

41. Within the context of the present penetration theory, it is evident that, for the penetration of homogeneous targets, final penetration depth is approximately proportional to W/A and to the natural log of the square of the impact velocity. Furthermore, the effect of nose shape is coupled with the effects of W/A , impact velocity, and target constitutive properties. Young's empirical equation for final penetration depth,² however, indicates that the final depth is proportional to nose length, impact velocity, and the square root of W/A regardless of target properties. Moreover, the relative penetrability of the target is characterized by a single multiplicative constant which must be derived from penetration experiments. Although Young's equation may correctly reflect the relative effects of impact velocity, nose shape, and W/A , it represents a statistical correlation of experimental observations and offers little explanation in terms of underlying physical phenomena. On the other hand, the present penetration theory is based on certain assumptions about the underlying physical processes but produces trends somewhat different from Young's equation. Even though the theory is "rationally" based, it may not be sufficiently

realistic; a more realistic theory might result in trends similar to those exhibited by Young's equation.

Penetration of Layered Targets

42. The relatively complex treatment of the layered target in Part II is important for predicting projectile loading when the initial layer thickness is comparable to the projectile nose dimensions and/or when the layers have extremely different properties. On the other hand, when the layers are thick and have fairly similar properties, final depth predictions which approximate the results of the layered target theory can be obtained simply by using the theory for homogeneous targets and changing the material property input when the projectile reaches a layer interface.

PART IV: APPLICATIONS OF PENETRATION THEORY

Introduction

43. The penetration theory presented in Part II is relatively simple compared with two-dimensional finite-difference analyses. In order to demonstrate in part the applicability of the theory as an engineering tool, theoretical results will be compared with two-dimensional finite-difference solutions, empirical results, and experimental observations. However, before these comparisons are made, some comments are in order:

- a. Although the ratio $R_a \ll 1$ in all the examples to be presented, the added mass term $\pi a^3 \rho_0 B_1$ will be retained as an upper limit on the effect of target acceleration.
- b. It will be shown that the solid Reynolds number R_s provides a simple rule of thumb which indicates whether or not the present theory is appropriate for a particular penetration problem.
- c. Material properties and impact conditions are given in both U. S. customary and metric (SI) units in the text, but graphic presentation of results is given in U. S. customary units to expedite comparison with other work.

Choice of Material Properties

44. The cavity expansion theory presented in Appendix A and the penetration theory developed in Part II are restricted to materials which exhibit bilinear behavior in shear, as shown in Figure A2. Moreover, the assumption of rate-independent shear behavior is implicit in the theoretical development. Real materials exhibit neither bilinear shear behavior nor rate-independence, and the guidelines to be followed when the present penetration theory is applied to real targets are:
(a) bilinear stress-strain curves should be chosen so as to approximate the total area under experimentally obtained stress-strain curves, up to

the point where complete failure occurs (i.e., where the slope becomes negative); and (b) when predictions are to be made prior to the penetration of an untried target, it is best to make two sets of calculations corresponding to the upper and lower bounds on Y , E , and E_t . Lower bound properties can be obtained from the results of static tests, while upper bound properties must be estimated from the results of dynamic tests.

Penetration of Rock

45. Thigpen⁷ has performed two-dimensional finite-difference calculations analyzing the penetration of a nonrigid projectile into Madera limestone and welded tuff. The present penetration theory is applied to the same problems for a rigid but otherwise identical projectile. Following Thigpen, the targets are idealized as compressible elastic-plastic continua of the von Mises type (compressive yield strength Y independent of pressure). For the range of dynamic pressures considered ($P \lesssim \rho v_0^2$), the relation between pressure and density is

$$\rho_\ell \cong \rho \left(1 + \frac{P_{\text{ave}}}{\rho C_0^2} \right) \quad (112)$$

where P_{ave} is average dynamic pressure in the plastic zone (Appendix B), and C_0 is initial sound speed. The modulus E is essentially constant for the range of pressures examined. For the limestone,

$$\rho = 168 \text{ pcf}^* (2.69 \text{ gm/cm}^3)$$

$$E \cong 3.15 \times 10^6 \text{ psi} (217 \text{ kbar})$$

$$Y = 1.37 \times 10^4 \text{ psi} (0.945 \text{ kbar})$$

* A table of factors for converting U. S. customary units of measurement to metric (SI) units is presented on page 4.

and

$$C_o = 1.12 \times 10^4 \text{ fps } (3.41 \times 10^3 \text{ m/sec})$$

For the tuff,

$$\rho = 115 \text{ pcf } (1.84 \text{ gm/cm}^3)$$

$$E \cong 1.09 \times 10^6 \text{ psi } (75.2 \text{ kbar})$$

$$Y = 5.51 \times 10^3 \text{ psi } (0.380 \text{ kbar})$$

and

$$C_o = 6.72 \times 10^3 \text{ fps } (2.05 \times 10^3 \text{ m/sec})$$

For limestone penetration,

$$W = 674 \text{ lb } (306 \text{ kg})$$

$$D = 8 \text{ in. } (20.3 \text{ cm})$$

$$L/D = 3.0 \text{ (9.25 CRH)}$$

and

$$v_o = 570 \text{ fps } (174 \text{ m/sec})$$

For tuff penetration,

$$W = 1000 \text{ lb } (454 \text{ kg})$$

$$D = 9 \text{ in. } (22.9 \text{ cm})$$

$$L/D = 2.4 \text{ (6.0 CRH)}$$

and

$$v_o = 695 \text{ fps } (212 \text{ m/sec})$$

46. The predictions of the present penetration theory are compared with Thigpen's results in Figures 18 and 19. Thigpen's deceleration curves correspond to the motion of a particle on the projectile axis of symmetry; in Figure 18 the particle is located 2 ft (61 cm) aft

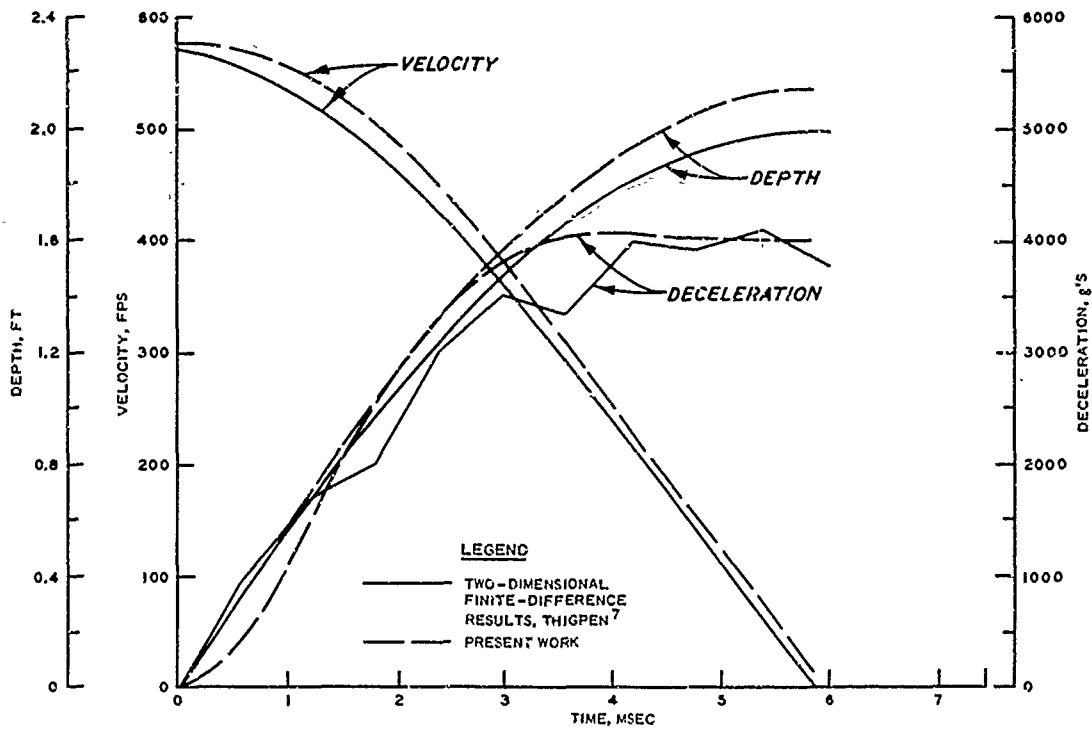


Figure 18. Motion curves for penetration into limestone

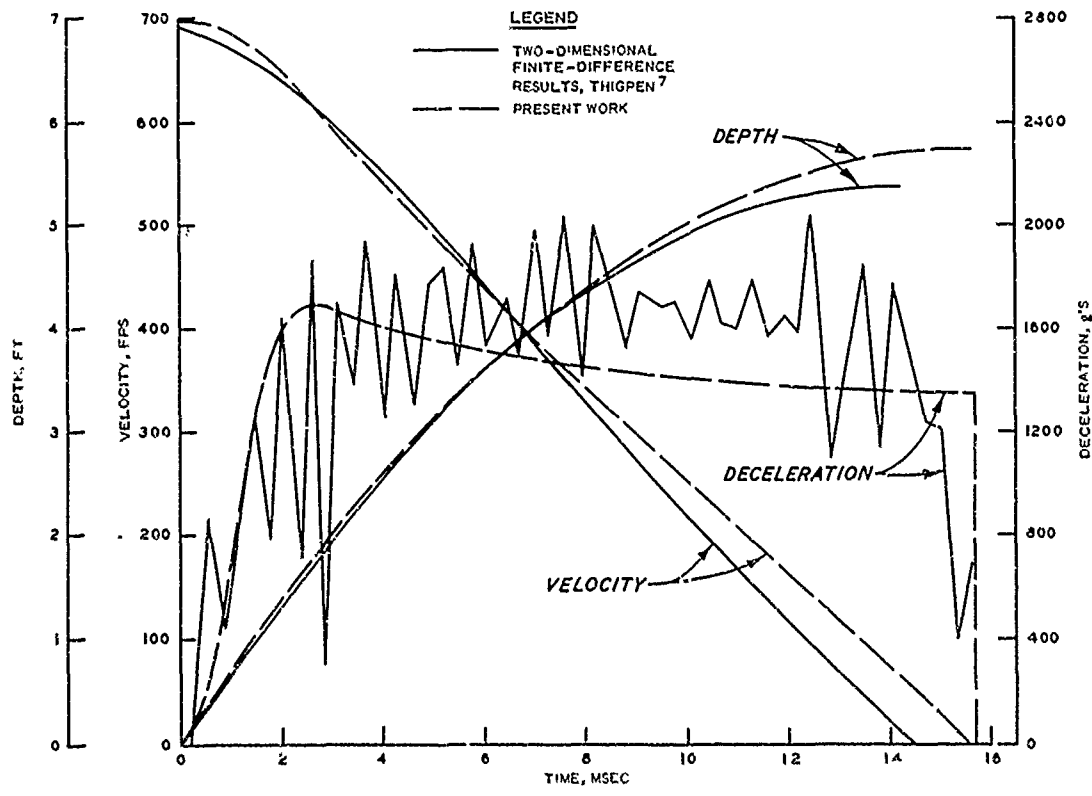


Figure 19. Motion curves for penetration into tuff

of the nose tip, and in Figure 19 the particle is located at the base of the nose. The oscillation in Thigpen's deceleration curves is due to nonrigidity of the projectile.⁷ It is important to observe that in these calculations the target shear resistance is very significant since the values of R_s at impact are 0.86 and 2.17 for the limestone and tuff, respectively. Moreover, the agreement with Thigpen's results apparently provides justification for using p_s to characterize average shear resistance to penetration, at least for homogeneous targets and low values of R_s .

Penetration of Concrete

47. Another test of the present penetration theory lies in the comparison of theoretical predictions with those of empirical penetration equations. A fairly accurate empirical equation for the penetration of armor piercing (AP) and semi-armor piercing (SAP) bombs into reinforced concrete is given by¹⁷

$$q_p = \frac{222WD^{0.215}}{A\sqrt{Y}} \left(\frac{v_o}{1000} \right)^{1.5} + 0.5D \pm 15\% \quad (113)$$

with q_p in inches, W in pounds, A in square inches, D in inches, Y in psi, and v_o in fps. Equation 113 is now used to predict the penetration of a 2000-lb (907-kg) AP bomb into reinforced concrete,¹⁸ with $Y = 5000$ psi (0.345 kbar), $E = 4.10 \times 10^6$ psi (283 kbar), and $\rho = 150$ pcf (2.4 gm/cm³). For the penetration theory predictions, the modulus E_t is taken to be zero, and the value of Y is the static value (5000 psi) as in Equation 113. In addition, the pressure-density curve in Figure 20 is used according to the procedure outlined in Appendix B and represents typical behavior of concrete under pressure. The bomb has $D = 13.5$ in. (34.3 cm) and $L/D = 1.12$ (1.5 CRH). Normal impact velocities range from 500 to 1500 fps (152 to 457 m/sec). Two sets of theoretical predictions are made, corresponding to the compressible and incompressible cases. These are compared with the results

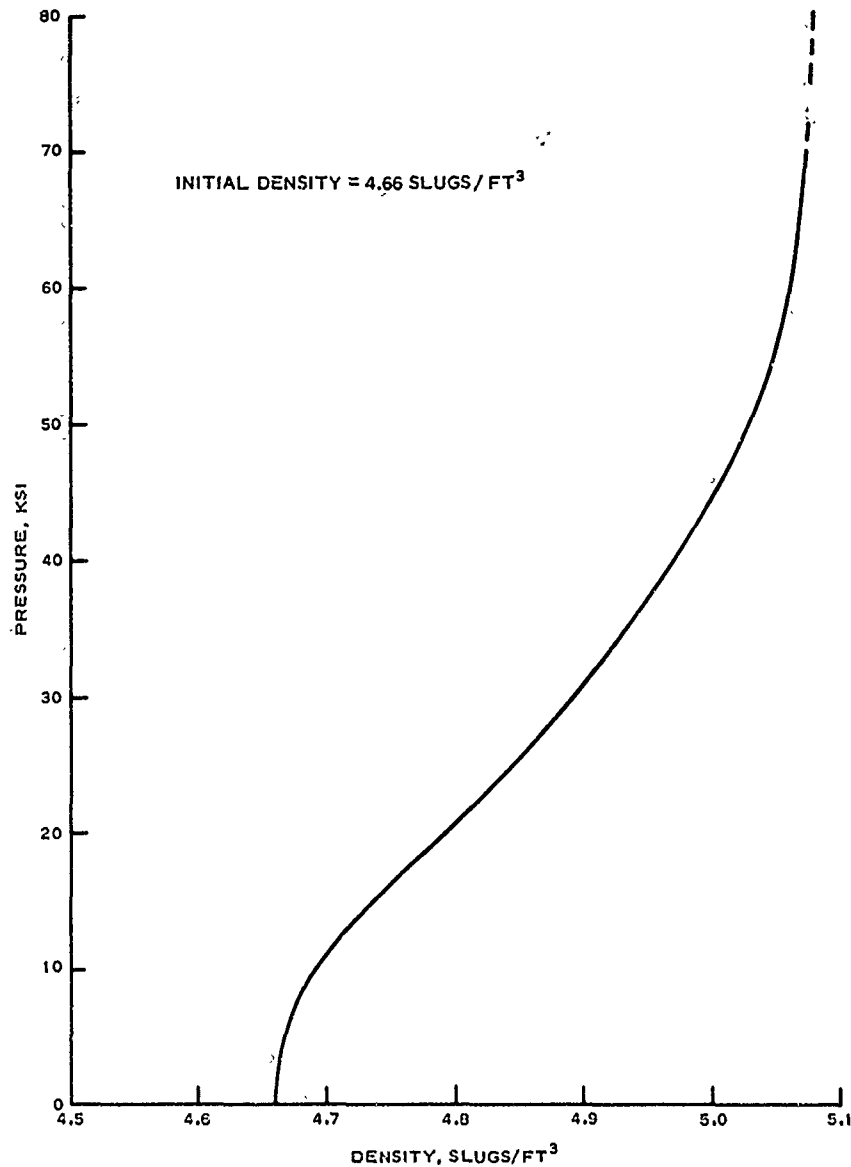


Figure 20. Typical pressure-density relation for concrete (1 ksi = 1000 psi)

of Equation 113 in Figure 21. Since the penetration theory predictions are made using the static value of Y , they should be regarded as upper bounds on predicted penetration depth. The results in Figure 21 correspond to impact values of R_s in the range $1 \lesssim R_s \lesssim 15$, in which the inertial resistance of the target begins to predominate over the shear resistance. Moreover, the agreement with Equation 113 provides some justification for using the theory in this range of values of R_s .

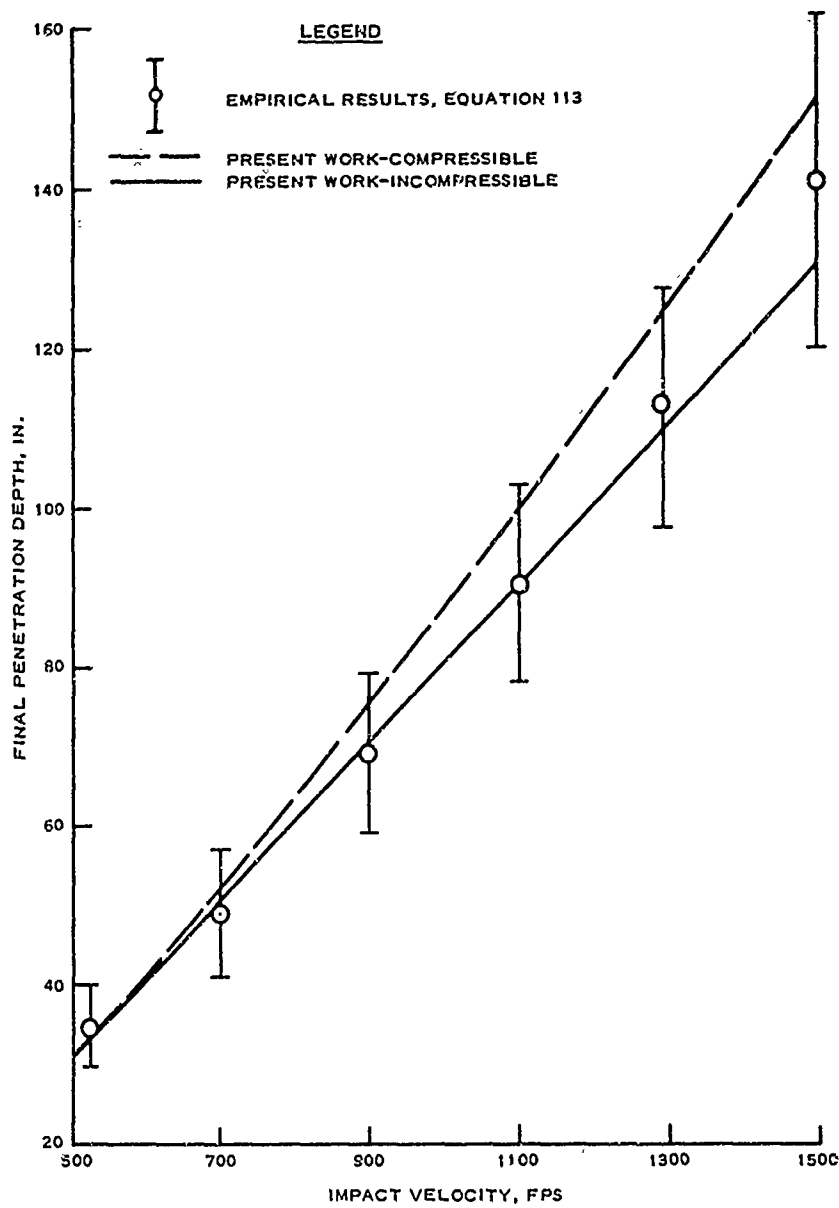


Figure 21. Penetration depth versus impact velocity for penetration of concrete by a 2000-lb AP bomb

Penetration of Soft Earth

48. As an example of penetration into soft earth, the normal impact of a terminal delivery vehicle (TDV) into moist, sandy clay is considered. The target is one of the range areas at Jefferson Proving

Ground, Indiana.¹⁹ The TDV has a total weight of 17.3 lb (7.85 kg), but when the full length of the projectile is embedded in the target, the projectile base separates, remaining at the target surface and reducing the projectile weight to 13.6 lb (6.17 kg). The diameter of the projectile is 3 in. (7.62 cm), the total projectile length is 17.7 in. (45.0 cm), and the nose is an ogive, $L/D = 1.45$ (2.35 CRH). For the target, $Y = 50$ psi (3.45 bar), $E = 3000$ psi (207 bar), and $E_t = 0$, obtained from dynamic unconfined compression tests.¹⁹ The undisturbed target density $\rho = 3.88$ slugs/ft³ (2.00 gm/cm³). Experimental impact velocities range from 350 to 610 fps (107 to 186 m/sec) corresponding to $65 \lesssim R_s \lesssim 200$. Since no pressure-density curve is available for the target, two sets of calculations are presented, corresponding respectively to the incompressible case and the compressible case for $\rho_c = 1.1\rho$ (probably representing a high upper limit on the effect of compressibility). The theoretical predictions are compared with experimental results in Figure 22. Since the experimental data are quite scattered, it is difficult to come to any definite conclusions from this comparison. However, within the framework of the theory, the incompressible calculation is probably the more realistic of the two, although the predicted depths are somewhat low compared to the experimental results. Viewed in this light, the results seem to indicate that $R_s \sim 100$ may represent an approximate upper limit on the range of applicability of the present penetration theory.

Perforation of a Metal Slab

49. Perhaps the most stringent test which can be applied to the penetration theory for layered targets developed in Part II is a situation in which the first layer is thin with extremely different properties from the second layer. Such a situation exists when a steel projectile with a diameter of 0.3 in. (0.762 cm) strikes a 6061-T6 aluminum slab with a thickness of 1 in. (2.54 cm). This, of course, represents a case where the first layer is aluminum and the second layer is air. Using the HEMP code, Wilkins²⁰ has performed a two-dimensional

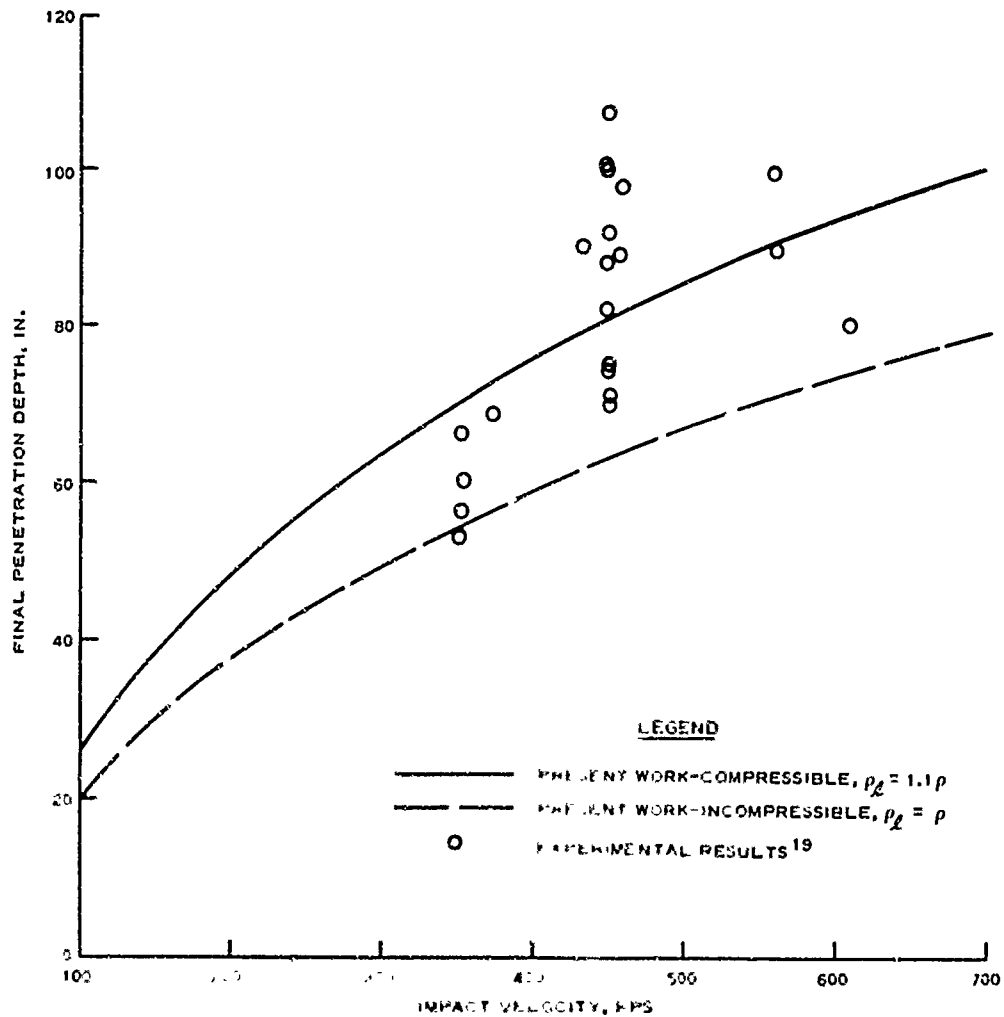


Figure 22. Penetration depth versus impact velocity for penetration of soft earth by a terminal delivery vehicle

finite-difference analysis of the perforation of 1-in.-thick aluminum slab by a 0.3-in.-diam steel projectile. The projectile has a conical nose, $L/D = 1$, a weight of 0.0183 lb (8.30 gm), and a normal impact velocity of 2756 fps (840 m/sec). For the aluminum, $\rho = 5.25$ slugs/ft³ (2.7 gm/cm³), $Y = 43,500$ psi (3 kbar), $E = 1.03 \times 10^7$ psi (710 kbar), and $E_t = 0$. The pressure-density relation is Equation 112 with $\rho C_o^2 = 1.24 \times 10^7$ psi (775 kbar). The properties of air are considered negligible compared to those of aluminum. According to Wilkins, the projectile perforates the slab with an exit velocity equal to 81 percent of the impact velocity. This represents a projectile momentum loss of

19 percent and a kinetic energy loss of 34.4 percent. The present penetration theory for layered targets has been applied to the same problem, and the results are presented in Figures 23-26. The crucial test of the theory lies in its ability to predict projectile kinetic energy loss during the perforation process. The incompressible theory yields an energy loss of 54 percent, and the compressible theory reduces this to 52 percent, essentially the same answer. Thus, the present theory overpredicts Wilkins' value for the energy loss by a minimum factor of 1.51. Two possible sources of error are immediately apparent: First, as is pointed out in Part III, paragraph 37, the theory apparently overpredicts the initial target inertial resistance when the value of R_s is significantly greater than one at impact (in this case, $R_s = 6.29$ at impact). Second, the target is always assumed to be in a compressive state of stress; however, it is well known that because the backside of the slab is a free surface, a finite region in the slab may be in a tensile state of stress during the perforation process, thus reducing the overall penetration resistance.

50. Within the framework of the theory as it stands, there is little that one can do about the suspected region of tensile stress, and this may represent a permanent limitation on the theory. On the other hand, the question of inertia is a bit more straightforward. Accordingly, a third calculation is presented in which the target is assumed incompressible, and the inertial terms in the projectile equation of motion are discarded altogether. For this case, the predicted energy loss is 32 percent, slightly underpredicting Wilkins' value of 34.4 percent. This does not necessarily mean that all the target resistance is due to shear. However, it may indicate that the theory does a better job of predicting target shear resistance than predicting target inertial resistance. In any case, it is emphasized that the present theory is developed not as a perforation theory, per se, but as a penetration theory for layered targets. For most cases of practical interest, the layers will have comparable densities (i.e. comparable inertial resistance) even though other properties may be radically different. Since the application of the layered-target theory to a perforation problem

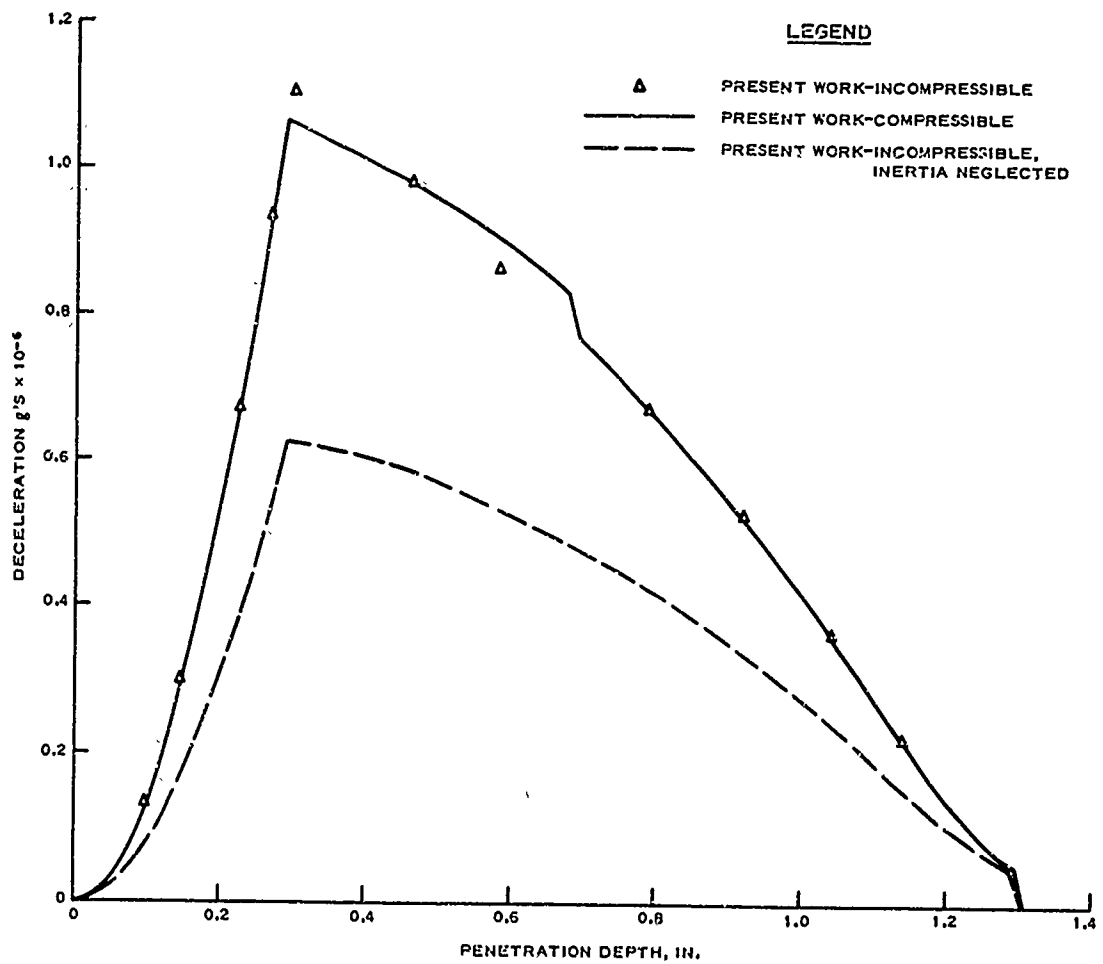


Figure 23. Projectile deceleration versus depth for perforation of 1-in.-thick aluminum slab

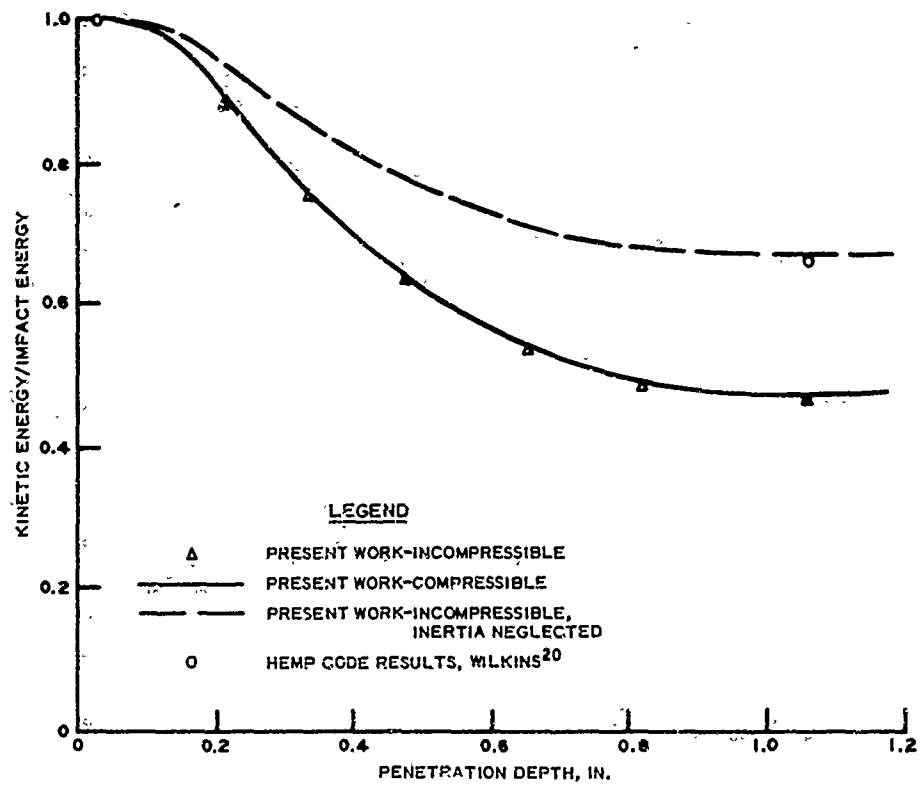


Figure 24. Projectile kinetic energy versus depth for perforation of 1-in.-thick aluminum slab

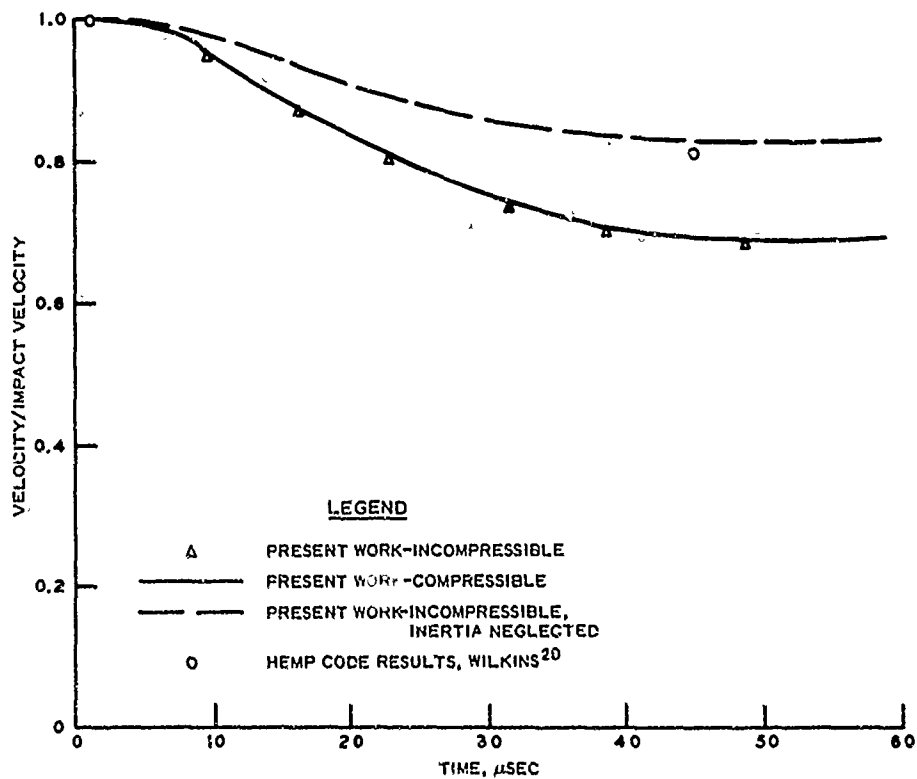


Figure 25. Projectile velocity versus time for perforation of 1-in.-thick aluminum slab

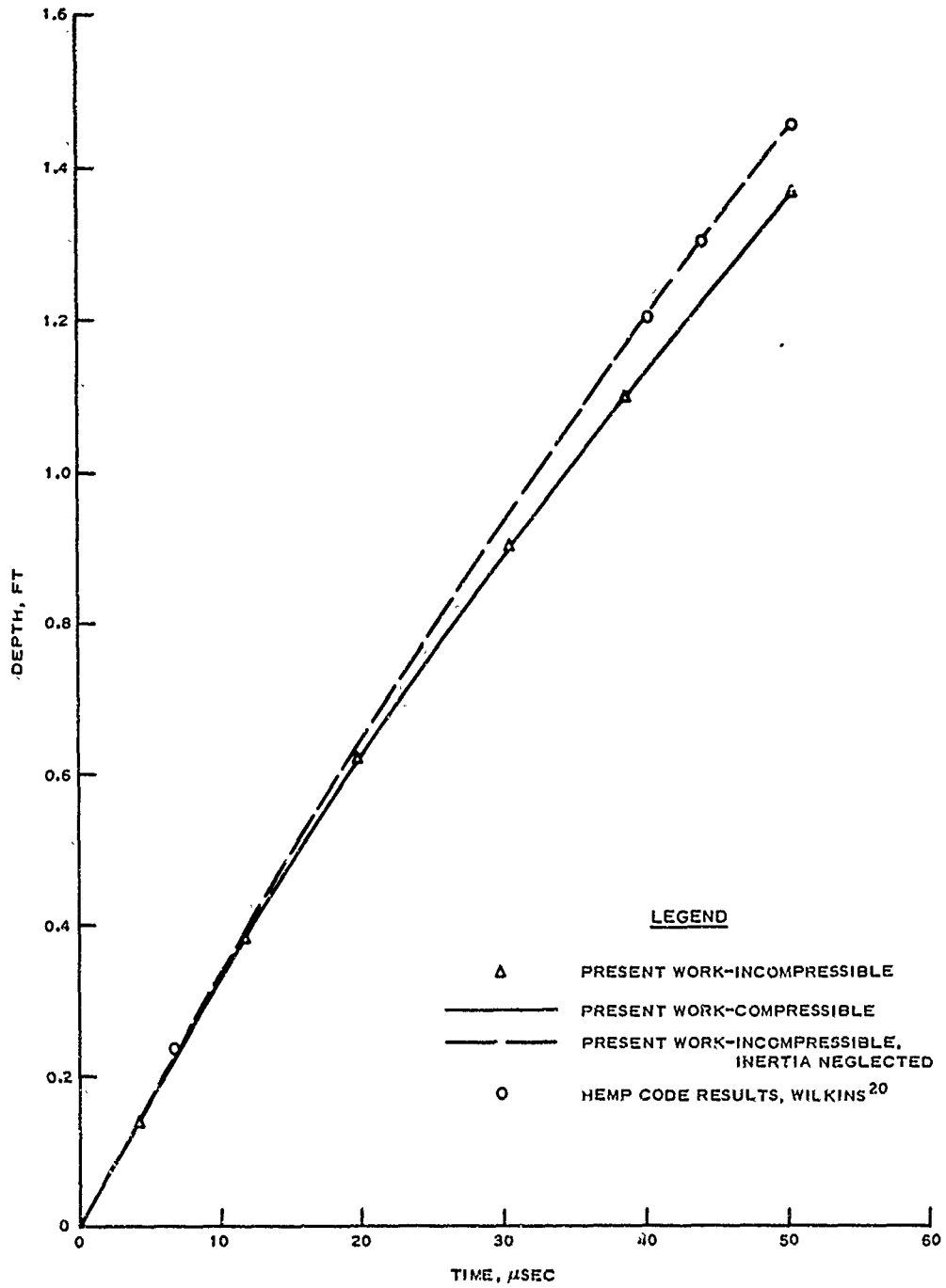


Figure 26. Penetration depth versus time for perforation of 1-in.-thick aluminum slab

represents a very extreme case and yields fair results, the theory probably represents a reasonable extension of the penetration theory for homogeneous targets.

Oblique Impact Against Hard Earth

51. At the present time, no data for oblique impact and ricochet have been found which are appropriate for comparison with the oblique impact theory developed in Part II, i.e., in the experimental results found to date, there is not enough information given about projectiles (e.g., CG location and moment of inertia) to effect a reliable test of the theory. Nevertheless, an application of the theory to the oblique impact of a TDV against a hard earth target is made without experimental verification and is presented as a sample calculation. The projectile characteristics are

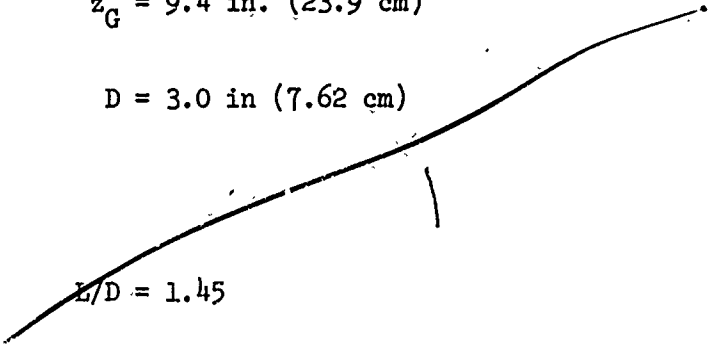
$$W = 15 \text{ lb (6.80 kg)}$$

$$I = 0.0975 \text{ slug-ft}^2 \text{ (0.132 kg-m}^2\text{)}$$

$$z_G = 9.4 \text{ in. (23.9 cm)}$$

$$D = 3.0 \text{ in (7.62 cm)}$$

and


$$L/D = 1.45$$

The target is equivalent to frozen sand found at Camp McCoy, Wisconsin,¹⁹ with

$$\rho = \rho_s = 3.21 \text{ slugs/ft}^3 \text{ (1.66 gm/cm}^3\text{)}$$

$$Y = 958 \text{ psi (66.1 bar)}$$

$$E = 6.25 \times 10^4 \text{ psi (4.31 kbar)}$$

and

$$E_t = 0$$

(These properties have been previously used in the analysis of TDV impact and penetration at Camp McCoy.¹⁹) The initial angle of obliquity is 45 deg (0.76 rad), and the impact velocities considered are 300 fps (91.4 m/sec) and 600 fps (183 m/sec). Initial and final projectile positions are illustrated for each impact velocity in Figures 27 and 28, demonstrating the dependence of vehicle rotation on impact velocity. In the 300-fps case, the projectile undergoes a rotation of 15.1 deg, and the downward motion of the CG is stopped before the nose is fully embedded. In the 600-fps case, the projectile undergoes a rotation of 4.17 deg during the embedding of the nose. The curve connecting the CG locations is the CG trajectory.

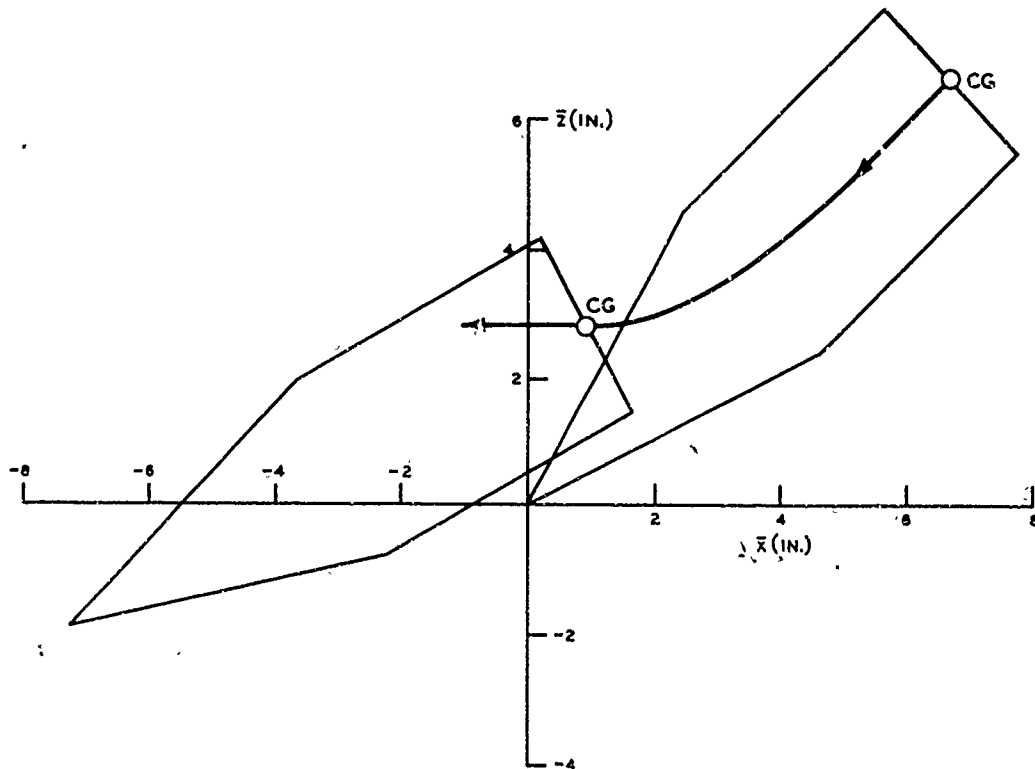


Figure 27. Oblique impact of TDV against hard earth
for $\omega_0 = 45 \text{ deg}$ and $v_0 = 300 \text{ fps}$

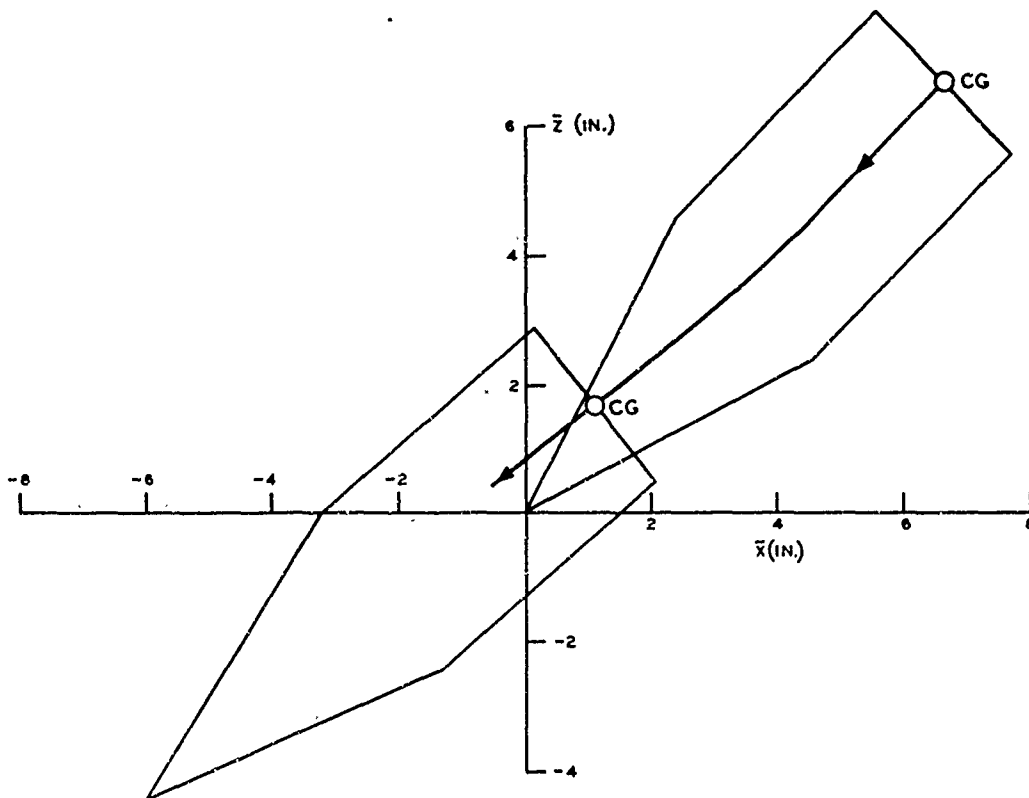


Figure 28. Oblique impact of TDV against hard earth for $\omega_0 = 45$ deg and $v_0 = 600$ fps

PART V: CONCLUSIONS AND RECOMMENDATIONS

52. The results presented in Part IV stand as partial evidence that the cavity expansion theory can be used as an approximate basis for the development of a projectile penetration theory, particularly when the effect of shear is predominant (i.e., for low values of the solid Reynolds number R_s). However, it is emphasized that the analogy between spherical cavity expansion and projectile penetration is somewhat fortuitous, and the present penetration theory probably reflects only the gross features of the projectile-target interaction. Thus, the acquisition of insight into the mechanics of penetration demands the application of whatever means are available, including empirical methods and two-dimensional finite-difference analyses.

53. For estimates of penetration depth, the applicability of the present penetration theory appears to lie in the approximate range $0 < R_s \leq 100$; but the upper bound is offered as a conservative rule of thumb and not as an absolute limit. (Results of experiments at high values of R_s are needed in order to establish a more realistic range.) However, it is important to note that as $R_s \rightarrow 0$ the problem of dynamic penetration reduces to that of a static punch, in which friction may be important. On the other hand, as $R_s \rightarrow \infty$ shear resistance becomes insignificant such that the projectile-target interaction may reduce essentially to a fluid dynamics problem.

54. Although some footholds have been established, the development of the penetration theory is still in an embryonic stage; some suggestions for additional work are listed below:

- a. At the present time, the role of target inertia in the projectile-target interaction is only partially understood, and the degree of contact between the projectile nose and the target has not been established. Consequently, further investigation is necessary to establish the distribution of dynamic pressure on the projectile-target contact surface as a function of projectile velocity, nose shape, and target properties.

- b. Although the cavity expansion shear resistance term p_g seems to represent a reasonable first approximation for average normal stress at the projectile surface due to shear in the target, some effort should be directed toward establishing normal and tangential stress components on the projectile surface due to target shear behavior. Furthermore, the variation of these quantities with nose shape, penetration depth, and confining pressure should be determined.
- c. The present oblique impact theory is limited to the embedding of the projectile nose, with all rotation occurring in a single plane. Moreover, this work has not been verified experimentally. Future efforts should first assess the accuracy of the existing theory. Then, if necessary, the theory can be extended to include aft body effects and motion in three dimensions. Eventually, it may be possible to formulate a workable theory for deep penetration at finite angles of attack and obliquity. However, it is emphasized that overcomplication is as undesirable as oversimplification, and modification of the theory should proceed one step at a time to avoid the incorporation of superfluous details.

REFERENCES

1. Rohani, B., "Fragment and Projectile Penetration Resistance of Soils; High-Velocity Fragment Penetration into Laboratory-Prepared Soil Targets," Miscellaneous Paper S-71-12, Report 2, Jun 1973, U. S. Army Engineer Waterways Experiment Station, CE, Vicksburg, Miss.
2. Young, C. W., "Depth Prediction for Earth-Penetrating Projectiles," Journal, Soil Mechanics and Foundations Division, American Society of Civil Engineers, Vol 95, No. SM3, May 1969, pp 803-817.
3. Classified reference.*
4. Classified reference.
5. Hageman, L. J. and Walsh, J. M., "HELP--A Multi-Material Eulerian Program for Compressible Fluid and Elastic-Plastic Flows in Two Space Dimensions and Time," 3SLR-350, Vol 1, 1970 Systems, Science, and Software, La Jolla, Calif.
6. Sedgwick, R. T., "Theoretical Terminal Ballistic Investigation and Studies of Impact at Low and Very High Velocities," Technical Report AFATL-TR-68-61, 1968, Space Sciences Laboratory, General Electric Company, King of Prussia, Pa.
7. Thigpen, L., "Projectile Penetration of Elastic-Plastic Earth Media," Journal, Geotechnical Engineering Division, American Society of Civil Engineers, Vol 100, No. GT3, Mar 1974, pp 279-294.
8. Bishop, R. F., Hill, R., and Mott, N. F., "The Theory of Indentation and Hardness Tests," Proceedings, Physical Society (London), Vol 57, 1945, pp 147-159.
9. Goodier, J. N., "On the Mechanics of Indentations and Cratering in Solid Targets of Strain-Hardening Metal by Impact of Hard and Soft Spheres," Technical Report 002-64, Jul 1964, Stanford Research Institute, Poulter Research Laboratories, Menlo Park, Calif.
10. _____, "On the Mechanics of Indentation and Cratering in Solid Targets of Strain-Hardening Metal by Impact of Hard and Soft Spheres," Proceedings, Seventh Hypervelocity Impact Symposium, Vol III, Tampa, Fla., Feb 1965, pp 215-260.
11. Ross, B. and Hanagud, S., "Penetration Studies of Ice with Application to Arctic and Subarctic Warfare," Final Report, Project 7000-452, Sep 1969, Stanford Research Institute, Menlo Park, Calif.; prepared under Contract N00014-68-A-0243, NR 274-008 for Submarine Arctic Warfare and Scientific Program, Naval Ordnance Laboratory, Silver Spring, Md., and the Office of Naval Research, Washington, D. C.

* Bibliographical material for the classified references will be furnished to qualified agencies upon request.

12. Hanagud, S. and Ross, B., "Large Deformation, Deep Penetration Theory for a Compressible Strain-Hardening Target Material," AIAA Journal, Vol 9, No. 5, May 1971, pp 905-911.
13. McNeil, R. L., "State of the Art," Proceedings, Conference on Rapid Penetration of Terrestrial Materials, Texas A&M University, College Station, Tex., Feb 1972, pp 11-125.
14. Young, C. W. and Ozanne, G. M., "Compilation of Low Velocity Penetration Data," Research Report No. SC-RR-66-306, Jun 1966, Sandia Laboratories, Albuquerque, N. Mex.
15. Young, C. W., "Low Velocity Penetration Tests in Natural Earth Targets of Selenite and Gypsite," Development Report No. SC-DR-66-2695A, Apr 1967, Sandia Laboratories, Albuquerque, N. Mex.
16. Yih, C. S., Fluid Mechanics, McGraw-Hill, New York, 1969, p 107.
17. Headquarters, Department of the Army, "Protective Design: Fundamentals of Protective Design (Non-Nuclear)," Technical Manual TM 5-855-1, Jul 1965, Washington, D. C.
18. Lin, T. Y., Design of Prestressed Concrete Structures, 2d ed., Wiley, New York, 1963.
19. Rohani, B., "Penetration Performance of Terminal Delivery Vehicle T-98WA into Soft and Frozen Ground: Analyses Based on Both Field Test Results and Theoretical Calculations," Nov 1973, U. S. Army Engineer Waterways Experiment Station, CE, Vicksburg, Miss.
20. Wilkins, M. L., "Penetration Mechanics," Preprint No. UCRL-72111 (prepared for submittal to Yale Scientific Magazine), Nov 1969, Lawrence Radiation Laboratory, University of California, Livermore, Calif., cited with permission of the author.
21. Hildebrand, F. B., Advanced Calculus for Applications, Prentice-Hall, Englewood Cliffs, 1962, pp 53-54.
22. Lamb, H., Hydrodynamics, 6th ed., Dover Publications, New York, 1945, p 122.

APPENDIX A: SPHERICAL CAVITY EXPANSION IN
A CONCENTRICALLY LAYERED MEDIUM

Introduction

1. This appendix presents an extension of cavity expansion theory developed by Bishop, Hill, and Mott,^{8*} Goodier,¹⁰ and Hanagud and Ross.¹² Goodier's treatment dealt with the dynamic expansion of a spherical cavity in an infinite, incompressible, elastic-plastic, strain-hardening medium. By means of a locking approximation in which the plastic zone is assumed to be uniformly compressed, Hanagud and Ross modified the theory to account for the case when the effects of compression predominate over the effects of shear. However, the inertial terms in the Hanagud-Ross treatment do not reduce to those of Goodier for the incompressible case. The present work eliminates this contradiction and also accounts for the effect of concentric layering.

Problem Formulation

2. In Figure A1, a spherical cavity of radius $a(t)$ is surrounded

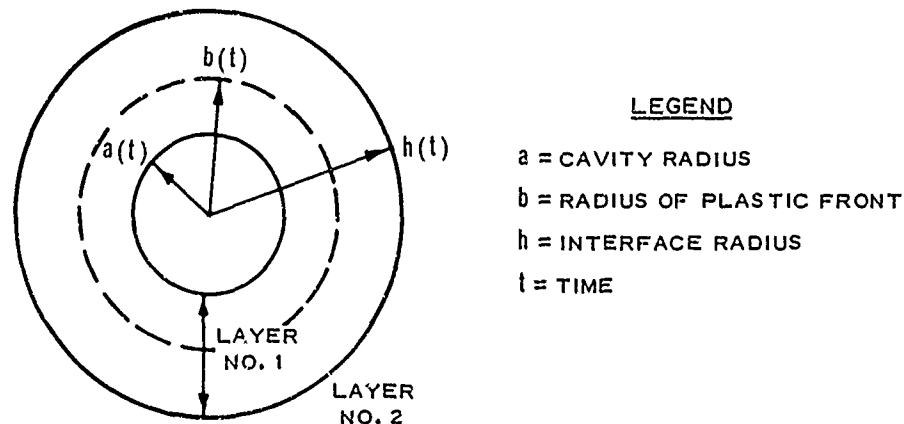


Figure A1. Spherical cavity surrounded by concentric layers

* Raised numbers refer to similarly numbered items in "References" on pp. 65-66 at end of main text.

by two concentric layers of different materials. Both materials are elastic-plastic with linear strain-hardening,⁹⁻¹² as illustrated in Figure A2.

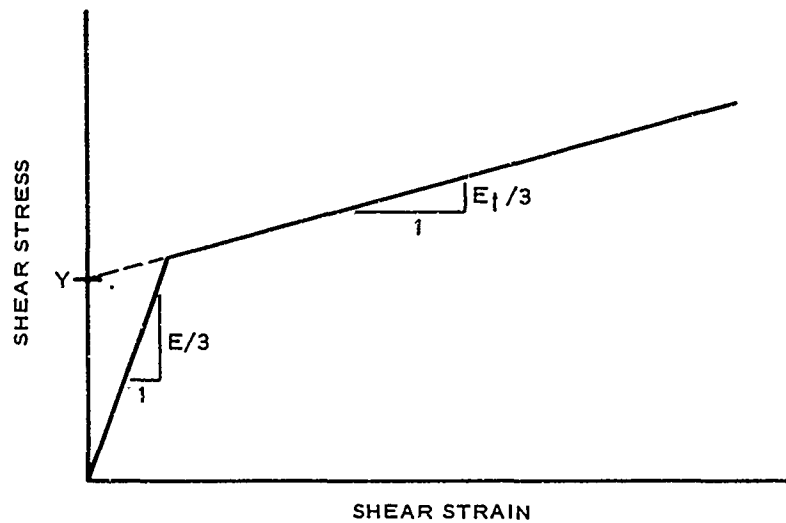


Figure A2. Material behavior in shear

Both materials are incompressible in the elastic and plastic states, but transition from the elastic to the plastic state is accompanied by a finite volumetric strain ϵ_ℓ . This quantity is known as a locking strain^{11,12} and is introduced in order to obtain a first approximation to the effect of compressibility. Although ϵ_ℓ is taken to be constant in the present analysis, it must be a function of pressure to have any physical meaning. However, the variation of ϵ_ℓ with pressure does not alter the analysis or conclusions of this appendix, and a discussion of the locking approximation is given in Appendix B.

3. The elastic and plastic zones are separated by a spherical plastic front of radius $b(t)$ (Figure A1). Since $b(t)$ is the only radial location where compression occurs, it also represents a shock front where density and stress are discontinuous. The equation of motion for spherical symmetry^{11,12} at $r \neq b$ on either side of $b(t)$ is then

$$\frac{\partial \sigma_r}{\partial r} + \frac{2}{r} (\sigma_r - \sigma_\theta) = \rho \left(\frac{\partial}{\partial t} + v \frac{\partial}{\partial r} \right) v \equiv \rho \frac{Dv}{Dt}, \quad b < r < \infty \quad (A1)$$

$$\frac{\partial \sigma_r}{\partial r} + \frac{2}{r} (\sigma_r - \sigma_\theta) = \rho_\ell \left(\frac{\partial}{\partial t} + v_\ell \frac{\partial}{\partial r} \right) v_\ell \equiv \rho_\ell \frac{Dv_\ell}{Dt}, \quad a < r < b \quad (A2)$$

where

σ_r = radial stress

σ_θ = tangential stress

r = radial coordinate

θ = polar coordinate

v = radial velocity in the elastic region

v_ℓ = radial velocity in the locked plastic region

4. The material is required to be stress-free as $r \rightarrow \infty$, and the discontinuity in σ_r at $r = b$ is defined by

$$\Delta \sigma_b \equiv \sigma_b^{(+)} - \sigma_b^{(-)} \quad (A3)$$

where $\sigma_b^{(+)}$ is the limiting value of σ_r as $r \rightarrow b$ in the elastic region, and $\sigma_b^{(-)}$ is the corresponding quantity in the locked plastic region. The equation of motion is then integrated with respect to r from $r = \infty$ to $r = a$, accounting for the discontinuity at $r = b$, so that the compressive normal stress at the cavity surface is given by

$$p(t) \equiv -\sigma_r(a,t) = \Delta \sigma_b + I_m(a,b) + I_m(b,\infty) + I_s(a,\infty) \quad (A4)$$

where the momentum integrals $I_m(a,b)$ and $I_m(b,\infty)$ are given by

$$I_m(a,b) = \int_a^b \rho_\ell \frac{Dv_\ell}{Dt} dr \quad \text{and} \quad I_m(b,\infty) = \int_b^\infty \rho \frac{Dv}{Dt} dr \quad (A5)$$

and the general shear integral is defined by

$$I_s(r_1, r_2) = 2 \int_{r_1}^{r_2} (\sigma_\theta - \sigma_r) \frac{dr}{r} \quad (A6)$$

Inertial Terms

5. Attention is now focused on the terms $\Delta\sigma_b$, $I_m(a, b)$, and $I_m(b, \infty)$ which embody the inertial effects in Equation A4. Consider first the stress discontinuity $\Delta\sigma_b$ at $r = b(t)$. Conservation of mass at $b(t)$ requires that^{11,12}

$$\rho_\ell(\dot{b} - v_\ell) = \rho(\dot{b} - v) \text{ at } r = b \quad (A7)$$

where a dot denotes time derivative. Equation A7 leads to

$$v = \frac{v_\ell - \alpha \dot{b}}{1 - \alpha} \text{ at } r = b \quad (A8)$$

where α is the locking compressibility defined by

$$\alpha \equiv 1 - \frac{\rho}{\rho_\ell} = 1 - e^{\epsilon_\ell} \quad (A9)$$

and

$$\epsilon_\ell \equiv \ln \left(\frac{\rho}{\rho_\ell} \right) \quad (A10)$$

Conservation of momentum at $b(t)$ requires that^{11,12}

$$\Delta\sigma_b = \rho_\ell v_\ell (\dot{b} - v_\ell) - \rho v (\dot{b} - v) \text{ at } r = b \quad (A11)$$

Incorporating Equation A8 in Equation A11 yields

$$\Delta\sigma_b = \frac{\alpha\rho_\ell(\dot{b} - v_\ell)^2}{1 - \alpha} \text{ at } r = b \quad (\text{A12})$$

Conservation of mass in the locked plastic region gives rise to^{11,12}

$$v_\ell(r,t) = \frac{f_\ell(t)}{r^2} \quad (\text{A13})$$

and

$$v_\ell(a,t) = \dot{a} = \frac{f_\ell(t)}{a^2} \text{ at } r = a(t) \quad (\text{A14})$$

Thus,

$$f_\ell = a^2\dot{a} \quad (\text{A15})$$

Likewise, conservation of mass in the elastic region demands that

$$v(r,t) = \frac{f(t)}{r^2} \quad (\text{A16})$$

Substituting Equations A13, A15, and A16 into Equation A9 and evaluating at $r = b(t)$ obtains

$$f(t) = \frac{a^2\dot{a} - \alpha b^2\dot{b}}{1 - \alpha} \quad (\text{A17})$$

Consolidating the definition of D/Dt given in Equations A1 and A2 with Equations A13 and A16 results in

$$\frac{Dv_\ell}{Dt} = \frac{\dot{f}_\ell}{r^2} - \frac{2f_\ell^2}{r^5} \text{ and } \frac{Dv}{Dt} = \frac{\dot{f}}{r^2} - \frac{2f^2}{r^5} \quad (\text{A18})$$

By combining Equation A18 with Equation A5, the momentum integrals become

$$I_m(a,b) = \int_a^b \rho_l \left(\frac{\dot{r}_l}{r^2} - 2 \frac{r_l^2}{r^5} \right) dr \quad (A19)$$

and

$$I_m(b,\infty) = \int_b^{\infty} \rho \left(\frac{\dot{r}}{r^2} - 2 \frac{r^2}{r^5} \right) dr \quad (A20)$$

6. So far, the discussion has avoided explicit consideration of the layer interface $h(t)$. However, the location of $b(t)$ relative to $h(t)$ determines the character of the momentum integrals $I_m(a,b)$ and $I_m(b,\infty)$ as well as the stress discontinuity $\Delta\sigma_b$. Denoting first and second layer properties by the subscripts 1 and 2, respectively, examine the situation when $b < h$ in Figure A3 below.

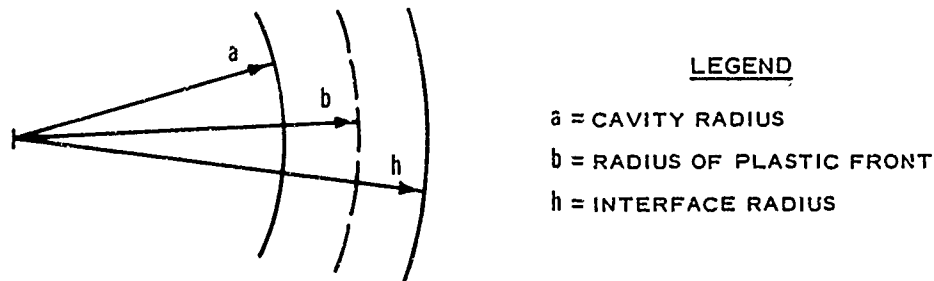


Figure A3. Relative location of cavity surface, plastic front, and layer interface when $b < h$

For this case,

$$I_m(a,b) = \rho_{l_1} \int_a^b \left(\frac{\dot{r}_l}{r^2} - \frac{2r_l^2}{r^5} \right) dr, \quad b < h \quad (A21)$$

and

$$I_m(b, \infty) = \rho_1 \int_b^h \left(\frac{\dot{r}}{r^2} - 2 \frac{r^2}{r^5} \right) dr + \rho_2 \int_h^{\infty} \left(\frac{\dot{r}}{r^2} - 2 \frac{r^2}{r^5} \right) dr, \quad b < h \quad (A22)$$

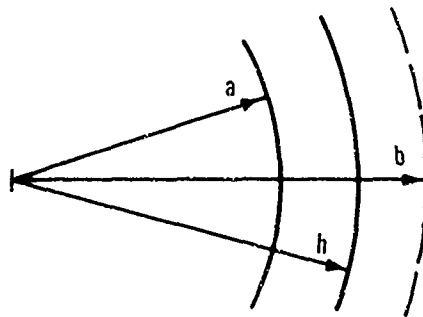
Evaluating integral in Equations A21 and A22 and employing Equation A13 in Equation A12 result in the inertial terms (Equation A4) for $b < h$ as follows:

$$\Delta\sigma_b = \frac{\alpha_1 \rho_{\ell_1}}{1 - \alpha_1} \left(\dot{b} - \frac{r_{\ell}}{b^2} \right)^2, \quad b < h \quad (A23)$$

$$I_m(a, b) = \rho_{\ell_1} \left[\dot{r}_{\ell} \left(\frac{1}{a} - \frac{1}{b} \right) - \frac{1}{2} r_{\ell}^2 \left(\frac{1}{a^4} - \frac{1}{b^4} \right) \right], \quad b < h \quad (A24)$$

$$I_m(b, \infty) = \dot{r} \left[\rho_1 \left(\frac{1}{b} - \frac{1}{h} \right) + \frac{\rho_2}{h} \right] - \frac{1}{2} r^2 \left[\rho_1 \left(\frac{1}{b^4} - \frac{1}{h^4} \right) + \frac{\rho_2}{h^4} \right], \quad b < h \quad (A25)$$

7. In contrast to Figure A3, Figure A4 illustrates the situation when $b > h$.



LEGEND

a = CAVITY RADIUS

h = INTERFACE RADIUS

b = RADIUS OF PLASTIC FRONT

Figure A4. Relative location of cavity surface, layer interface, and plastic front when $b > h$

For this case,

$$I_m(a, b) = \rho_{\ell_1} \int_a^h \left(\frac{\dot{r}_{\ell}}{r^2} - 2 \frac{r^2}{r^5} \right) dr + \rho_{\ell_2} \int_h^b \left(\frac{\dot{r}_{\ell}}{r^2} - 2 \frac{r^2}{r^5} \right) dr, \quad b > h \quad (A26)$$

and

$$I_m(b, \infty) = \rho_2 \int_b^{\infty} \left(\frac{\dot{r}}{r^2} - 2 \frac{r^2}{r^5} \right) dr, \quad b > h \quad (A27)$$

Evaluating the integrals in Equations A26 and A27 and substituting Equation A13 into Equation A12 result in the inertial terms (Equation A4) for $b > h$:

$$\Delta \sigma_b = \frac{\alpha_2 \rho_{\ell_2}}{1 - \alpha_2} \left(\dot{b} - \frac{r_{\ell}}{b^2} \right)^2, \quad b > h \quad (A28)$$

$$I_m(a, b) = \dot{r}_{\ell} \left[\rho_{\ell_1} \left(\frac{1}{a} - \frac{1}{h} \right) + \rho_{\ell_2} \left(\frac{1}{h} - \frac{1}{b} \right) \right] - \frac{1}{2} r_{\ell}^2 \left[\rho_{\ell_1} \left(\frac{1}{a^4} - \frac{1}{h^4} \right) + \rho_{\ell_2} \left(\frac{1}{h^4} - \frac{1}{b^4} \right) \right], \quad b > h \quad (A29)$$

$$I_m(b, \infty) = \rho_2 \left(\frac{\dot{r}}{b} - \frac{r^2}{2b^4} \right), \quad b > h \quad (A30)$$

Shear Terms

8. Consider the term $I_s(a, \infty)$, which constitutes the effect of shear in Equation A4; the appropriate stress-strain relations¹² are expressed as

$$\sigma_{\theta} - \sigma_r = \begin{cases} \frac{2}{3} E (\epsilon_{\theta} - \epsilon_r), & \text{elastic state} \\ Y + \frac{2}{3} E_t (\epsilon_{\theta} - \epsilon_r), & \text{plastic state} \end{cases} \quad (A31)$$

where E and E_t are elastic and strain-hardening moduli, Y is yield strength, and ϵ_r and ϵ_{θ} are radial and tangential strains.

The locking assumption implies that^{11,12}

$$\epsilon_r + 2\epsilon_\theta = \begin{cases} 0, & \text{elastic state} \\ \epsilon_\ell, & \text{plastic state} \end{cases} \quad (\text{A32})$$

The quantities E , E_t , Y , and ϵ_ℓ are material constants. It is appropriate to express the tangential strain as⁹⁻¹²

$$\epsilon_\theta = \ln \frac{r}{r_0} \quad (\text{A33})$$

where r_0 and r are initial and instantaneous particle positions, respectively. Combining Equations A31-A33 yields

$$\sigma_\theta - \sigma_r = \begin{cases} 2E \ln \frac{r}{r_0}, & r > b \\ Y + 2E_t \left(\ln \frac{r}{r_0} - \frac{1}{3} \epsilon_\ell \right), & r < b \end{cases} \quad (\text{A34})$$

where the elastic and locked plastic regions are separated by the plastic front $b(t)$. Note that the shear stress $\sigma_\theta - \sigma_r$ does not have to be continuous for Equation A6 to exist; piecewise continuity is sufficient for existence.²¹ A discontinuity in $\sigma_\theta - \sigma_r$ exists at $r = h$ since this is the material interface where the material properties E , E_t , Y , and ϵ_ℓ are discontinuous. Another discontinuity in $\sigma_\theta - \sigma_r$ exists at the plastic front $r = b(t)$ where the material undergoes a sudden compression. However, when $\epsilon_\ell = 0$ in Equation A34, there is no discontinuity in $\sigma_\theta - \sigma_r$ at $r = b \neq h$. Restricting attention to situations where $|\epsilon_\ell| \ll 3Y/2E_t$ reduces Equation A34 to

$$2(E - E_t) \ln \frac{b}{b_0} \cong Y, \quad |\epsilon_\ell| \ll \frac{3Y}{2E_t} \quad (\text{A35})$$

at $r = b(t)$, where b_0 is the initial position of a particle located at $b(t)$. By rearranging Equation A35, the quantity β is defined by

$$\beta \equiv \ln \frac{b}{b_0} \cong \frac{Y}{2(E - E_t)} \quad (A36)$$

and it follows that

$$b_0 \cong be^{-\beta} \quad (A37)$$

Conservation of mass in the elastic region requires that⁹⁻¹²

$$r^3 - b^3 = r_0^3 - b_0^3, \quad r > b \quad (A38)$$

Substituting Equation A37 into Equation A38 and rearranging results in

$$\ln \frac{r}{r_0} = -\frac{1}{3} \ln \left[1 - \frac{b^3}{r^3} (1 - e^{-3\beta}) \right], \quad r > b \quad (A39)$$

9. In the locked plastic region surrounding a cavity of radius $R(t)$ and initial radius R_0 , conservation of mass demands that^{11,12}

$$\rho(r_0^3 - R_0^3) = \rho_\ell(r^3 - R^3), \quad R < r < b \quad (A40)$$

which gives rise to

$$\ln \frac{r}{r_0} - \frac{1}{3} \epsilon_\ell = -\frac{1}{3} \ln \left(1 - \frac{R_*^3}{r^3} \right), \quad R < r < b \quad (A41)$$

where

$$R_* \equiv R \left(1 - \frac{\rho R_0^3}{\rho_\ell R^3} \right)^{1/3} \quad (A42)$$

and

$$\epsilon_\ell = \ln \frac{\rho}{\rho_\ell} \quad (A43)$$

Incorporating Equation A39 into the first of Equation A34 and integrating with respect to r from $r = r_1$ to $r = r_2$ for constant E obtains

$$2 \int_{r_1}^{r_2} (\sigma_\theta - \sigma_r) \frac{dr}{r} \cong \frac{4}{3} \beta E \left(\frac{b^3}{r_1^3} - \frac{b^3}{r_2^3} \right), \quad b \leq r_1 \leq r_2 < \infty \quad (A44)$$

with the restriction that $\beta \ll 1$. Likewise, employing Equation A41 in the second of Equation A34 and integrating from $r = r_1$ to $r = r_2$ for constant Y and E_t results in

$$2 \int_{r_1}^{r_2} (\sigma_\theta - \sigma_r) \frac{dr}{r} = 2Y \ln \frac{r_2}{r_1} + \frac{4}{9} E_t \sum_{m=1}^{\infty} \frac{1}{m^2} \left[\left(\frac{R_*}{r_1} \right)^{3m} - \left(\frac{R_*}{r_2} \right)^{3m} \right],$$

$$R \leq r_1 \leq r_2 \leq b \quad (A45)$$

(Note: Equations A44 and A45 are evaluated in Reference 11.) Equations A42, A44, and A45 now make evaluation of Equation A6 straightforward. With $a(t)$ and $h(t)$ representing cavities relative to the first and second layers, respectively, R_* , R , and R_0 are replaced in the same order in Equation A42 by a_* , a , and a_0 and then by h_* , h , and h_0 so that

$$a_* = a \left(1 - \frac{\rho_1 a_0^3}{\rho_{l_1} a^3} \right)^{1/3} \quad \text{and} \quad h_* = h \left(1 - \frac{\rho_2 h_0^3}{\rho_{l_2} h^3} \right)^{1/3} \quad (A46)$$

where the subscripts 1 and 2 denote first and second layer properties.

10. Examining first the case where $b(t) < h(t)$ in Figure A3 makes it possible to rewrite the shear term in Equation A4 as

$$I_s(a, \infty) = I_s(a, b) + I_s(b, h) + I_s(h, \infty), \quad b < h \quad (A47)$$

Applying Equations A44 and A45 to Equation A47 then produces

$$I_s(a, \infty) = 2Y_1 \ln \frac{b}{a} + \frac{4}{9} E_{t_1} \sum_{m=1}^{\infty} \frac{1}{m^2} \left[\left(\frac{a_*}{a} \right)^{3m} - \left(\frac{a_*}{b} \right)^{3m} \right] \\ + \frac{4}{3} \beta_1 E_1 \left(1 - \frac{b^3}{h^3} \right) + \frac{4}{3} \beta_1 E_2 \frac{b^3}{h^3}, \quad b < h \quad (A48)$$

For the case where $b(t) > h(t)$ in Figure A4, Equation A47 is replaced by

$$I_s(a, \infty) = I_s(a, h) + I_s(h, b) + I_s(b, \infty), \quad b > h \quad (A49)$$

By means of Equations A44 and A45, Equation A49 is superseded by

$$I_s(a, \infty) = 2Y_1 \ln \frac{h}{a} + \frac{4}{9} E_{t_1} \sum_{m=1}^{\infty} \frac{1}{m^2} \left[\left(\frac{a_*}{a} \right)^{3m} - \left(\frac{a_*}{h} \right)^{3m} \right] \\ + 2Y_2 \ln \frac{b}{h} + \frac{4}{9} E_{t_2} \sum_{m=1}^{\infty} \frac{1}{m^2} \left[\left(\frac{h_*}{h} \right)^{3m} - \left(\frac{h_*}{b} \right)^{3m} \right] \\ + \frac{4}{3} \beta_2 E_2, \quad b > h \quad (A50)$$

Relations Among $a(t)$, $b(t)$, and $h(t)$

11. First, examine Equations A38 and A40 for the case $b(t) < h(t)$. Replacing r and r_0 by h and h_0 in Equation A38 and combining with Equation A37 yields

$$h^3 - h_0^3 = \left(1 - e^{-3\beta_1} \right) b^3, \quad b < h \quad (A51)$$

Likewise, replacing r , r_0 , R , and R_0 by b , b_0 , a , and a_0 ,

respectively, in Equation A40 and combining with Equation A37 results in the expression

$$a_*^3 = \delta_1 b^3, \quad b < h \quad (\text{A52})$$

where

$$\delta_1 = 1 - \frac{\rho_1}{\rho_{l_1}} e^{-3\beta_1} \quad (\text{A53})$$

and a_* is given by the first of Equation A46. Evaluating Equation A51 at $b = h$ obtains

$$h = h_0 e^{\beta_1} \quad @ \quad b = h \quad (\text{A54})$$

Now since $\beta_1 \ll 1$, it is appropriate to make the approximation

$$h \cong h_0, \quad b \leq h_0 \quad (\text{A55})$$

By restricting attention to cavities which expand to more than twice the initial radius a_0 , it is acceptable to replace the first of Equation A46 by

$$a_* \cong a \quad (\text{A56})$$

so that Equation A52 reduces to

$$a^3 \cong \delta_1 b^3, \quad b < h_0 \quad (\text{A57})$$

and

$$a^2 \dot{a} = \delta_1 b^2 \dot{b}, \quad b < h_0 \quad (\text{A58})$$

12. When $b(t) > h(t)$, r , r_0 , R , and R_0 are replaced respectively in Equation A40 by b , b_0 , h , and h_0 . Consolidating

the resulting equation with Equation A37 obtains

$$h_*^3 = \delta_2 b^3, \quad b > h_0 \quad (A59)$$

and

$$h_*^2 h_* = \delta_2 b^2 b, \quad b > h_0 \quad (A60)$$

where

$$\delta_2 = 1 - \frac{\rho_2}{\rho_{\ell_2}} e^{-3\beta_2} \quad (A61)$$

Now Equation A40 with r , r_0 , R , and R_0 replaced respectively by h , h_0 , a , and a_0 becomes

$$\rho_1 (h_0^3 - a_0^3) = \rho_{\ell_1} (h^3 - a^3), \quad b > h_0 \quad (A62)$$

By rearranging and combining with Equations A46 and A56, Equation A62 reduces to

$$h^3 = a_*^3 + \frac{\rho_1}{\rho_{\ell_1}} h_0^3 \cong a^3 + \frac{\rho_1}{\rho_{\ell_1}} h_0^3 \quad (A63)$$

and

$$h^2 h = h_*^2 h_* = \delta_2 b^2 b = a^2 a, \quad b > h_0 \quad (A64)$$

Combined Effects

13. Inserting Equations A58 and A64 into Equation A17 produces

$$f(t) = \begin{cases} C_1 a^2 \dot{a}, & b < h_0 \\ C_2 a^2 \dot{a}, & b > h_0 \end{cases} \quad (A65)$$

where

$$C_1 = \frac{1 - \frac{\alpha_1}{\delta_1}}{1 - \alpha_1} \quad \text{and} \quad C_2 = \frac{1 - \frac{\alpha_2}{\delta_2}}{1 - \alpha_2} \quad (\text{A66})$$

Using Equations A15, A58, and A65 in Equations A23-A25 results in

$$\Delta\sigma_b = \frac{\alpha_1 \rho_{t_1} (1 - \delta_1)^2}{\delta_1^2 (1 - \alpha_1)} \left(\frac{4}{b} \right) \dot{a}^2, \quad b < h_0 \quad (\text{A67})$$

$$I_m(a, b) = \rho_{t_1} \left[(a\dot{a} + 2\dot{a}^2) \left(1 - \frac{a}{b} \right) - \frac{1}{2} \dot{a}^2 \left(1 - \frac{a^4}{b^4} \right) \right], \quad b < h_0 \quad (\text{A68})$$

$$I_m(b, \infty) = C_1 (a\dot{a} + 2\dot{a}^2) \left[\rho_1 \left(\frac{a}{b} - \frac{a}{h} \right) + \rho_2 \frac{a}{h} \right] - \frac{1}{2} C_1^2 \dot{a}^2 \\ \times \left[\rho_1 \left(\frac{4}{b} - \frac{4}{h} \right) + \rho_2 \frac{4}{h} \right], \quad b < h_0 \quad (\text{A69})$$

By means of Equation A56, Equation A48 reduces to

$$I_s(a, \infty) = 2Y_1 \ln \frac{b}{a} + \frac{4}{9} E_{t_1} \left[\frac{\pi^2}{6} - \sum_{m=1}^{\infty} \frac{1}{m^2} \left(\frac{a}{b} \right)^{3m} \right] \\ + \frac{4}{3} \beta_1 E_1 \left(1 - \frac{b^3}{h^3} \right) + \frac{4}{3} \beta_1 E_2 \frac{b^3}{h^3}, \quad b < h_0 \quad (\text{A70})$$

where¹¹

$$\sum_{m=1}^{\infty} \frac{1}{m^2} = \frac{\pi^2}{6} \quad (\text{A71})$$

Incorporating Equations A15, A64, and A65 in Equations A28-A30 yields

$$\Delta\alpha_b = \frac{\alpha_2 \rho_{\ell_2} (1 - \delta_2)^2}{\delta_2^2 (1 - \alpha_2)} \left(\frac{a^4}{b^4} \right) \dot{a}^2, \quad b > h_0 \quad (\text{A72})$$

$$I_m(a, b) = (a\ddot{a} + 2\dot{a}^2) \left[\rho_{\ell_1} \left(1 - \frac{a}{h} \right) + \rho_{\ell_2} \left(\frac{a}{h} - \frac{a}{b} \right) \right] \\ - \frac{1}{2} \dot{a}^2 \left[\rho_{\ell_1} \left(1 - \frac{a^4}{h^4} \right) + \rho_{\ell_2} \left(\frac{a^4}{h^4} - \frac{a^4}{b^4} \right) \right], \quad b > h_0 \quad (\text{A73})$$

$$I_m(b, \infty) = \rho_2 \left[C_2 (a\ddot{a} + 2\dot{a}^2) \frac{a}{b} - \frac{1}{2} C_2 \dot{a}^2 \left(\frac{a^4}{b^4} \right) \right], \quad b > h_0 \quad (\text{A74})$$

By utilizing Equations A56 and A59, Equation A50 becomes

$$I_s(a, \infty) = 2Y_1 \ln \frac{h}{a} + \frac{4}{9} E_{t_1} \left[\frac{\pi^2}{6} - \sum_{m=1}^{\infty} \frac{1}{m^2} \left(\frac{a}{h} \right)^{3m} \right] + 2Y_2 \ln \frac{b}{h} \\ + \frac{4}{9} E_{t_2} \sum_{m=1}^{\infty} \frac{\delta_2^m}{m^2} \left[\left(\frac{b}{h} \right)^{3m} - 1 \right] + \frac{4}{3} \beta_2 E_2, \quad b > h_0 \quad (\text{A75})$$

Summary of Results

14. For consistency with previous work,⁹⁻¹² the compressive normal stress $p(t)$ at the cavity surface is expressed as

$$p(t) = p_s + \rho_{\ell_1} (B_1 a\ddot{a} + B_2 \dot{a}^2) \quad (\text{A76})$$

where

$$p_s \equiv I_s(a, \infty) \quad (A77)$$

and

$$\rho_{\ell_1} (B_1 a \ddot{a} + B_2 \ddot{a}^2) = \Delta \bar{\sigma}_b + I_m(a, b) + I_m(b, \infty) \quad (A78)$$

For the case where $b < h_0$, p_s , B_1 , and B_2 are given by

$$p_s = 2Y_1 \ln \frac{b}{a} + \frac{4}{9} E_{t_1} \left[\frac{\pi^2}{6} - \sum_{m=1}^{\infty} \frac{1}{m^2} \left(\frac{a}{b} \right)^{3m} \right] + \frac{4}{3} \beta_1 E_1 \left(1 - \frac{b^3}{h_0^3} \right) + \frac{4}{3} \beta_1 E_2 \frac{b^3}{h_0^3}, \quad b < h_0 \quad (A79)$$

$$B_1 = 1 - \frac{a}{b} + \left(1 - \frac{\alpha_1}{\delta_1} \right) \left[\frac{a}{b} - \left(1 - \frac{\rho_2}{\rho_1} \right) \frac{a}{h_0} \right], \quad b < h_0 \quad (A80)$$

$$B_2 = 2B_1 + \frac{\alpha_1 (1 - \delta_1)^2}{\delta_1^2 (1 - \alpha_1)} \left(\frac{a^4}{b^4} \right) - \frac{1}{2} \left(1 - \frac{a^4}{b^4} \right) - \frac{\left(1 - \frac{\alpha_1}{\delta_1} \right)^2}{2(1 - \alpha_1)} \left[\frac{a^4}{b^4} - \left(1 - \frac{\rho_2}{\rho_1} \right) \frac{a^4}{h_0^4} \right], \quad b < h_0 \quad (A81)$$

where $h \cong h_0$ and $a/b \cong \delta_1^{1/3}$ from Equation A57. For the case where $b > h_0$, p_s , B_1 , and B_2 are expressed as

$$p_s = 2Y_1 \ln \frac{h}{a} + \frac{4}{9} E_{t_1} \left[\frac{\pi^2}{6} - \sum_{m=1}^{\infty} \frac{1}{m^2} \left(\frac{a}{h} \right)^{3m} \right] + 2Y_2 \ln \frac{b}{h} + \frac{4}{9} E_{t_2} \sum_{m=1}^{\infty} \frac{\delta_2^m}{m^2} \left[\left(\frac{b}{h} \right)^{3m} - 1 \right] + \frac{4}{3} \beta_2 E_2, \quad b > h_0 \quad (A82)$$

$$B_1 = 1 - \frac{a}{h} + \frac{\rho_{l_2}}{\rho_{l_1}} \left(\frac{a}{h} - \frac{a}{b} \right) + \frac{\rho_2}{\rho_{l_1}} \left(\frac{1 - \frac{\alpha_2}{\delta_2}}{1 - \alpha_2} \right) \frac{a}{b}, \quad b > h_0 \quad (A83)$$

$$B_2 = 2B_1 + \frac{\rho_{l_2} \alpha_2 (1 - \delta_2)^2}{\rho_{l_1} \delta_2^2 (1 - \alpha_2)} \left(\frac{a}{b} \right)^4 - \frac{1}{2} \\ \times \left[1 - \frac{a}{h} + \frac{\rho_{l_2}}{\rho_{l_1}} \left(\frac{a}{h} - \frac{a}{b} \right) \right] - \frac{\rho_2}{2\rho_{l_1}} \left(\frac{1 - \frac{\alpha_2}{\delta_2}}{1 - \alpha_2} \right)^2, \quad b > h_0 \quad (A84)$$

where

$$h^3 \cong a^3 + \frac{\rho_1}{\rho_{l_1}} h_0^3 \quad (A85)$$

from Equation A63, and b is given by Equation A59. Note that at $b = h \cong h_0$, $p(t)$ may be discontinuous. This arises from the mathematical treatment of the problem and does not necessarily correspond to a physical discontinuity. What happens is that at $b = h$, the speed at which the plastic front is propagated undergoes a step change due to the discontinuity in Y and E . This is an elastic effect and can occur even if the materials are incompressible.

Special Cases

15. When both layers have exactly the same properties (i.e. the homogeneous case), then by dropping the subscript, Equation A57 becomes

$$\frac{a}{b} \cong \delta^{1/3} \quad (A86)$$

so that Equations A79-A84 reduce to

$$p_s = -\frac{2}{3} Y \ln \delta + \frac{4}{9} E_t \left[\frac{\pi^2}{6} - \sum_{m=1}^{\infty} \frac{\delta^m}{m^2} \right] + \frac{4}{3} \beta E \quad (A87)$$

$$B_1 = 1 - \frac{\alpha}{\delta^{2/3}} \quad (\text{A88})$$

$$B_2 = \frac{3}{2} - \frac{\alpha}{\delta^{2/3}} \left[2 - \frac{(1-\delta)^2}{1-\alpha} \right] + \frac{1}{2} \delta^{4/3} \left[1 - \frac{(1-\frac{\alpha}{\delta})^2}{1-\alpha} \right] \quad (\text{A89})$$

where

$$\delta = 1 - \frac{\rho}{\rho_\ell} e^{-3\beta} \quad (\text{A90})$$

$$\beta = \frac{Y}{2(E - E_t)} \quad (\text{A91})$$

$$\epsilon_\ell = \ln \frac{\rho}{\rho_\ell} \quad (\text{A92})$$

and

$$\alpha = 1 - \frac{\rho}{\rho_\ell} \quad (\text{A93})$$

15. When $\alpha = 0$, the material is incompressible, and Equations A67 and A68 reduce to

$$B_1 = 1 \quad (\text{A94})$$

$$B_2 = \frac{3}{2} \quad (\text{A95})$$

Since it is usually true that⁹⁻¹² $Y \ll E$ and $E_t \ll E$, then

$$p_s \cong \frac{2}{3} Y \left(1 + \ln \frac{2E}{3Y} \right) + \frac{2}{27} \pi^2 E_t \quad (\text{A96})$$

in agreement with Goodier.¹⁰ On the other hand, when compressibility predominates over shear, $\beta \ll \alpha$, and

$$\delta \cong \alpha \quad (\text{A97})$$

$$B_1 \cong 1 - \delta^{1/3} \quad (\text{A98})$$

and

$$B_2 \cong \frac{3}{2} - \delta^{1/3}(1 + \delta) + \frac{1}{2} \delta^{4/3} \quad (\text{A99})$$

in agreement with Hanagud and Ross.¹²

APPENDIX B: COMPRESSIBILITY

Introduction

1. The cavity expansion theory developed in Appendix A and the penetration theory developed in Part II both utilize the concept of locking behavior^{11,12} to estimate the effect of material compressibility at any given instant. Moreover, within the context of the cavity expansion theory and the present penetration theory, the incorporation of compressibility constitutes a perturbation of the basic incompressible theories set forth by Goodier.^{9,10} In this appendix a technique for approximating the effective locking strain ϵ_ℓ is developed in which the material is first treated as incompressible in order to obtain an approximate value for the average dynamic pressure in the plastic zone. This pressure can then be used to estimate the average volumetric strain (i.e., the effective locking strain ϵ_ℓ) in the plastic zone when the material is only slightly compressible.

Average Dynamic Pressure in the Plastic Zone

2. Suppose there is a spherical cavity centered at the origin with radius $a(t)$, radial velocity \dot{a} , and radial acceleration \ddot{a} . Furthermore, suppose that the cavity is surrounded by an incompressible homogeneous material whose behavior in shear is rate independent. The situation is spherically symmetric, and the dynamic pressure P at any $r > a$ in the material is²²

$$P = \rho \left[\frac{a}{r} (a\ddot{a} + 2\dot{a}^2) - \frac{a^4 \dot{a}^2}{2r^4} \right] \quad (B1)$$

where r is the radial coordinate, ρ is density, and the material is stress-free as $r \rightarrow \infty$. The average value of P in a region $a < r < b$ is

$$P_{ave} = \frac{\int_a^b Pr^2 dr}{\int_a^b r^2 dr} \quad (B2)$$

Employing Equation B1 in Equation B2 and evaluating the integrals results in the expression

$$P_{ave} = \frac{3}{2} \rho \left[\frac{(a\delta + 2a^2) \left(\frac{a}{b} - \frac{a^3}{b^3} \right) - a^2 \left(\frac{a^3}{b^3} - \frac{a^4}{b^4} \right)}{\left(1 - \frac{a^3}{b^3} \right)} \right] \quad (B3)$$

Suppose now that b represents the radius of the plastic front for an incompressible elastic-plastic material as described in Appendix A (where $\rho = \rho_\ell$) such that Equations A86 and A90 reduce to

$$\frac{a}{b} \cong \delta_I^{1/3} \quad (B4)$$

and

$$\delta_I = 1 - e^{-3\beta} \quad (B5)$$

Equation B4 is now incorporated in Equation B3 so the average dynamic pressure in the plastic zone $a < r < b$ for an incompressible material is

$$P_{ave} = \frac{3}{2} \rho \left[\frac{(a\delta + 2a^2) \left(\delta_I^{1/3} - \delta_I \right) - a^2 \left(\delta_I - \delta_I^{4/3} \right)}{1 - \delta_I} \right] \quad (B6)$$

Equation B6 can now be used in conjunction with a pressure-density curve to obtain a first approximation to the average volumetric strain (i.e. locking strain) ϵ_ℓ in the plastic zone $a < r < b$ as long as $|\epsilon_\ell| \ll 1$. Thus, for materials which are only slightly compressible, Equation B6 can be used to obtain a value for ϵ_ℓ which is appropriate

for the cavity expansion theory in Appendix A. For a two-layer situation, Equation B6 is used in turn for each layer. This may lead to an underestimation of $|\epsilon_\ell|$ for the first layer and an overestimation for the second layer, but a reasonable approximation to the average effect of compressibility for both layers is obtained.

Compressibility in the Penetration Theory

3. An upper limit on P_{ave} for projectile penetration is obtained by replacing \dot{a} with the projectile velocity \dot{q} and dropping the material acceleration term $a\ddot{a}$ (Appendix C) in Equation B6 such that

$$P_{ave} = \frac{3}{2} \rho \dot{q}^2 \left(\frac{2\delta_I^{1/3} - 3\delta_I + \delta_I^{4/3}}{1 - \delta_I} \right) \quad (B7)$$

Equation B7 can be used with a pressure-density curve for a given target material to obtain an upper limit on $|\epsilon_\ell|$ at any velocity \dot{q} as long as $|\epsilon_\ell| \ll 1$. Subject to this limitation,

$$\alpha = 1 - \frac{\rho}{\rho_\ell} \cong -\epsilon_\ell \quad (B8)$$

APPENDIX C: TARGET ACCELERATION

Introduction

1. In Goodier's original penetration theory for rigid spherical projectiles,^{9,10} the projectile equation of motion is

$$\left(M + \frac{2}{3} \pi a_o^3 \rho_{\ell} B_1\right) \ddot{q} = -\pi a_o^2 \left(p_s + \frac{2}{3} \rho_{\ell} B_2 \dot{q}^2\right) \quad (C1)$$

The development of this equation is discussed in Part II, paragraph 9. The term $(2/3)\pi a_o^3 \rho_{\ell} B_1$ reflects Goodier's assumed variation of target acceleration over the frontal surface of the projectile, and the quantity $(2/3)\pi a_o^3 \rho_{\ell}$ is generally known as the added mass for the sphere.¹³ When $R_a \ll 1$ (Part II, Equation 5), this term has only a small effect on penetration depth predictions; but when the added mass is comparable to projectile mass M (e.g., $R_a \gtrsim 0.1$), then the effect of this term becomes significant.

The Effect of Added Mass on Penetration Predictions

2. Consider the projectile equation of motion (C1) which without the term $(2/3)\pi a_o^3 \rho_{\ell} B_1$ reduces to

$$M \ddot{q} = -\pi a_o^2 \left(p_s + \frac{2}{3} \rho_{\ell} B_2 \dot{q}^2\right) \quad (C2)$$

where deletion of the added mass is tantamount to disregarding target acceleration. Equation C2 is now used in Goodier's original applications of his rigid projectile penetration theory. The results are shown in Figures C1-C4; the solid curves correspond to Equation C1, and the dashed curves correspond to Equation C2. In these figures q_p is final penetration depth, D is projectile diameter, v_o is impact velocity, ρ_p is projectile density, and Y is target yield strength. In each case discarding the added mass term improves agreement with experiment. From these results it is concluded that the contribution of the term $\pi a_o^3 \rho_{\ell} B_1$

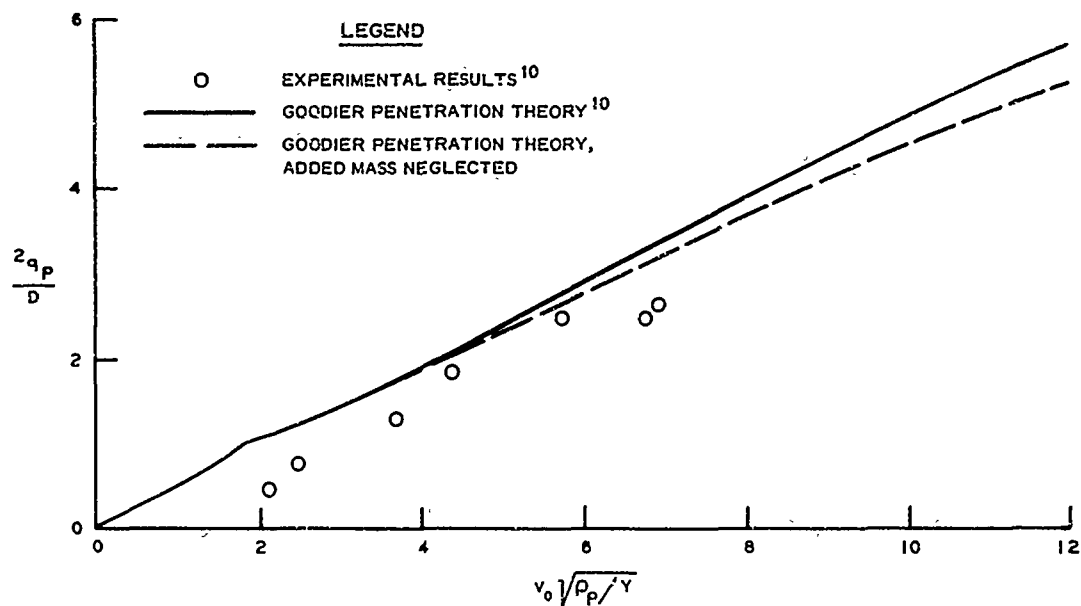


Figure C1. Penetration of aluminum target (AL 2024 T3) by lead spheres, $R_a = 0.16$

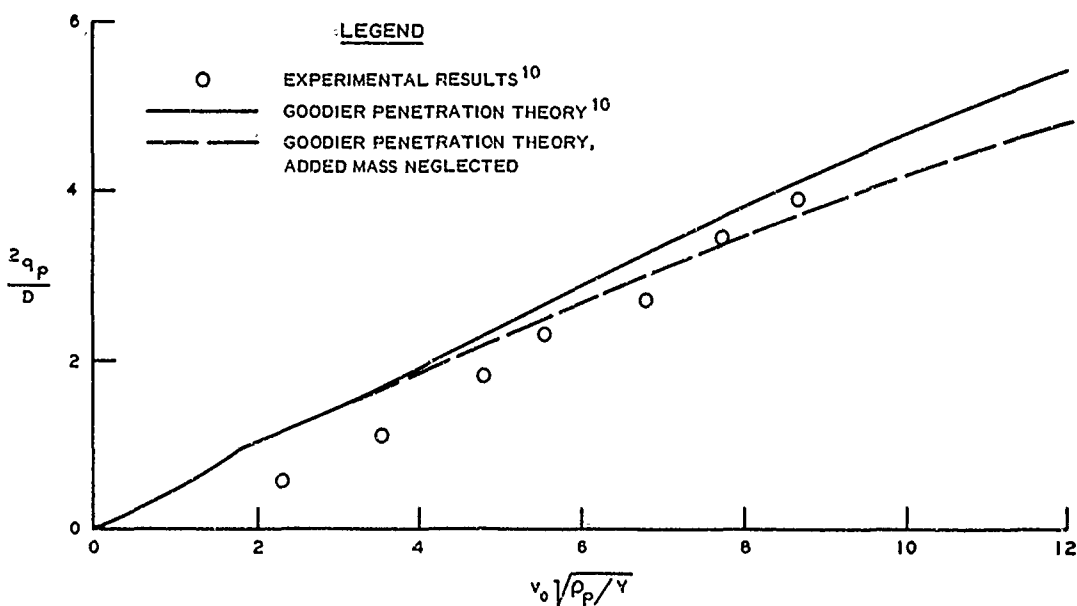


Figure C2. Penetration of aluminum target (AL 2024 T3) by copper spheres, $R_a = 0.22$

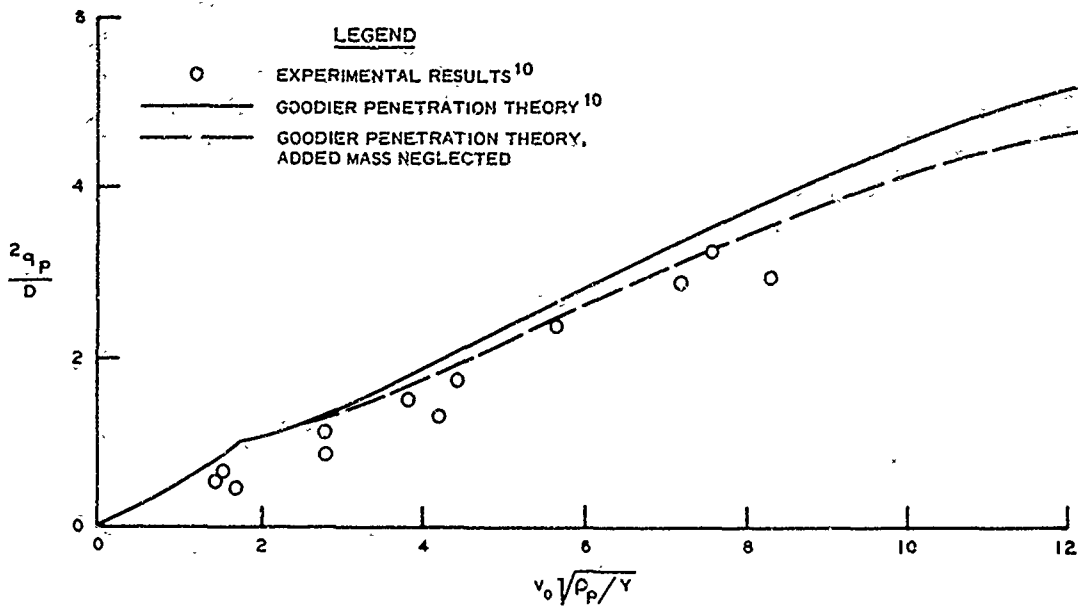


Figure C3. Penetration of aluminum target (AL 2024 T3) by steel spheres, $R_a = 0.25$

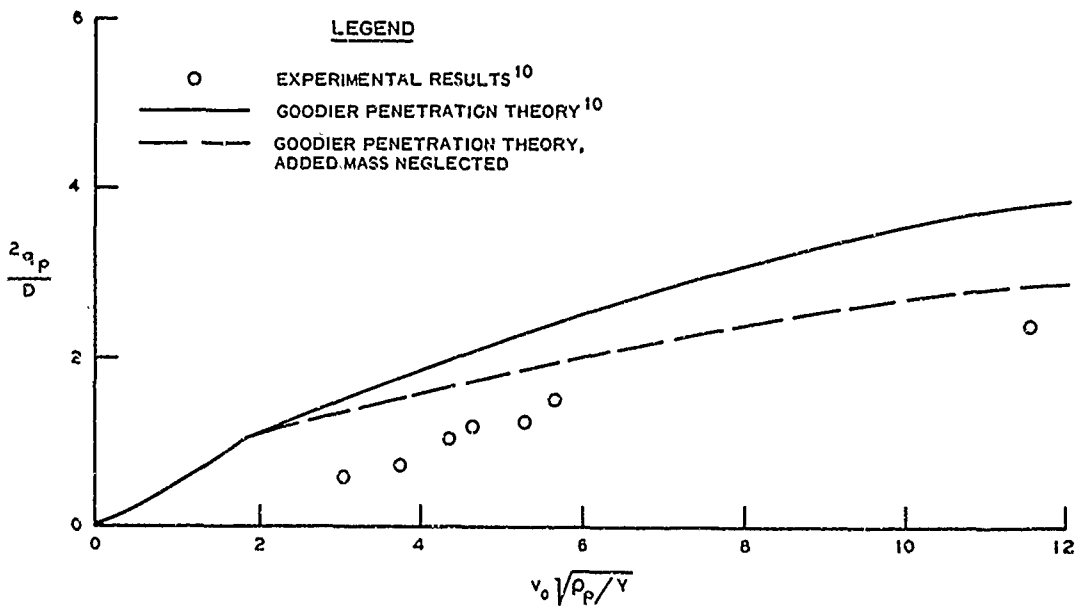


Figure C4. Penetration of aluminum target (AL 2024 T3) by aluminum spheres, $R_a = 0.75$

which appears in Part II, Equation 30 and elsewhere, probably represents a high upper limit insofar as the effect of target acceleration on final depth of penetration is concerned. Furthermore, for most applications of the penetration theory as formulated, it appears appropriate simply to drop the B_1 term from Equation 30. However, this term is retained as an upper limit for added mass throughout the presentation of theory in Part II.

APPENDIX D: NOTATION

a, \dot{a}, \ddot{a}	Radial position, velocity, and acceleration of spherical cavity wall, respectively
a_H	Projectile radius at point of contact with a layer interface
a_n	Projectile radius at point of contact with the target surface
a_o	Projectile radius at base of nose
A	Projectile frontal area = πa_o^2
b, h	Radii of spherical plastic front and concentric layer interface, respectively
B_1, B_2	Inertial coefficients from cavity expansion theory
C_o	Initial sound speed
CG	Center of gravity
CRH	Ogive caliber radius head
D	Projectile diameter at base of nose = $2a_o$
E	Modulus of elasticity
E_t	Strain-hardening modulus
f_n	Factor relating projectile nose shape to target inertial resistance
F_x	Resisting force projected normal to projectile axis of symmetry
F_z	Resisting force projected along projectile axis of symmetry
G_o	Ratio of maximum inertial resistance to shear resistance within the context of penetration theory-- $(\rho_t B_2 \dot{q}^2 / p_s)$
H	Layer interface location
H_o	Initial layer interface location
I	Projectile moment of inertia
I_m	Momentum integral
I_s	General shear integral
L	Nose length
M	Projectile mass
M_{CG}	Moment about CG
p	Compressive normal stress on projectile surface
p_n	Average value of p over the projectile nose surface
p_s	Component of p due to target deformation (shear resistance)
p_I	Component of p due to target inertia (dynamic pressure)

P_{ave}	Average dynamic pressure in the plastic zone
q, \dot{q}, \ddot{q}	Projectile penetration depth, velocity, and acceleration, respectively
q_p	Final depth of penetration
q_{pb}	Final penetration depth for a blunt cylinder
q_*	Projectile penetration depth when the plastic front reaches a layer interface
R_a	$\pi a^3 \rho_\ell / M$, added mass parameter
R_n	Nose performance ratio
R_s	$\rho q^2 / Y$, order of magnitude index of the ratio of inertia forces to shear forces, referred to as the "solid Reynolds number"
S	Location of plastic front
t	Time
v	Radial velocity in the elastic region
v_ℓ	Radial velocity in the plastic region
v_n	Normal component of particle velocity
v_o	Impact velocity
v_p	Target particle velocity
v_t	Tangential component of particle velocity
W	Projectile weight
$\bar{X}, \bar{Y}, \bar{Z}$	Fixed space coordinates
Y	Yield strength
z	Distance from projectile nose tip along axis of symmetry
z_G	Distance from projectile nose tip to CG
z_o	Point where the projectile axis of symmetry intersects the target surface
α	Target compressibility = $1 - \rho / \rho_\ell$
β	$Y/2 / (E - E_t)$
$\bar{\gamma}$	Moment arm
δ	$1 - (\rho / \rho_\ell) \exp(-3\beta)$
ϵ_ℓ	Locking strain = $\ln(\rho / \rho_\ell)$
ϵ_r	Radial strain
ϵ_θ	Tangential strain
ζ	L/D
θ	Polar coordinate or polar angle

λ	See Equation 78
ξ	z/z_0
π	3.1416
ρ	Initial target density
ρ_l	Locked target density, i.e., average compressed density in the plastic zone
$\sigma_b^{(+)}$	Limiting value of σ_r as $r \rightarrow b$ in the elastic region
$\sigma_b^{(-)}$	Limiting value of σ_r as $r \rightarrow b$ in the locked plastic region
σ_r	Radial stress
σ_θ	Circumferential stress
ϕ	Cone half-angle
ψ	Circumscribed cone half-angle
$\omega, \dot{\omega}, \ddot{\omega}$	Angle of obliquity, rotational velocity, and angular acceleration, respectively
ω_0	Initial angle of obliquity

Note: A dot over any quantity denotes a derivative with respect to time.

In accordance with ER 70-2-3, paragraph 6c(1)(b), dated 15 February 1973, a facsimile catalog card in Library of Congress format is reproduced below.

Bernard, Robert S

Development of a projectile penetration theory; Report 1: Penetration theory for shallow to moderate depths, by Robert S. Bernard and; Sathya V. Hanagud. Vicksburg, U. S. Army Engineer Waterways Experiment Station, 1975.

I v. (various pagings) illus. 27 cm. (U. S. Waterways Experiment Station. Technical report S-75-9, Report 1)

Prepared for Office, Chief of Engineers, U. S. Army, Washington, D. C., under Project 4A161102B52E, Task 04, Work Unit 013.

Includes bibliography.

1. Projectile penetration. I. Hanagud, Sathya V., joint author. II. U. S. Army. Corps of Engineers. (Series: U. S. Waterways Experiment Station, Vicksburg, Miss. Technical report S-75-9, Report 1)
TA7.W34 no.S-75-9 Report 1